



Durham E-Theses

Towards a fuller understanding of selected molecular compounds

Probert, Michael R.

How to cite:

Probert, Michael R. (2005) *Towards a fuller understanding of selected molecular compounds*, Durham theses, Durham University. Available at Durham E-Theses Online: <http://etheses.dur.ac.uk/2393/>

Use policy

The full-text may be used and/or reproduced, and given to third parties in any format or medium, without prior permission or charge, for personal research or study, educational, or not-for-profit purposes provided that:

- a full bibliographic reference is made to the original source
- a [link](#) is made to the metadata record in Durham E-Theses
- the full-text is not changed in any way

The full-text must not be sold in any format or medium without the formal permission of the copyright holders.

Please consult the [full Durham E-Theses policy](#) for further details.

TOWARDS A FULLER UNDERSTANDING OF SELECTED MOLECULAR COMPOUNDS

Michael R. Probert

**A copyright of this thesis rests
with the author. No quotation
from it should be published
without his prior written consent
and information derived from it
should be acknowledged.**

Thesis submitted in part fulfilment of the requirements for the degree of

Doctor of Philosophy

at the

University of Durham

Department of Chemistry
June 2005



07 DEC 2005

TOWARDS A FULLER UNDERSTANDING OF SELECTED MOLECULAR COMPOUNDS

Thesis submitted for the degree of Doctor of Philosophy by

Michael R. Probert, University of Durham

June 2005

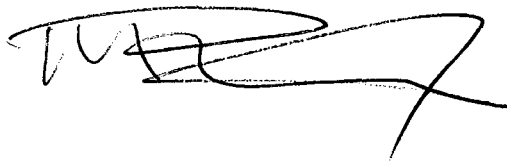
Abstract

This work is separated into two distinct sections. The first section deals with the analysis by variable temperature single crystal X-ray diffraction of crystalline molecular materials with novel physical properties. The second section details the electron density analysis of selected crystalline compounds using high resolution, low temperature single crystal X-ray diffraction.

Chapter 1 provides introduction to X-ray diffraction outlining the theory this work is based on. Chapter 2 introduces the molecular material studies based on materials containing the bis(ethylenedithio)-tetrathiafulvalene molecule. The aim of these studies was to achieve a greater understanding of the materials and the changes they undergo when exposed to variations in temperature whilst in the crystalline state. These structural changes observed are very minor but have dramatic effects on the electrical properties of the materials studied. It became apparent that the only way to form a full understanding of these materials was to be able to 'see' the electronic configuration of the materials, not just their gross structure. The field of electron density analysis by X-ray diffraction is now a well documented area. Chapter 4 provides an introduction to the field of electron density analysis. Diffraction experiments were conducted on systems of different complexity to investigate this field and these results are reported in Chapter 5. No electron density analyses have been conducted on the molecular materials studied in Chapter 3 as yet, due to the lack of crystals of suitable quality. It was also noted that to fully categorise the nature of the physical changes occurring in these structures that a diffractometer capable of analysing these samples throughout the temperature range of their physical phenomena was needed. An outline for the development of such a diffractometer is detailed in Chapter 6, 'future works'.

DECLARATION

The work described in this thesis was carried out in the Department of Chemistry at the University of Durham between October 2001 and June 2005, under the supervision of Prof. Judith A. K. Howard. All the work is my own, unless otherwise stated, and has not been submitted previously for a degree at this, or any other university.



Michael R. Probert

The copyright of this thesis rests with the author. No quotation from it should be published without his prior written consent and information derived from it should be acknowledged.

Acknowledgements

Firstly I would like to thank my supervisor Prof. Judith Howard for her invaluable help, guidance and support throughout the years. Her patience seemingly knows no bounds and is equally matched by her enthusiasm and dedication. Thanks also for the cakes, biscuits and many meals in and out of the lab, but especially for giving me the opportunity to leave England's 'green and pleasant land' and finally get to see some of the wider world.

I would also like to thank all of the members of the lab for making working life in Durham something far more interesting.

Particular thanks have to go to:

Andres and Dima – help not only with all things crystallographic and entertaining my ideas but also for the introduction to the great game.

Mike Turner aka Mike 3 – for helping to instil the perfect ways to start a conference and keeping me sane when things weren't going so well.

However I owe most of this to Alex who has been a constant support for me throughout my time in Durham. Thanks babe, love you.

Table of Contents

Title	i
Abstract	ii
Declaration	iii
Acknowledgements	iv
Table of Contents	v
List of Figures	viii
List of Tables	xiv
Abbreviations	xvii

Chapter 1	<i>Introduction to X-ray diffraction</i>	
1.1	<i>Part one basic theory</i>	1
	1.1.1 <i>Interactions of X-rays with crystals</i>	1
	1.1.2 <i>Laue diffraction</i>	2
	1.1.3 <i>Bragg diffraction</i>	2
	1.1.4 <i>Systematic corrections</i>	3
1.2	<i>Introduction to X-ray diffraction Part 2: Experiments</i>	6
	1.2.1 <i>What is required from the experiment?</i>	6
	1.2.2 <i>Which crystal?</i>	6
	1.2.3 <i>Unit cell determination</i>	6
	1.2.4 <i>Space group determination</i>	8
	1.2.5 <i>Structure solution and refinement</i>	9
	1.2.6 <i>Internal structure validation</i>	12
1.3	<i>Introduction to practical techniques</i>	13
	1.3.1 <i>Preparation of sample</i>	13
	1.3.2 <i>Crystal Mounting</i>	13
	1.3.3 <i>Temperature controllers</i>	15
	1.3.4 <i>Diffractometers</i>	16
	1.3.5 <i>Data Reduction, Solution and Refinement</i>	19
1.4	<i>References</i>	20

Chapter 2	Introduction to selected organic molecular materials	
2.1	General Introduction	22
2.2	Introduction to the compounds studied	26
2.3	References	33
Chapter 3	Selected studies of organic molecular crystals	
3.1	The study of the structure of $\beta''(ET)_4[(H_3O)Ga(C_2O_4)_3]PhNO_2$	36
3.2	The study of the structure of: $\beta''(ET)_4[(H_3O)Ga(C_2O_4)_3]C_5H_5N$	53
3.3	The study of the structure of: $\beta''(ET)_4[(NH_4)M(C_2O_4)_3]_2 \cdot 18\text{-crown-6-ether} \cdot (H_3O)_2 \cdot (H_2O)_5$; $M = Ga$ or Cr	58
3.4	The study of the structure of: $\kappa\text{-(}ET)_2Cu(SCN)_2$	64
3.5	The study of the structure of: $\alpha\beta\text{-(}ET)_4[(H_3O)Ga(C_2O_4)_3]PhN(CHO)CH_3$	69
3.6	The study of the structure: $\beta''(ET)_4[(H_3O)Ga(C_2O_4)_3]CH_2Cl_2$	77
3.7	References	80
Chapter 4	Introduction to charge density theory and experiments.	
4.1	Theoretical introduction	82
4.1.1	Shortfalls of the IAM model	83
4.1.2	The Spherical Kappa formalism	83
4.1.3	Multipole model for Aspherical atoms	84
4.2	Experimental considerations: data collection and reduction.	86
4.2.1	Is there a need for a change from the standard experimental procedure?	86
4.2.2	Use of machines – adapting the collection strategy	87
4.2.3	Redundancy and pre-calculated completeness	88
4.2.4	Duration of the diffraction experiment	89

	4.2.5	<i>Data processing</i>	89
	4.3	<i>Interpretation of results</i>	90
	4.4	<i>References</i>	95
Chapter 5		<i>Charge Density Studies:</i>	
	5.1	<i>TCNQ (7,7,8,8-tetracyano-p-quinodimethane)</i>	96
	5.2	<i>Probing the Magnetic exchange interactions in some copper complexes</i>	106
	5.2.1	<i>Bis(D,L-alaninato)copper(II) Hydrate (Cu-d-ALA-d-ALA)</i>	107
	5.3	<i>Cu – L-alanine-L-phenylalanine (Cu-L-ALA-PHE)</i>	114
	5.4	<i>Cu – L-alanine-L-tyrosine</i>	119
	5.5	<i>NNDPNA (N,N-dimethyl-para-nitro-aniline)</i>	120
	5.6	<i>References</i>	127
Chapter 6		Future research and development	
	6.1	<i>The necessity for improvement in current X-ray diffraction instrumentation</i>	129
	6.2	<i>X-ray detection</i>	130
	6.3	<i>A New diffractometer?</i>	131
Appendix A		Seminars and courses attended	134
Appendix B		Publications List	137
Appendix C		Other Structure Analyses	138
Appendix D		Research Sample Crystallographic Tables	144
Appendix E		Service Sample Crystallographic Tables	145

List of Figures

Chapter 1	Introduction to X-ray diffraction	
1.1	Diagram showing Bragg's Law for a given set of Miller planes.	3
1.2.3	Crystal axes relating to the Cartesian set.	7
1.2.4	Atomic Scattering factors	10
1.3.1	Schematic of the Helix cryo-system.	16
1.3.2	A SMART 6K diffractometer with Oxford cryostream.	17
1.3.3	The Fddd diffractometer.	18
Chapter 2	Introduction to selected organic molecular materials	
2.1.1	TTF and TCNQ molecular diagrams.	23
2.1.2	The TMTSF molecule	24
2.1.3	The BEDT-TTF molecule	25
2.1.4	The DMET, left, and MPT, right, molecules	25
2.1.5	Schematic showing the different packing motifs of $(ET)_2I_3$.	25
2.2.1	Hexagonal packing of anionic layer including a guest molecule, taken from the β'' - $(ET)_4[(H_3O)Ga(C_2O_4)_3]PhNO_2$ structure.	27
2.2.2	Graph showing the change in resistivity of β'' - $(ET)_4[(H_3O)Ga(C_2O_4)_3]PhNO_2$ with temperature.	28
2.2.3	The electrical Resistivity of β'' - $(ET)_4[(NH_4)M(C_2O_4)_3]18$ -crown-6-ether $\cdot (H_xO)_6$ $M = Cr$ or Ga , $x = 2$ or 3 .	30
2.2.4	The preliminary proton resistivity of β'' - $(ET)_4[(NH_4)M(C_2O_4)_3]18$ -crown-6-ether $\cdot (H_xO)_6$ $M = Cr$ or Ga , $x = 2$ or 3 .	30
2.2.5	ET molecule showing chemically equivalent bonds, highlighted in the same colour, used in the charge analysis of the molecule.	31

Chapter 3	<i>Selected studies of organic molecular crystals</i>	
3.1.1	<i>Asymmetric unit of β''-(ET)₄[(H₃O)Ga(C₂O₄)₃]PhNO₂</i>	36
3.1.2	<i>The packed unit cell of β''-(ET)₄[(H₃O)Ga(C₂O₄)₃]PhNO₂ viewed down the b-axis</i>	38
3.1.3	<i>The hexagonal cavity formed by the Ga-oxalate species and protonated water molecules encapsulating the nitro benzene guest molecule.</i>	39
3.1.4	<i>Graph showing the variation of occupancy factors with temperature for the disordered ethylene groups</i>	40
3.1.5	<i>F_o maps viewed through the plane of the disordered terminal ethylene group (C1,C2) of the disordered ET molecule, contours at 0.1 e/Å³, upper left 290 K, upper right 200 K, lower left 150 K and lower right 100 K.</i>	40
3.1.6	<i>Cell volume variation with temperature for β''-(ET)₄[(H₃O)Ga(C₂O₄)₃]PhNO₂</i>	43
3.1.7	<i>Graph showing the uncorrected unit cell volumes, and the disconnection at the same temperature of data collected on different SMART diffractometers</i>	44
3.1.8	<i>Orientation of the nitrobenzene to the ET molecules at 100 K.</i>	45
3.1.9	<i>Variation of torsion angle in the nitro benzene molecule, in β''-(ET)₄[(H₃O)Ga(C₂O₄)₃]PhNO₂, with temperature.</i>	46
3.1.10	<i>Graph showing the changes in the major S – S interactions in β''-(ET)₄[(H₃O)Ga(C₂O₄)₃]PhNO₂.</i>	48
3.1.11	<i>Average spherical thermal parameters at various temperatures for β''-(ET)₄[(H₃O)Ga(C₂O₄)₃]PhNO₂.</i>	51
3.2.1	<i>Pyridine is the guest molecule in β''ET₄[(H₃O)Ga(C₂O₄)₃]C₅H₅N</i>	53
3.2.2	<i>Asymmetric unit of pyridine guest complex, Ga: dark green, S-yellow, O-red, N-blue, C-grey, H-green, pyridine not labelled for clarity.</i>	53

3.3.1	<i>18-crown-6-ether, the guest molecule in $\beta''(ET)_4[(NH_4)M(C_2O_4)_3]_2$ 18-crown-6-ether $\cdot (H_3O)_2 \cdot (H_2O)_5$</i>	58
3.3.2	<i>Packing diagram showing the layering in $\beta''(ET)_4[(NH_4)Ga(C_2O_4)_3]_2$ 18-crown-6-ether $\cdot (H_3O)_2 \cdot (H_2O)_5$ at 30 K, the water molecules and hydrogen atoms have been removed for clarity, view is perpendicular to the a-c plane</i>	58
3.3.3	<i>Crown ether channels containing water molecules at 30 K</i>	60
3.3.4	<i>The crown ether cage formed from Ga-oxalate layers, above (green) and below (pink) the crown ether guest molecule</i>	61
3.3.5	<i>Short S – S contacts in $\beta''(ET)_4[(NH_4)M(C_2O_4)_3]_2$ 18-crown-6-ether $\cdot (H_3O)_2 \cdot (H_2O)_5$ at 30 K</i>	62
3.4.1	<i>Thermal ellipsoid plot at 50% probability for $\kappa-(ET)_2Cu(SCN)_2$ at 60 K, symmetry equivalent ligand present (connected though dashed bond).</i>	64
3.4.2	<i>Infinite Cu chains formed through the crystal, viewed perpendicular to the a-b plane.</i>	66
3.4.3	<i>S – S contacts for $\kappa-(ET)_2Cu(SCN)_2$ at 30 K</i>	67
3.5.1	<i>The guest molecule for $\alpha\beta-(ET)_4[(H_3O)Ga(C_2O_4)_3]PhN(CHO)CH_3$</i>	69
3.5.2	<i>Packing diagram of $\alpha\beta-(ET)_4[(H_3O)Ga(C_2O_4)_3]PhN(CHO)CH$ at 190 K, showing the alternating packing of the ET molecules.</i>	69
3.5.3	<i>The cavity in the metal oxalate layer containing the guest molecule in $\alpha\beta-(ET)_4[(H_3O)Ga(C_2O_4)_3]PhN(CHO)CH$ at 190 K</i>	70
3.5.4	<i>Diffraction pattern images at 90 K and 290 K, images created using FRM2FRM</i>	72

3.5.5	<i>Overlay of 4 independent ET molecules at 290 K, 190 K and 90 K from left to right respectively. Different molecules represented by differing bond colouring</i>	75
3.6.1	<i>Dichloromethane, the guest molecule in $\beta''(ET)_4[(H_3O)Ga(C_2O_4)_3]CH_2Cl_2$</i>	77
3.6.2	<i>Thermal ellipsoid plot of $\beta''(ET)_4[(H_3O)Ga(C_2O_4)_3]CH_2Cl_2$ at 120 K ellipsoids shown at 50% probability level</i>	77
Chapter 4	<i>Introduction to charge density theory and experiments.</i>	
4.1.2	<i>X-ray scattering factor schematic, for non hydrogen atoms, taken from presentation by Piero Macchi European Charge Density Meeting 2003.</i>	84
4.3.1	<i>Plots of the charge density (ρ) showing C-C and C=C of TCNQ molecule showing a bcp at the intersection of the arrows, generated using Mapview</i>	91
4.3.2	<i>Deformation density plot through the mean plane of the cyano-groups of a TCNQ molecule.</i>	92
4.3.3	<i>Negative Laplacian showing O electron lone pairs in the nitro group of NN-dimethyl-paranitro-aniline (NNDPNA, see section 5.5).</i>	93
Chapter 5	<i>Charge Density Studies</i>	
5.1.1	<i>The recorded crystal faces and their dimensions</i>	97
5.1.2	<i>Data collection strategy</i>	98
5.1.3	<i>Thermal ellipsoid plot of TCNQ shown at 50% probability</i>	99
5.1.4	<i>Flow chart from .raw files to .hkl file for refinement</i>	100
5.1.5	<i>Residual electron density after multipole refinement</i>	102
5.1.6	<i>Static deformation density map for TCNQ</i>	103
5.1.7	<i>Bond path diagram for TCNQ</i>	104
5.2.1	<i>The crystal faces measured</i>	107

5.2.2	<i>Thermal ellipsoid plot of Bis(D,L-alaninato)copper(II) Hydrate shown at 50% probability, showing possible coordination with water, disorder removed for clarity</i>	108
5.2.3	<i>Copper and oxygen atoms forming chains through the structure</i>	108
5.2.4	<i>Residual electron density in the copper – ligand plane after multipole refinement</i>	110
5.2.5	<i>Static deformation density map through the carboxylate group</i>	111
5.2.6	<i>Bond path from O (water) to copper centre and static deformation density map through the plane of the water molecule</i>	112
5.3.1	<i>Images above (left) and below (right) the phase transition, images generated using FRM2FRM¹⁸</i>	116
5.3.2	<i>Thermal ellipsoid plot, shown at 50%, of room temperature structure</i>	116
5.3.3	<i>Thermal ellipsoid plot, shown at 50 %, of the 250K structure</i>	117
5.3.4	<i>Trace of overlay of the three independent centres at 250 K (pink) and the room temperature framework (dashed green)</i>	118
5.5.1	<i>Thermal ellipsoid plot of NNDPNA at 120 K with atomic labelling</i>	121
5.5.2	<i>Residual electron density for NNDPNA, contours at 0.05 eA³ positive contours are red, negative blue and black dotted zero</i>	123
5.5.3	<i>Deformation density for NNDPNA, contours at 0.1 eA³ (red positive, blue negative and dotted zero)</i>	124
5.5.4	<i>Negative Laplacian of nitro group, for NNDPNA, showing lone pairs on O atoms</i>	124
5.5.5	<i>Bond path diagram for NNDPNA</i>	125

Chapter 6	Future research and development	
6.1	<i>Schematic of beamstop placed inside the sample environment</i>	130
6.2	<i>Test case of traditional beamstop (left) and beamstop inside Be can (right) collected on a SMART 1K diffractometer</i>	131
6.3	<i>The concept of 'Magic Distances'</i>	133

List of Tables

Chapter 1	Introduction to X-ray diffraction	
1.2.3	<i>The Bravais lattices, the unit cell requirements and the centering types</i>	7
Chapter 2	Introduction to selected organic molecular materials	
2.1.1	<i>Early chronology of synthetic organic conductors and superconductors</i>	23
2.2.1	<i>Averaged, chemically equivalent, bond lengths determined experimentally in neutral ET molecules</i>	32
Chapter 3	Selected studies of organic molecular crystals	
3.1.1	<i>Room Temperature unit cell dimensions for: β''- $(ET)_4[(H_3O)Ga(C_2O_4)_3]PhNO_2$</i>	37
3.1.2	<i>Crystallographic data for β''- $(ET)_4[(H_3O)Ga(C_2O_4)_3]PhNO_2$ at 290 K</i>	42
3.1.3	<i>S – S interaction lengths calculated at the temperatures for which full structure solutions were available, errors in the order of $\pm 0.002 \text{ \AA}$</i>	47
3.1.4	<i>C = C double bond lengths in the independent ET molecules</i>	48
3.1.5	<i>Calculated charges (Q) supported by ET molecules calculated using Equation 2.1</i>	49
3.1.6	<i>Selected crystallographic data over the range of temperatures studied</i>	52
3.2.1	<i>Crystallographic data for $\beta''ET_4[(H_3O)Ga(C_2O_4)_3]C_5H_5N$ at 290 K</i>	54
3.2.2	<i>Crystallographic data for $\beta''ET_4[(H_3O)Ga(C_2O_4)_3]C_5H_5N$ at 30 K</i>	57
3.3.2	<i>Short S – S contacts in $\beta''(ET)_4[(NH_4)Ga(C_2O_4)_3]18$- crown-6-ether $\cdot (H_2O)_7$ at 30 K.</i>	62

3.3.3	<i>Calculated charges carried by the ET molecules in $\beta''(ET)_4[(NH_4)M(C_2O_4)_3]_2$ 18-crown-6-ether $\cdot(H_3O)_2(H_2O)_5$</i>	63
3.4.1	<i>Crystallographic data for $\kappa-(ET)_2Cu(SCN)_2$</i>	65
3.4.2	<i>Ligand bond lengths in $\kappa-(ET)_2Cu(SCN)_2$</i>	67
3.4.3	<i>Crystallographically independent ET molecule C=C double bond lengths present in $\kappa-(ET)_2Cu(SCN)_2$</i>	67
3.4.4	<i>Short S – S contacts for $\kappa-(ET)_2Cu(SCN)_2$ at 30 K</i>	68
3.4.5	<i>Calculated charges (Q) carried by the ET molecules in $\kappa-(ET)_2Cu(SCN)_2$, see Equation 2.1</i>	68
3.5.1	<i>Crystallographic data for: $\alpha\beta-(ET)_4[(H_3O)Ga(C_2O_4)_3]PhN(CHO)CH_3$ at temperatures shown</i>	71
3.5.2	<i>Crystallographic data for: $\alpha\beta-(ET)_4[(H_3O)Ga(C_2O_4)_3]PhN(CHO)CH_3$ at 90 and 190 K</i>	74
3.5.3	<i>ET molecules' central C = C bond lengths</i>	75
3.5.4	<i>Calculated charges supported by the independent ET molecules in $\beta''(ET)_4[(H_3O)Ga(C_2O_4)_3]PhN(CHO)CH_3$</i>	76
3.6.1	<i>Selected crystallographic details for $\beta''(ET)_4[(H_3O)Ga(C_2O_4)_3]CH_2Cl_2$ at 120 K</i>	78
Chapter 4	<i>Introduction to charge density theory and experiments.</i>	
4.3.1	<i>Types of stable critical point and their chemical meaning.</i>	91
Chapter 5	<i>Charge Density Studies</i>	
5.1.1	<i>TCNQ crystallographic data at 120 K * non hydrogen atoms</i>	96
5.1.2	<i>The recorded crystal faces and their dimensions</i>	97
5.1.3	<i>Spherical atom refinement data at 120 K</i>	99

5.1.4	<i>Bond lengths and values of the electron density (ρ), the Laplacian ($\nabla^2\rho$) and the ellipticity of the bond at the bond critical points</i>	103
5.1.5	<i>Final agreement factors for multipole refined TCNQ structure at 120 K</i>	105
5.2.1	<i>The crystal faces measured</i>	107
5.2.2	<i>Final crystal data for Bis(D,L-alaninato)copper(II) Hydrate at 120 K</i>	113
5.2.3	<i>Values at the bond critical points for the ordered section of the structure</i>	113
5.3.1	<i>Crystal data for Cu-ALA-PHE above and below phase transition</i>	115
5.5.1	<i>Crystallographic data for NNDPNA at 120 K</i>	121
5.5.2	<i>Critical values at molecular bond critical points for NNDPNA.</i>	126

Abbreviations

<i>ET</i>	<i>BEDT-TTF - bis(ethylenedithio)-tetrathiafulvalene</i>
<i>TTF</i>	<i>tetrathiafulvalene</i>
<i>TMTSF</i>	<i>tetramethyl tetraselenafulvalene</i>
<i>DMET</i>	<i>dimethyl(ethylenedithio)diselenadithiafulvalene</i>
<i>MPT</i>	<i>methylene dithiopropylenedithiotetrathiafulvalene</i>
<i>BEDO-TTF</i>	<i>bis(ethylenedioxo)-tetrathiafulvalene</i>
<i>DIMET</i>	<i>3,4-dimethyl-3',4'-ethylenedithio-tetrathiafulvalene</i>
<i>MDT</i>	<i>methylenedithiotetrathiafulvalene</i>
<i>TCNQ</i>	<i>7,7,8,8-tetracyano-p-quinodimethane</i>
<i>DMTCNQ</i>	<i>2,4-dimethyl-TCNQ</i>
<i>ALA</i>	<i>alanine</i>
<i>PHE</i>	<i>phenylalanine</i>
<i>TYR</i>	<i>tyrosine</i>
<i>MST</i>	<i>metal-semiconductor transition</i>
<i>SST</i>	<i>Semiconductor-superconductor transition</i>
<i>NNDPNA</i>	<i>N,N-dimethyl-para-nitro-aniline</i>

Definitions of symbols found in equations

F_o	<i>Observed structure factor</i>
F_c	<i>Calculated structure factor</i>
ρ_{xyz}	<i>electron density</i>
ρ_{IAM}	<i>electron density for independent atom model</i>
ρ_{atom}	<i>electron density associated with an atom</i>
ρ_{core}	<i>electron density associated with an atom's core electrons</i>
$\rho_{valence}$	<i>electron density associated with an atom's valence electrons</i>
ρ_{pro}	<i>electron density derived from the pro-molecule</i>
κ	<i>expansion coefficient</i>
$-\nabla^2\rho(r)$	<i>negative Laplacian of electron density</i>

Chapter 1

Introduction to X-ray diffraction

1.1 Part one basic theory

1.1.1 Interactions of X-rays with crystals

The interaction of X-rays with crystalline material is a phenomenon that is well known, the analysis of the interaction has become an important analytical tool since the first publications of structures deduced from said interaction in 1913¹. The important properties of X-rays had been described earlier in 1896, by Röntgen. The field of X-ray crystallography has since then grown into a large division of physical science, proving invaluable to many diverse areas in modern chemistry. This thesis does not intend to be a treatise on the theory of diffraction, as such an attempt would be foolish and redundant given the wide range of texts on the subject²⁻⁵ however a short summary of the field and some of its history is included as a background to the theory used throughout. For the purposes of this work a 'crystal' is defined as being a continuous, 3 dimensional, periodic array of repeated units. The periodic array is known as the crystal lattice and can take one of only 14 forms, known as the Bravais lattices. The 'repeated units' are the unit cell; the building block of the crystal that, using only translational motion, can fill all space by placing a unit cell on each lattice point. The unit cell itself can often be generated from a much smaller fragment, the asymmetric unit. These smaller units depend on the presence of symmetry elements inside the unit cell, which upon operation generate the unit cell from the asymmetric unit. The combination of these symmetry elements form the definition of the system's space group⁶, a symbol characterizing the system and showing the symmetry elements present. There are 230 possible space groups.



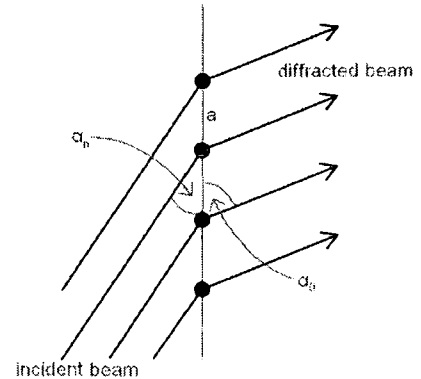
1.1.2 Laue diffraction

Max von Laue interpreted the diffraction of X-radiation from crystalline samples analogously to patterns from diffraction gratings, though expanded for use with a 3 dimensional lattice, giving rise to 3 independent conditions which must be met simultaneously for diffraction to occur.

$$a(\cos\alpha_n - \cos\alpha_0) = h\lambda$$

$$b(\cos\beta_n - \cos\beta_0) = k\lambda$$

$$c(\cos\gamma_n - \cos\gamma_0) = l\lambda$$



Equation 1.1.2: The three Laue conditions, shown diagrammatically for the a direction

In the Laue equations a , b and c are the distances between rows of atoms and the angles $\alpha_n, \beta_n, \gamma_n$ and $\alpha_0, \beta_0, \gamma_0$ are those shown in equivalent to the ones shown in the diagram above. Laue diffraction is still used to interpret multiple wavelength (white radiation) diffraction experiments such as those commonly carried out at (a large scale) central facility, on instruments such as VIVALDI.

1.1.3 Bragg diffraction

Although diffraction was understood to occur from a regular crystal lattice, it was not until 1912 when W. L. Bragg represented the same phenomenon using a simple geometric approach to determine when constructive interference would occur in the system and where reflections could be detected. Instead, like Laue, of treating the crystal as a 3D entity, Bragg proposed a law which depended purely on lattice planes, likening a crystal to a diffraction grating such as the one used by Thomas Young in the diffraction of light experiments. This treatment yielded Bragg's Law, see Figure 1.1, where the path length difference between the beam diffracted from one layer and another is: $ab + bc$, a distance which simple trigonometry yields to be equal to $2d\sin\theta$. For the interference between the two diffracted beams to be constructive, i.e. observed as a 'reflection', this distance must be equal to a whole number of wavelengths of the primary beam, $n\lambda$. Bragg then developed his well known law, its usual expression being:

$$n\lambda = 2d\sin\theta$$

Equation 1.1.3: The Bragg equation

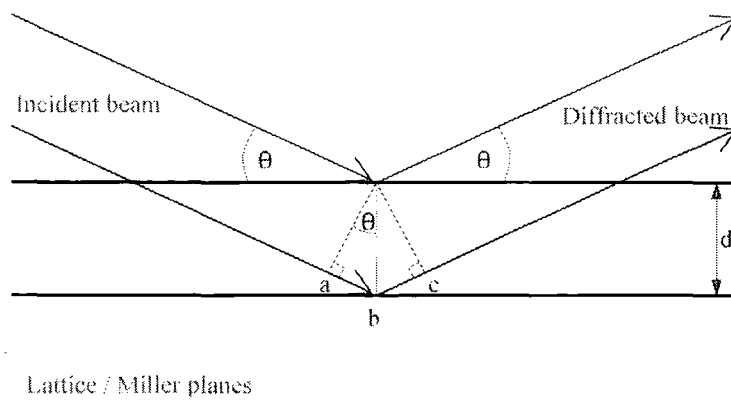


Figure 1.1: Diagram showing Bragg's Law for a given set of Miller planes.

Bragg's law is a simplification of the complex interactions found in a diffraction experiment and is not a true physical representation of the interactions, as there are no physical planes reflecting X-rays inside the crystal. This, however, does not detract from its usefulness and it has for many years been the most commonly used first step in the interpretation of experimental diffraction patterns. As detection methods have evolved especially the advent of area detectors, significant diffraction, although diffuse, can be observed away from the Bragg reflection condition. This diffuse scatter is now beginning to be interpreted⁷ for the determination of other crystal characteristics that are outside the scope of this work, though this may spell the 'beginning of the end' for the Bragg equation in its raw form.

1.1.4 Systematic corrections

These are corrections that are required due to influences in the diffracted intensity from the method of collection which occur in a systematic way. Some of the more common systematic corrections applied to diffraction data are listed below along with how they affect the data collected and some of the procedures used to correct for them.

Lorentz

A particular reciprocal lattice point (r.l.p) may remain in the diffraction geometry for longer than other r.l.p's causing an artificial increase in the value of the intensity for that

reflection. This is purely a result of relative speeds that r.l.p's travel through the diffraction geometry and as such the correction is applied automatically. It is commonly grouped together with polarisation and reported as the Lp correction in the output files of the integration routines.

*Polarisation*⁸

As a crystal monochromated X-ray beam is inherently partially polarised, a polarisation correction needs to be applied, this correction factor is based on the angle of diffraction from the monochromator and the value of 2θ where the reflection occurs. It is a machine dependent correction that can cause a bias in the data, especially at higher 2θ values and as with the Lorentz correction is applied automatically to the data.

Absorption

This is a correction applied for loss of intensity due to absorption of X-rays in the crystal, resulting in reduced intensity measurements. For small organic structures it is often such a small effect that can be practically ignored; for structures containing heavier elements it can become very important, requiring accurate correction. There are two common ways of correcting for absorption, an empirical approach and a statistical one. The first, implemented in XPREP⁹, requires knowledge of the crystal shape, including size and apparent crystal faces (Miller indices relating to the face) and is calculated from the path length of the diffracted beam through the crystal. The second relies on the symmetry of the point group of the crystal system to analyse and correct equivalent intensities, this is the method implemented in SADABS¹⁰ which also performs other corrections and normalises the σ -values.

*Thermal Diffuse Scattering*¹¹

Thermal diffuse scattering (TDS) is a product of cooperative lattice vibrations, causing an increase in the background intensity that is not uniform across the diffraction pattern, instead is centred on the Bragg position. The TDS effect increases with diffraction angle, and if present to a large extent causes the systematic reduction of the anisotropic thermal parameters from their true values. TDS effects are generally small and receive little attention. The effect is reduced by lowering the temperature of data collections.

Extinction¹² – Primary and Secondary

This is a process that causes the systematic reduction in the observed intensity of strong reflections compared to the calculated intensity derived from the model. Extinction occurs in two forms primary and secondary. The first of these is due to a double reflection of the beam occurring and thereby lowering the observed intensity. Primary extinction is commonly associated with near perfect crystals. Secondary extinction is caused by the mosaicity of a crystal, when diffraction occurs from one mosaic block that part of the primary beam is no longer available to diffract from another perfectly aligned mosaic block. Secondary extinction is less damaging to data quality as the proportion of the primary beam lost through diffraction is so small.

Detector face plate correction (fiducial)

The detector face plate is slightly absorbing to X-rays. The angle of incidence of a reflection to the plate determines the path length through it and thus determines the amount of absorption occurring at this point before the diffracted beam's intensity is measured.

$\lambda/2$ contamination

Contamination of the diffraction pattern by $\lambda/2$ radiation can be seen by the presence of weak reflections in the diffraction pattern, which have Miller indices corresponding to half those of some of the strong reflections. These weak reflections can break the assumed symmetry rules of a system and it appears as if there are non integer reflections present in the pattern. $\lambda/2$ contamination can also result in some low angle reflections appearing much stronger than predicted as they can have additional intensity by the method described above.

Crystal Decay

X-rays are quite hard and they can cause damage to the crystal being studied, this radiation damage cannot be avoided. The propagation of the radiation damage through the crystal and hence how much it affects the diffraction is dependant on the motion of atoms in the structure, therefore cooling the crystal can reduce significantly the effects of radiation damage.

It is impossible to correct for any random errors that occur, though it is hoped that collecting high redundancies of data reduces the effect of these errors to a minimum.

1.2 Introduction to X-ray diffraction Part 2: Experiments

1.2.1 What is required from the experiment ?

Before starting any experiment, it is wise to envisage what is required and or desired from the results of the work. In many cases for diffraction experiments this is an easy question to answer: the relative connectivity of the atoms in the structure and any electronic interactions therein, fortunately these are the results gained from any successful refinement of single crystal diffraction data. Crystallography has thus become the characterisation method of choice for many chemists, and is a powerful tool for the physical scientist. It aids understanding of the properties of crystalline materials, showing atomic and molecular interactions present in the crystalline state. More advanced experiments requiring highly accurate data or novel crystal environments, require more careful planning – these will be discussed in a later part of this thesis.

1.2.2 Which crystal ?

This seemingly trivial part of any single crystal experiment is a step of vital importance. It is far more time efficient and productive to spend a little longer selecting the best possible sample, than to collect data from a lower quality crystal and then have to apply many corrections and/or constraints when modelling the final data. This does present an inherent problem, which requires consideration when interpreting single crystal diffraction data: only a fraction of the sample is analysed and as such may not be representative of the bulk material. The solution is relatively simple requiring the experimentalist to check and make sure that the sample is representative by testing more than one crystal, even if the quality of the rest of the sample is lower due to any of the many factors that affect crystallisation process.

1.2.3 Unit cell determination

Once a suitable crystal has been selected and mounted on the diffractometer, a very short data collection is completed. From the diffraction data collected, vectors are calculated between reflections and an indexing routine calculates the orientation matrix from these vectors. The indexing routine essentially calculates the three shortest non co-planar vectors between reflections and arbitrarily assigns the reflections to have the *100*, *001* and *010* Miller indices (*hkl*). Then other reflections are assigned *hkl* values

from the derived unit cell, which is necessarily at least a sub-cell of the correct unit cell. If other reflections that were collected return indices of rational fractions then the derived cell is increased in size to compensate for this.

The unit cell, if it is primitive, is the smallest parallelepiped constructed so that the three dimensional crystal structure may be recreated through translational symmetry only. The unit cell is always defined in terms of the three sides **a**, **b**, **c** and their internal angles α , β , γ .

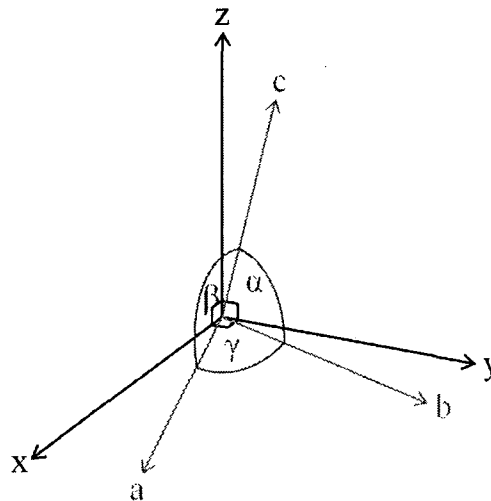


Figure 1.2.3: Crystal axes relating to the Cartesian set.

This gives rise to a crystallographic coordinate system. A unit cell can be categorised into one of seven crystal systems, which combined with the four lattice types of centering P, C, I, F give rise to 14 possible Bravais lattices shown in Table 1.2.3.

Crystal system	Restrictions on Unit Cell	Centering allowed
Triclinic	None	P
Monoclinic	$\alpha = \gamma = 90^\circ$	P, C
Orthorhombic	$\alpha = \beta = \gamma = 90^\circ$	P, C, F, I
Tetragonal	$a = b, \alpha = \beta = \gamma = 90^\circ$	P, I
Cubic	$a = b = c, \alpha = \beta = \gamma = 90^\circ$	P, F, I
Trigonal	$a = b, \alpha = \beta = 90^\circ, \gamma = 120^\circ$	P
Hexagonal	$a = b, \alpha = \beta = 90^\circ, \gamma = 120^\circ$	P

Table 1.2.3: The Bravais lattices, the unit cell requirements and the centering types.

These 14 Bravais lattices can then be combined with the crystallographic symmetry elements to generate the 230 possible space groups. Each crystal structure determined belongs to one of these 230 space groups, which allow a simplification of the structural model to the asymmetric unit. This is the simplest description (in terms of parameters) of the crystal structure that can be used to construct the unit cell given the use of the symmetry operations related to that space group and the translational symmetry of the unit cell.

1.2.4 Space group determination

Space group determination is made possible by the analysis of systematically absent reflections in the diffraction data and the equivalence of the reflection intensities. The symmetry of a given system may be such that systematic reflections are forbidden due to the wave nature of X-rays and only destructive interference that would occur at that reflections position. For example, if a 2_1 screw axis is present in the c direction, there are two equivalent positions of (x, y, z) and $(-x, -y, -z+1/2)$ leading to the reflections where the l index is odd for the $00l$ reflections, being absent from the diffraction pattern. These specific types of zero intensity reflections are known as systematic absences.

Incorrect determination of the space group makes the structure solution more difficult and often impossible. If there is doubt over the true space group of a system, as can often happen if the crystal were imperfect or there were disorder in the structure, then the lower symmetry space group should be chosen for initial analysis, as it can be used to trace the true space group after refinement. The structure (given enough data) will always solve in a lower symmetry space group but the refinement is more difficult and less stable, due to the increased number of parameters and correlations between parameters. There is an ongoing argument between crystallographers about the treatment of disordered structures where the disorder breaks the symmetry of the parent space group, whether to refine the structure in the higher symmetry SG, or to reduce the symmetry and struggle with highly correlated parameters which can destabilise the least squares refinement.

1.2.5 Structure solution and refinement⁴

The diffracted X-ray beam, scattered by a crystal, has an associated intensity and phase. The intensity of the scattered beam, for a given reflection, is proportional to the amplitude its structure factor ($|F_{hkl}|_o$) – however it is fundamentally very difficult to measure the phase of a diffracted beam directly. This leads to the greatest problem with crystallography known as the ‘the phase problem’. Although phases are experimentally difficult to measure, they can be calculated from the structure once it is known and the intensities have been measured.

$$|F_{hkl}|_o = \sum_j f_j \exp 2\pi i(hx_j + ky_j + lz_j)$$

Equation 1.2.5a: Structure factor equation, where f_j is the form factor of the j^{th} atom at coordinates x,y,z .

The electron density in the structure may be calculated from the structure factors using a Fourier transform of the diffraction pattern. An important point to note here is that the electron density at any point in the unit cell is affected by *all* reflections measured.

$$\rho_{xyz} = \frac{1}{V} \sum_h \sum_k \sum_l |F_{hkl}|_o e^{-2\pi i(hx + ky + lz)}$$

Equation 1.2.5b: Electron density from structure factors.

These relationships form the basis of structure refinement. Iterative improvements in a trial structure from least squares refinement of the fit of the measured intensities to those calculated from each trial structure, eventually yield the correct final structure. Structure solution is a very different problem, which is usually achieved by one of two methods – Patterson maps or direct methods. The Patterson¹³ function requires only the experimentally measurable intensity and the Miller indices of the reflections:

$$P_{(xyz)} = \frac{1}{V} \sum_{hkl} |F_{hkl}|^2 \cos[2\pi(hu + kv + lw)]$$

Equation 1.2.5c: The Patterson function.

The result of the Patterson calculation is a map in which there are peaks at positions u,v,w where $(\underline{u}, \underline{v}, \underline{w})$ describes an interatomic vector in the structure with its amplitude relative to the product of the atomic masses at the ends of the vector. For this reason Patterson methods are usually employed when a heavy atom is present (typically heavier than Br) or when direct methods fail.

Atomic scattering (form) factors⁴:

The probability of finding an electron associated with an atom in a given region of space is a function that can be well defined using quantum mechanics. The Fourier transform of this function is the atomic scattering factor (f_j). The general form of the scattering factor is shown in Figure 1.2.4, each atomic scattering factor has a maximum equal to its atomic number at $\sin\theta/\lambda = 0$ and decreases with increasing $\sin\theta/\lambda$. The rate of decay of the scattering factor with $\sin\theta/\lambda$ is dependent atomic number of the element, as shown in Figure 1.2.4.

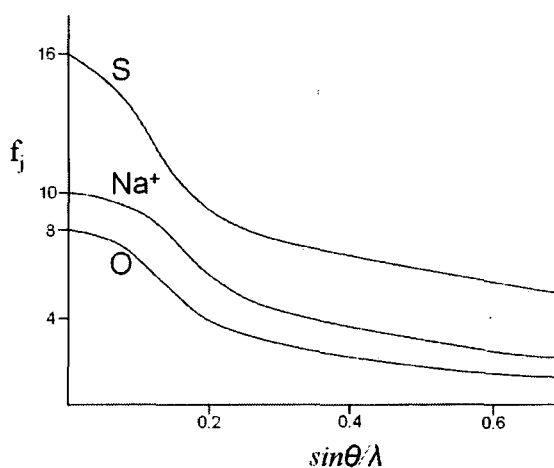


Figure 1.2.4: Atomic scattering factors

Anisotropic displacement parameters⁴:

In a perfect crystal atoms would occupy exactly the same position in each unit cell repeat, with each repeat being perfectly aligned with the previous one. This perfect crystal *never* occurs: blocks of unit cells are misaligned, to a greater or lesser extent, known as the crystal's *mosaicity*; additionally the atoms are not stationary objects, they possess thermal energy manifested in small vibrations, about their mean positions. These effects are not wholly separable by the interpretation of single crystal X-ray diffraction data. Therefore to account for the inconsistency in atomic positions in different unit cells, atoms are modelled to be within a certain volume, not simply at a point i.e. a 3D probability distribution function (p.d.f.). Initially an isotropic model is used where the atomic density is modelled to be contained within a sphere; the larger the sphere, the less well resolved the position of the atom. This model can be vastly improved by introducing anisotropy into the shape of the p.d.f; with the volume over which the atomic density is distributed being defined by an ellipsoid. An ellipsoid can be described mathematically by a 3 x 3 real symmetric matrix known in this case as the

U_{ij} matrix. The anisotropy in the positions of the atoms is a feature of the relative strengths of the modes of vibration of the atom i.e. bond libration is a lower energy mode than bond stretching.

Direct methods¹⁴:

This is the most common technique used in modern crystal structure determination. It is purely a mathematical approach to the problem whereby only well conditioned reflections are used for which a random set of phases is chosen and the structure attempted then the phases changed and the process repeated. The result is the structure solution whose phases gave the most statistically sound figures of merit. Only using these 'good' reflections the structure solution by direct methods can cause problems upon structure refinement. Some structures which solve easily have unstable refinements, this can be due to the inclusion on refinement of some reflections that are poorly correlated to the structure solution.

Phase calculation is a far greater challenge for non centric structures as in centred structures the phases can take only values of 0 or 180 degrees, due to the inversion symmetry present.

Refinement:

After an initial or 'trial' model has been found via one of the above methods, it is the experimentalist's challenge to increase the accuracy of this model to best represent the diffraction data collected. This is achieved through an iterative process using least squares matrix refinement. The least squares refinement of a given function, in this case the difference between the calculated structure factors F_c and those observed during the experiment F_o . The routine minimises the difference squared of the two values i.e.

$$L = \sum w(F_o^2 - F_c^2)^2$$

Equation 1.2.5d: Function minimised by Least squares refinement in SHELXTL.

where w expresses a weighting scheme which accounts for random errors and compensates for the differences in accuracies in the measured intensities for different reflections. The length of time for refinement varies widely, depending on the accuracy of the trial structure from solution, the quality of the data and the skill of the crystallographer.

1.2.6 Internal structure validation

The ‘ideal’ model for any dataset can never be achieved as there are many sources of random errors in the collected data, though these are minimised they can never be fully removed. This then requires a method of checking the quality of the final solution achieved. From the experimental point of view the best refinement is the one which results in the lowest values of minimum and maximum residual electron density unaccounted for in the chemically sensible structural model. There are a few mathematical analysis functions that are widely used to describe the quality of the refinement, and its basic data.

The most common of these are:

$$R_1 = \frac{\sum_i |\Delta_i|}{\sum_i |F_{o,i}|} \quad wR = \left(\frac{\sum_i w_i \Delta_i^2}{\sum_i w_i F_{o,i}^2} \right) \quad S = \sqrt{\frac{\sum (w \cdot \Delta_i^2)}{(n - m)}}$$

Equation 1.2.6: Typical structure validation parameters.

In these equations, R_1 is the residual ‘R’-factor, wR is the weighted ‘R’-factor, S is the goodness of fit (GoF), Δ_i is typically $|F_o| - |F_c|$ or $F_o^2 - F_c^2$, w is a weighting scheme, n is the number of reflections and m is the number of parameters used in the refinement. These parameters are merely indications of the state of a refinement as they do not take into account the physical discrepancies of the model. For example the R values alone do not inform about abnormal a.d.p.’s for a given atom or group of atoms. These are identified by careful inspection of the full output.

1.3 Introduction to practical techniques

1.3.1 Preparation of sample

A suitable crystal must be mounted onto a goniometer head for the single crystal X-ray diffraction experiment. Suitable crystals are of size $0.3 \times 0.3 \times 0.3 \text{ mm}^3$ or smaller. It is important not to exceed these crystal dimensions if the experiment is to be carried out on any standard laboratory diffractometer, as the crystal needs to be fully immersed in the X-ray beam. If a crystal of this size is not evident in the sample then a larger crystal may be cut using a scalpel or a razor blade. This is avoided if possible as the action of cutting a crystal can damage it and therefore reduce the quality of the data that can be collected.

1.3.2 Crystal Mounting

Three main mounting types are used for the diffractometers in the laboratory.

- 1) Hair mounted crystals – these are crystals that are mounted on the end of a single strand of hair supported in a thin metal tube, which is in turn supported by a brass pip that is inserted into the goniometer head. The crystal can be mounted on the strand of hair in a variety of ways depending on the nature of the experiment to be carried out.
 - i) If the data collection is to be started and maintained at any temperature below 200 K and if the crystal is stable in it, the crystal is mounted in a perfluoropolyether oil. This substance is an oil at room temperature and below 200 K it freezes to become a glass, providing no coherent diffraction and hence no increase in the background of the collected data. This method is a non permanent mounting of the crystal and is the quickest and simplest way of mounting the sample. If the crystal is air sensitive, this method is still suitable as the crystal can be coated in the oil preventing any contact with the air. For extremely air sensitive materials the oil must first be degassed to prevent any reaction of the crystal with trapped air in the oil.
 - ii) If the data collection is to be below 310 K then a variant on the above technique can be used. The single strand of hair can be tied into a loop, so that the crystal

sits in a small amount of oil inside the loop of hair. The surface tension of the oil holding the crystal in position. This should be used for room temperature collections of materials that are air sensitive, or require room verification of crystal quality at room temperature before permanent mounting. This method is again a non permanent process and the crystal can be removed easily from the hair for a different experiment.

- iii) If a crystal is to be used for a series of data collections at various temperatures, then the mounting needs to be more permanent than the two methods described above. In this case the crystal is attached to the same mount but is attached with an epoxy resin; a very small amount is used to produce the smallest increase in background scattering. This technique relies on two things, firstly that the sample is stable enough to survive the drying process of the resin and secondly the resin used has a small thermal expansion coefficient. The expansion/contraction of the resin used is another reason to use the smallest amount possible and have as little surface contact with the crystal as can be managed to reduce the strains on the crystal by differing expansion coefficients of the resin and the crystal.

2) Glass fibre mounted crystals: this is a variant on the above process where the fibre to which the crystal is attached is not hair, but a thin glass fibre. This has some advantages over the hair strand – generally the glass fibre is more rigid and a longer fibre can be used, placing the heavily diffracting metal that the fibre is mounted in further away from the incident beam. However the glass is not a good enough conductor to be used for very low temperature experiments, as it does not conduct enough heat from outside the cold zone of the cryo-system in use, to stop heavy icing on the crystal mount.

3) The two methods outlined above are both for use on Bruker SMART or other three circle diffractometers and their cryogenic devices. The dispex on the Fddd diffractometer uses a different cooling method and requires the crystal to be attached using a conducting material. Cooling is achieved through adiabatic expansion of a closed system of helium gas this cools a copper block in the dispex head, which then cools the crystal though conduction. The conducting material chosen is commercially available 0.3 mm pencil lead. The main component of this is graphite, which has good conductivity properties. The graphite rod is sharpened to a fine point and the crystal is then attached to it using special epoxy resin¹⁵ which has a very small thermal expansion

over the temperature range 4 to 300 K. The graphite rod is attached using an adapted head. This is a permanent mounting process that is required because the cooling of the system is not as rapid as in the gas flow coolers and therefore mounting in oil risks the crystal falling off the inverted ϕ mount before the oil has become a glass.

1.3.3 Temperature controllers

All of the low temperature devices below are connected to similar types of electronic controller, which allow a temperature to be selected and maintained within the limits of the equipment. The controllers also provide a function to allow a variety of cooling strategies to be followed, on cooling some crystals can crack, or twin and the rate of cooling has been shown to affect the degree to which this occurs.

Oxford CryoSystems Cryo-stream¹⁷

This is an open flow nitrogen cryo-cooler. It is designed to cool to 90K routinely in its standard mode and by altering the flow conditions 80K can be achieved, although with slightly lower stability. The cryostream can also heat to 350K. The cryo-stream works by surrounding the crystal in an atmosphere of dry N₂ gas at the desired temperature and thus has the advantage of surrounding the sample in an inert atmosphere. Temperatures can be logged if desired and errors recorded. The cryo-stream should be stable to within ± 0.2 K of the desired temperature.

Oxford CryoSystems Helix¹⁸

This is an open flow helium gas cryo-system with a cooling range from 300K to 25K. Bottled helium gas is cooled through heat exchangers, mounted on a two stage closed cycle cooler. The cooled helium gas is then delivered to the sample with a stability of ± 0.3 K. Figure 1.3.1 shows a schematic of the system for details.

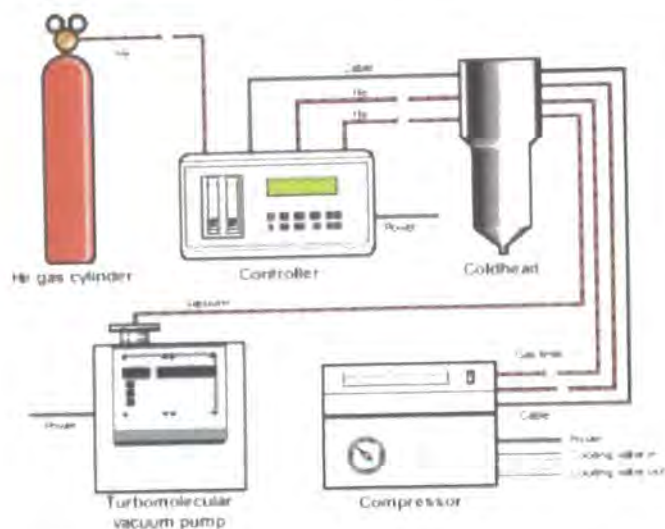


Figure 1.3.1: Schematic of the Helix cryo-system.

APD 202 Displex¹⁶

This is a closed cycle cryo-refrigerator, it has an increased cooling capacity compared to open flow devices and should offer greater stability in temperature. A 202 Displex can cool samples to 10K. Increased maintenance is required along with careful monitoring, as only a small leak in the system can cause loss of vacuum in the sample environment, or He(g) from the compressor as is the case for the Helix system. Cooling in this head relies on conduction through the 'goniometer' head and crystal mount. The crystal is maintained in a vacuum chamber, the outer walls of which are constructed of Be, which is highly transparent to X-rays.

1.3.4 Diffractometers

BRUKER SMART 1K:

This is a three circle diffractometer with a sealed tube molybdenum X-ray source with graphite monochromator $K\alpha = 0.71073 \text{ \AA}$, coupled with a Bruker charge coupled device (CCD) small area detector. The area detector has a variable distance to the sample to allow a balance between air scattering and spatial resolution. When measuring a crystal which has a large unit cell, the sample to detector distance must be increased as the reflections from a larger unit cell are closer together in reciprocal space. The SMART 1K has an Oxford Cryostream and Helix device fitted.

BRUKER SMART 6K:

This is another three circle diffractometer with the same source as the SMART 1K, it also has a CCD detector however this is much larger than the one on the SMART 1K. This allows a larger area of reciprocal space to be measured in one frame and hence allows reduction in the data collection times. The larger amount of data that is collected can often be redundant and therefore run optimisation is of greater importance. The SMART 6K has an Oxford Cryostream mounted, this is shown in Figure 1.3.2.

BRUKER APEX – with BEDE MICROSOURCE:

The third of diffractometers in the laboratory has both an Oxford Cryostream and Helix mounted. The CCD is slightly different in that it has an active area similar to the 1K CCD, but has no fibre optic taper, resulting in fewer corrections applied to the data. This diffractometer also has a novel X-ray source, a Bede Mo Microsource.

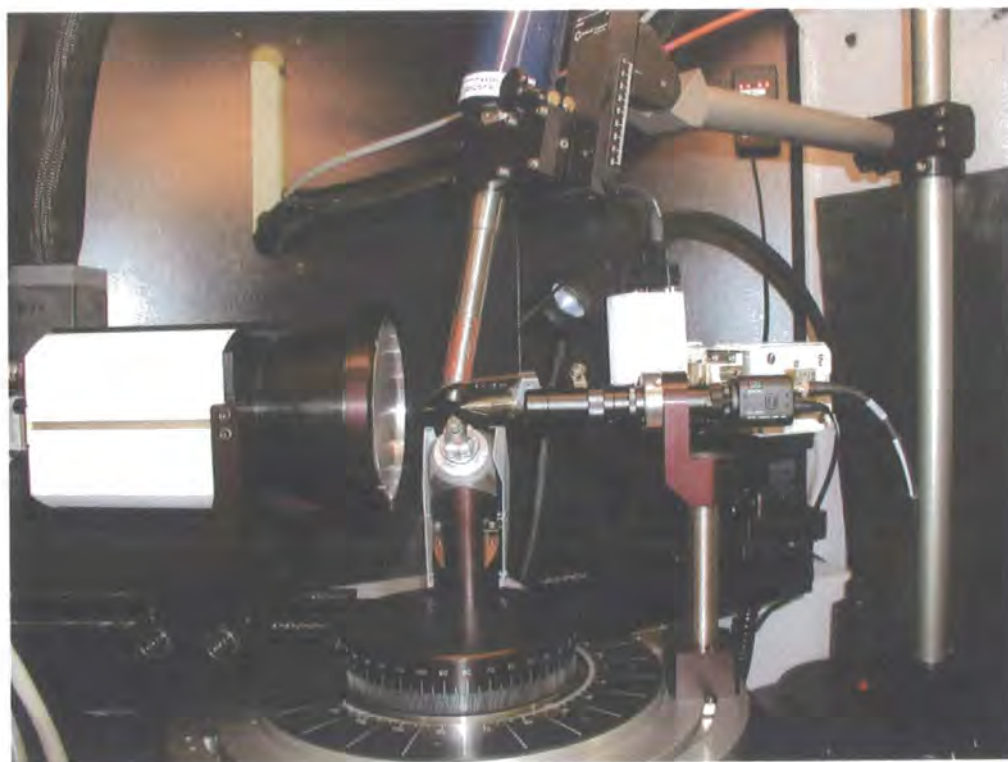


Figure 1.3.2: A SMART 6K diffractometer with Oxford cryostream.

The general advantage of CCD detectors is that the standard data collection time for a four circle diffractometer equipped with a single point detector is of the order of days and for some collections months, whereas the same data collection on a CCD is of the order of hours. The data collection software that Bruker diffractometers use, SMART¹⁹,

allows optimised strategies to be formed for data collection depending on the symmetry of the system and the redundancy of data required. After a MATRIX run has been completed and a unit cell calculation performed, the crystallographer has a good idea of what the basic symmetry of the system is, output from the BRAVAIS routine, this can then be input into further software called ASTRO²⁰. This software reads in the physical parameters of the diffractometer and the unit cell parameters and this combined with the symmetry of the system, is used to calculate the percentage of reciprocal space covered by the data collection proposed.

The Fddd diffractometer²¹.

This is an automated four circle diffractometer, constructed with a Huber 512 Eulerian cradle with offset *ph* circle, see Figure 1.3.3. Data collection is currently much slower than



Figure 1.3.3: The Fddd diffractometer.

that of the SMART diffractometers as it uses a single point detector. However this feature allows individual reflections to be measured with a very high degree of accuracy. It also allows the user to avoid the collection of data that is apparent due to the additional scattering from the beryllium cans that the sample is held in for the

Displex system. Problems can occur with crystal degradation due to X-ray damage caused by the extended amount of time the data collection takes.

1.3.5 Data Reduction, Solution and Refinement

The software that was used for the reduction of the X-ray data from all Bruker machines is SAINT-PLUS²², supplied by BRUKER with the diffractometers. This software integrates frame data (the diffraction pattern collected) and contains programs for the reduction of the raw peak intensities to more useful structure factor data in *.hkl* files. It contains routines to determine the symmetry and hence space group of a system, and provides the user with files prepared for structure solution.

The Fddd diffractometer is operated by custom software Allibon²³ (1996), which also reduces the observed data to standard data files containing *hkl* and F_{obs} information.

Solution and refinement can be performed using a number of programs however all data presented in this thesis were initially solved using XS in SHELXTL²⁴ and the spherical atom model refinements performed in XL of the same suite of programs. Further advanced refinements, for the multipolar method (described in Chapter4), were performed using XD²⁵ after successful spherical atom refinements.

1.4 References

- 1 Bragg, W.L., *Proc. Camb. Phil. Soc.* 1913, **17**, 43-57.
- 2 Glusker, J.P.; Trueblood, K.N., *Crystal Structure Analysis A Primer*. 2nd Ed. Oxford University Press, 1985.
- 3 Giacovazzo, C.; Monaco, H.L.; Viterbo, D.; Scordari, F.; Gilli, G.; Zanotti, G.; Catti, M., *Fundamentals of Crystallography*, Oxford University Press, 1994.
- 4 Glusker, J.P., *Crystal Structure Analysis for Chemists and Biologists*, New York, VCH, 1994.
- 5 Stout, G.H.; Jensen, L.H., *X-ray Structure Determination A Practical Guide* 2nd Ed. Wiley Interscience.
- 6 International Tables for Crystallography. Vol. A. 5th edition. Edited by Th. Hahn. Dordrecht: Kluwer Academic Publishers, 2002.
- 7 Welberry, T. R.; Goossens, D.J.; Edwards A.J.; David, W.I.F., *Acta Cryst.*, 2001, **A57**, 101-109.
- 8 Kerr, K.A.; Ashmore, J.P., *Acta Cryst.*, 1974, **A30**, 176-179.
- 9 XPREP – Reciprocal space exploration Version 6.12, Bruker Analytical X-ray Instruments Inc.: Madison, Wisconsin.
- 10 G. M. Sheldrick, SADABS, Empirical Absorption Correction Program. University of Göttingen, Germany, 1998.
- 11 Skelton, E.F.; Katz, J.L., *Acta Cryst.*, 1969, **A25**, 319-329.
- 12 Havighurst, R.J., *Phys. Rev.*, **28**, 1926, 882-890.
- 13 Patterson, A.L., *Phys. Rev.*, **46**, 1934, 372-376.
- 14 Skelton, E.F.; Katz, J.L., *Acta Cryst.*, 1952, **5**, 60-65.
- 15 Oxford Instruments, TRZ0004
- 16 Archer, J.M.; Lehmann, M.S., *J. Appl. Cryst.*, 1987, **19**, 456-458.
- 17 Cryostream Cooler, Oxford Cryosystems Ltd, Oxford, U.K.
- 18 A.E. Goeta; L.K. Thompson; C.L. Sheppard; C.W. Lehmann; J. Cosier; C. Webster; J.A.K. Howard, *Acta Cryst.*, **C55**, 1999, 1243-1246.
- 19 Bruker Advanced X-ray Solutions SMART for WNT/2000 5.625, Bruker AXS, Madison, Wisconsin, 1997.
- 20 ASTRO 5.007, Bruker Analytical X-ray Instruments Inc.: Madison, Wisconsin, 1997.

- 21 Copley, R.C.B.; Goeta, A.E.; Lehmann, C.W.; Cole, J.C.; Yufit, D.S.; Howard, J.A.K.; Archer, J.M.; *J. Appl. Cryst.*, 1997, **30**, 413-417.
- 22 SAINT-NT, Data Reduction Software, version 6.12; Bruker Analytical X-ray Instruments Inc.: Madison, Wisconsin.
- 23 Allibon, J.R., 1996, *MAD Diffractometer Control Software – AlphaVMS version*. Institute Laue-Langevin (DPT/SCI), Grenoble, France.
- 24 SHELXTL, version 5.1; Bruker Analytical X-ray Instruments Inc.: Madison, Wisconsin.
- 25 Koritzánszky, T.; Howard, S.; Mallinson, P.R.; Su, Z.; Richter, T.; Hansen, N.K., XD – A computer program package for multipole refinement and analysis of electron densities from diffraction data.

Chapter 2:

Introduction to selected organic molecular materials

2.1 General Introduction

The past 20-25 years have seen the birth of a new, interesting field of materials chemistry, namely that of organic charge-transfer (CT) salts. These materials are constructed from discreet molecular building blocks which possess the potential to allow a rearrangement of charge in the solid state. Conducting organic solids are often referred to as “synthetic metals” (synmetals), owing to their ability to conduct electricity. These have been shown also to possess unusual electrical and magnetic properties. The idea of synthetic metals has been apparent since 1911, when McCoy and Moore¹ stated:

“We think, in concluding, that the organic radicals in our amalgams are in the metallic state and, therefore, that it is possible to prepare composite metallic substances from non-metallic constituent elements”

This comment would have been regarded with much scepticism when published but was in fact a very intuitive remark way ahead of its time. The compounds studied in this thesis all show properties not traditionally expected from organic materials, and have evolved building on the ideas first hinted at in 1911. One interesting property that these materials can exhibit is the onset of superconductivity when they are perturbed from ambient conditions by some form of external stimulus. Little^{2,3} was the first to suggest in the mid 1960's that organic solids could not only conduct but if constructed correctly, could also exhibit superconductivity. Little's comments sparked a great deal

of interest in this new area of physical chemistry. It was hoped that since these materials were based on molecular units, by altering these units in subtle and sometimes not so subtle ways, the physical properties could be adjusted in a controllable fashion. The first important steps taken in producing conductors from organic units, were the synthesis of the electron acceptor 7,7,8,8-tetracyano-p-quinodimethane (TCNQ)⁴ and tetrathiafulvalene (TTF)⁵, an electron donor molecule Figure 2.1.1.

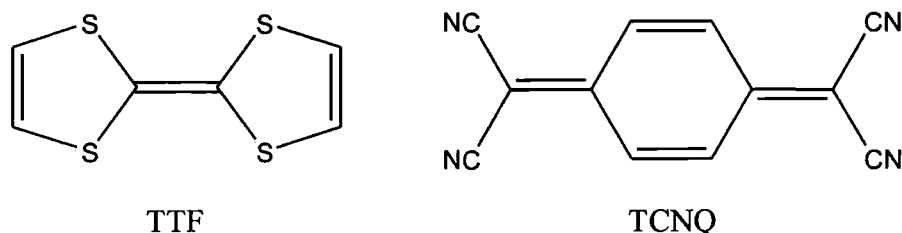


Figure 2.1.1: TTF and TCNQ molecular diagrams.

Ferraris *et al*⁶ mixed TTF and TCNQ to obtain the charge transfer salt TTF-TCNQ, now known as the first true organic metal. It is metallic to 54K. The interest of many researchers was the development of high temperature superconductors that

1962	Synthesis of TCNQ
1963	Synthesis of TCNQ Salts [Cs ₂ (TCNQ) ₃]
1970	Synthesis of TTF
1973	TTF-TCNQ synthesised: first organic metal
1976	TMTSF synthesised
1978	ET synthesised
1979	TMTSF-DMTCNQ synthesised: $\sigma = 10^5(\Omega^{-1} \text{cm}^{-1})$ at 10 kbar and 1 K
1979	Selenium-based Bechgaard salts synthesised: (TMTSF) ₂ X, where X = monovalent anion Superconductors under pressure at T \approx 1 K
1981	(TMTSF) ₂ ClO ₄ = first organic superconductor at ambient pressure at 1.4 K
1983	(BEDT-TTF) ₂ ReO ₄ - SC under pressure at T _c \cong 1 K – first S-based SC
1984-1986	β -(BEDT-TTF) ₂ X, where X = I ₃ ⁻ , IBr ₂ ⁻ , AuI ₂ ⁻ Superconductors synthesised, where T _c = 1.4, 2.8 and 5.0 K respectively
1986-1989	Ni(dmit) ₂ ⁿ⁻ salts synthesised with T _c ranging from 1.62-5.9 K at pressures from 7-24 kbar
1987-1988	κ -(ET) ₂ Cu(SCN) ₂ synthesised: highest T _c at 10.4 K (MDT-TTF) ₂ AuI ₂ synthesised with T _c at 4.5 K (DMET) ₂ X salts synthesised, where X = AuCl ⁻ , AuBr ⁻ , Au(CN) ₂ ⁻ , I ₃ ⁻ and IBr ₂ ⁻ with T _c 's ranging from 0.47-1.9 K. Only the I ₃ ⁻ , IBr ⁻ , AuCl ⁻ and the κ -phase of AuBr ₂ ⁻ salts are ambient pressure superconductors.
1989	BEDO-TTF synthesised and numerous salts prepared New superconductors synthesised, (ET) ₂ NH ₄ Hg(SCN) ₄ , T _c at 1.15 K, (BEDO-TTF) ₃ Cu ₂ (NCS) ₃ , T _c = 1.1 K
1990	κ -(ET) ₂ Cu[N(CN) ₂]Br, T _c = 11.6 K
1990	κ -(ET) ₂ Cu[N(CN) ₂]Cl, T _c = 12.8 K at 0.3 kbar

Table 2.1.1: Early chronology of synthetic organic conductors and superconductors.

would be of commercial value. The drive for better organic conductors and high temperature superconductors caused the rapid growth of this field, as shown by the early chronology of this field Table 2.1.1, taken from *Organic Superconductors*⁷.

Superconductivity is a physical state that can be well characterised. The phenomenon is linked to some very specific physical effects, not least that the material's electrical resistance (ρ) drops to zero at a specific temperature (T_c) and/or pressure. The material's specific heat increases discontinuously with the onset of superconductivity (T_c), and there are also phenomena such as the expulsion of magnetic fields from the superconducting body (Meissner effect^{8,9}). A material can be shown to be in a *superconducting* state by the presence of Shubnikov-de Haas^{10,11} (SdH) oscillations in magnetoresistance measurements.

The discovery of a superconducting state in $(\text{TMTSF})_2\text{PF}_6$ was realised in early 1979 by Bechgaard *et al*¹² and this provoked more excitement in the field. Bechgaard's important advancement was to use an inorganic monovalent anion instead of TCNQ and a modification of the TTF molecule. $(\text{TMTSF})_2\text{PF}_6$ required the application of between 5 – 12 kbar at a temperature of 1-2 K to reach its superconducting state. Two years later, in 1981, the first ambient pressure organic superconductor was formed using a derivative of the work of Bechgaard¹³, with $T_c = 1.4$ K. It was $(\text{TMTFS})_2\text{ClO}_4$.

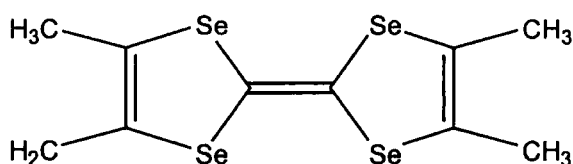


Figure 2.1.2: The TMTSF molecule

After substitution of TCNQ, by different organic anions, the active research focused on the development of new electron donors. These were mainly based on the TTF backbone, such as TMTSF (above) and then further on bis(ethylenedithio)-tetrathiafulvalene (BEDT-TTF).

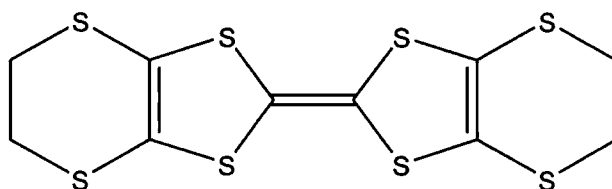


Figure 2.1.3 The BEDT-TTF molecule.

BEDT-TTF (ET) has become the major electron donor in organic CT salts, as it contains twice the number of chalcogenides than there are Se atoms in TMTSF. Many unsymmetrical electron donors have also been prepared, such as dimethyl(ethylenedithio)diselenadithiafulvalene (DMET)¹⁴ and methylene dithiopropylenedithiotetrathiafulvalene MPT¹⁵ Figure 2.1.4.

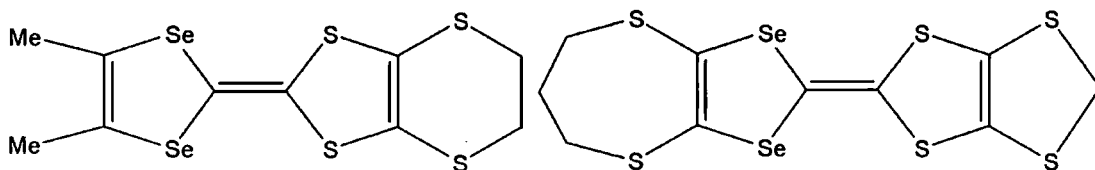


Figure 2.1.4: The DMET, left, and MPT, right, molecules

A general rule is that non symmetrical electron donors have T_c 's lower than the CT salts prepared with symmetric electron donors. ET molecules in these organic molecular materials are usually found in one of three stacking motifs, these are shown in Figure 2.1.5, taken from Lang and Müller¹⁶ showing the different phases of $(\text{ET})_2\text{I}_3$.

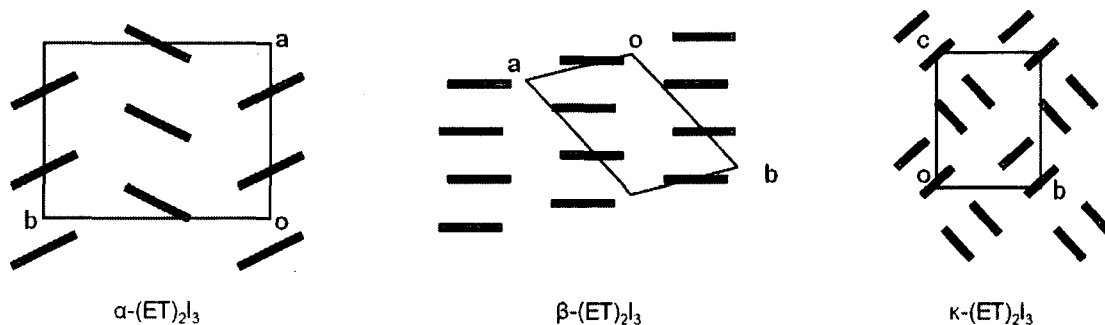


Figure 2.1.5: Schematic showing the different packing motifs of $(\text{ET})_2\text{I}_3$.

As the organic species in the CT salts could be systematically modified and owing to the wealth of inorganic anions that were accessible, it was suggested by Ginzburg¹⁷ that organic materials were the best candidates for new superconductors. The materials discussed are still far from the desired technologically applicable CT salts envisioned. The compounds do however provide a systematic route to the analysis of some certain

physical phenomena that have been observed in the current literature^{18,19} for example superconductivity in molecular materials.

2.2 Introduction to the compounds studied

The first molecular superconductor containing paramagnetic metal ions (β "-(BEDT-TTF)₄[(H₂O)Fe(C₂O₄)₃]C₆H₅CN), reported in 1995²¹ consisted of Fe as the central metal ion of the oxalate layers and Ph-CN as the guest molecule in the cavity formed in these layers. The needle shaped polymorph of this material became superconducting below 8.5 K, while above this temperature it showed metallic behaviour. The superconducting transition was sharp, showing no signs of hysteresis within the limits of the temperature controller ($\pm 0.1^\circ$). Since this first publication of these materials, there has been considerable interest in the formation of iso-structural compounds which may have similar physical properties²²⁻²⁷. The central metal ion and the guest molecule in the metal-oxalate network have been exchanged systematically to see the change, if any, in physical properties of the bulk material and to increase our understanding of these interesting properties. The year 2001 saw the publication of the iso-structural Cr, Fe, Co and Al salts^{23,23}.

The work herein concentrates on one class of organic metals, namely those that have separation into well defined organic and inorganic layers, forming charge transfer salts. This type of charge transfer salt has become an attractive synthetic target since the materials can show a range of novel physical properties. The structure – property relationship that these materials possess is not entirely understood, and their structural parameters have not been fully explored.

The compounds investigated contain some common features, namely that of ET molecules forming one organic layer in the structure. These organic layers are, in most cases, separated by a hexagonal honeycomb layer, Figure 2.2.1, of transition metal atoms ligated by three bi-dentate oxalate ligands. The central metal atom and the symmetry generated equivalent atoms, form three of the vertices of the honeycomb

structure, with the other three vertices made up of another counter ion and its symmetry equivalents. In most cases studied, this counter ion was a protonated water molecule.

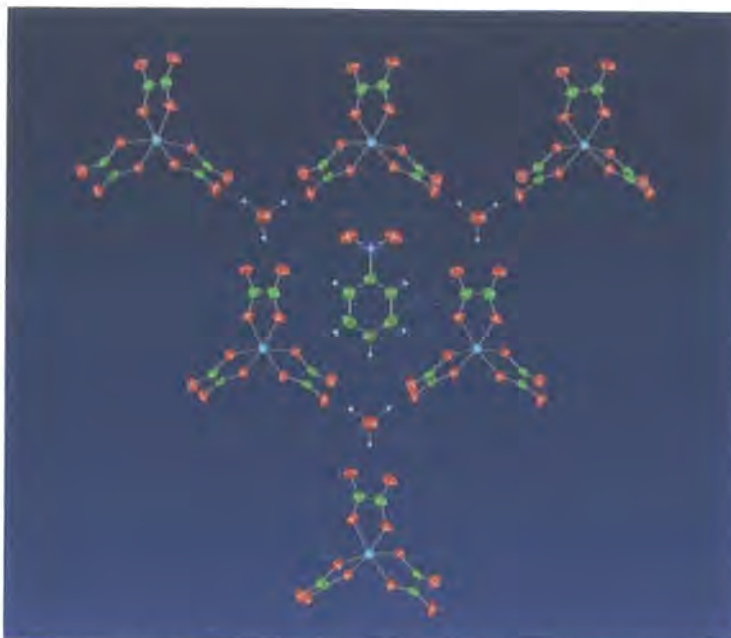


Figure 2.2.1: Hexagonal packing of anionic layer including a guest molecule, taken from the β'' -(ET)₄[(H₃O)Ga(C₂O₄)₃] PhNO₂ structure^{18,19}.

CT salts of this type have been synthesised successfully since the mid 1980s²⁰. The cationic layers stack in a predominantly β'' arrangement. This type of stacking configuration, a slightly twisted version of the central system shown in Figure 2.1.5, facilitates many short S – S intermolecular contacts and these are shown and discussed in Chapter 3. These S – S contacts allow overlap of the ET molecular orbitals, potentially creating a two dimensional conduction band through the crystal.

The anionic layers adopt a pseudo hexagonal pattern (Figure 2.1.2) with the cavity occupied by a suitably chosen guest molecule. In the case of Figure 2.1.2 the guest molecule is nitrobenzene. The inclusion of a guest molecule in the cavity can cause minor deviations from a perfect hexagonal lattice. The guest molecules align in a parallel mode to these deviations, indicating the presence of guest host interaction.

It can be seen clearly from the above, that the system under scrutiny can be adapted in many ways, the ligating molecules to the central metal atom, the guest molecule in the cavity and the additional counter ion present. Manipulation of these fragments in the structure can allow a careful structural analysis to be performed on a variety of very

similar compounds that do not possess the same physical characteristics, potentially shedding light on the interactions responsible for the physical properties of the materials.

The compounds presented in this thesis were investigated for a number of reasons: to confirm a structure at a particular temperature, or to elucidate a structure that had been measured previously yet the structure had failed to solve, or to carry out a full variable temperature structural analysis.

The primary case for study was β'' -(ET)₄[(H₃O)Ga(C₂O₄)₃]PhNO₂^{18,19}, a crystal for which the temperature – resistivity relationship is not understood. A plot of this relationship is shown in Figure 2.2.2. Previous studies²⁸ had suggested that the superconductivity was a volume property and though the volume is undoubtedly involved in the complex electrical properties of these structures, it seems unlikely that it can explain the properties observed for β'' -(ET)₄[(H₃O)Ga(C₂O₄)₃]PhNO₂ which follow no basic function.

Resistivity vs Temperature

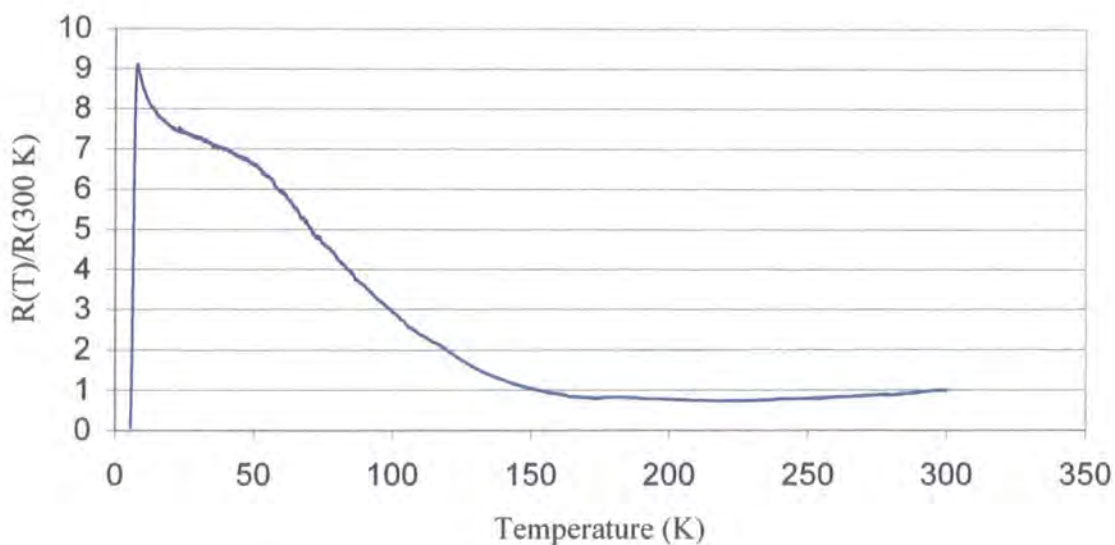


Figure 2.2.2: Graph showing the change in resistivity of β'' -(ET)₄[(H₃O)Ga(C₂O₄)₃]PhNO₂ with temperature.

This sample, with nitrobenzene as the guest molecule, deviates from classical behaviour of both conductors and insulators markedly. Crystals of β'' -(ET)₄[(H₃O)Ga(C₂O₄)₃]PhNO₂ exhibit metallic behaviour at room temperature, and

continue to do so until 160 K with the resistivity gradually reducing, i.e. classical metallic behaviour. However upon cooling below 160 K the resistivity increases at a much faster rate. This increase in resistance has a shoulder at 55 K and then continues to rise again. There is a sharp increase in the resistivity between 25 and 7.5 K at which point a sharp maximum is reached and the resistance falls to zero (see Figure 2.2.2), entering a superconducting state. This material therefore passes through a metal-semiconductor transition (MST) ≈ 160 K and then further passes through a semiconductor-superconductor transition (SST) ≈ 7.2 K.

An iso-structural pyridine 'guest' sample was also analysed and it shows similar properties but without the sharp transitions. It shows a broad MST at 130K and re-enters the metallic state at 60 K, then has a smooth transition to its superconducting state, with $T_c = 1.5$ K. All electrical resistivity measurements between 1 K and 300K were taken on single crystals at the R.I. using an Oxford Instruments Maglab 2000 with EP probe²⁹.

Rashid *et al.*³⁰ suggested that the guest molecules' aromatic rings might somehow play a templating role in stabilising the crystal structures, given the hexagonal cavity in which they were always found. However Rashid *et al.*³⁰ disproved this subsequently, showing the same hexagonal cavities were to be found in the crystal structure of β'' -(ET)₄[(H₃O)Cr(C₂O₄)₃]CH₂Cl₂. The iso-structural Ga salt has now been formed, and the results are presented here.

Further manipulation of the structure by changing the guest molecule from the substituted phenyl ring to 18-crown-6-ether, provided crystals which showed another rare phenomenon: proton conductivity in the solid state. The possibility of this phenomenon occurring in these structures was noted by Akutsu-Sato *et al.*³¹ when the CT salts β'' -(ET)₄[(NH₄)M(C₂O₄)₃]₂18-crown-6-ether·(H₃O)₂·(H₂O)₅, where M = Cr, Ga or Fe and x = 2 or 3, were reported. The preliminary results of both the electrical and the proton resistivities are shown in Figures 2.2.3 and 2.2.4. These preliminary results showed interesting features that increased the desire for a full structural understanding of this material at different temperatures.

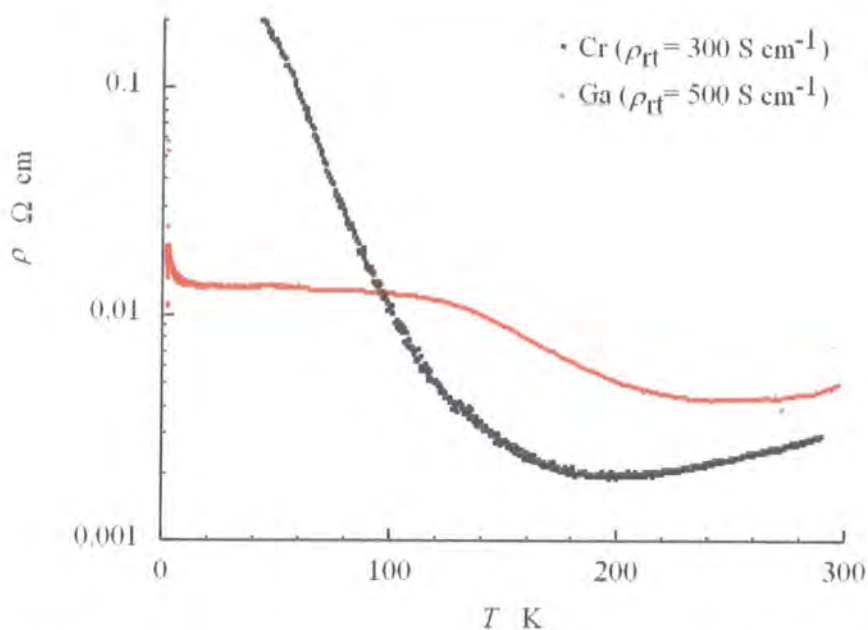


Figure 2.2.3: The electrical Resistivity of $\beta''(ET)_4[(NH_4)M(C_2O_4)_3]_2 18\text{-crown-6-ether} \cdot (H_3O)_2 \cdot (H_2O)_5$ $M = \text{Cr or Ga}$, $x = 2$ or 3 .

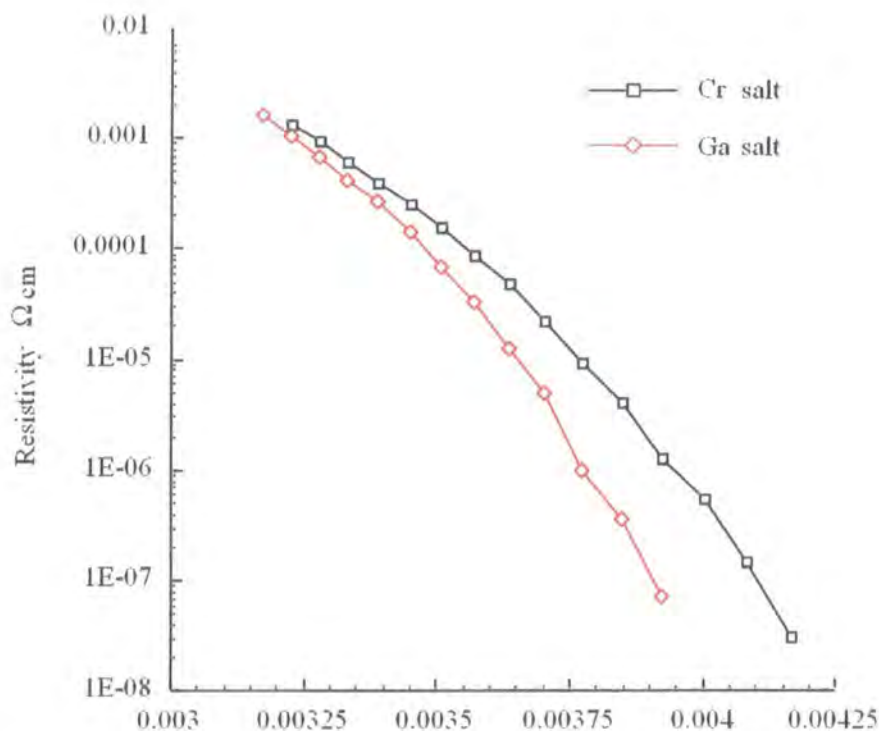


Figure 2.2.4: The preliminary proton resistivity of $\beta''(ET)_4[(NH_4)M(C_2O_4)_3]_2 18\text{-crown-6-ether} \cdot (H_3O)_2 \cdot (H_2O)_5$ $M = \text{Cr or Ga}$, $x = 2$ or 3 .

Further measurements of these values were made by Akutsu-Sato *et al*^{32,33} and these show that the proton conductivity of this material was very high.

The charge transfer from the organic ET molecules in these compounds is approximately +0.5 per molecule and this achieves charge balance needed for electro neutrality for the crystal. A reliable method for analysing the charge supported by an ET molecule was pioneered by Guionneau *et al.*³⁴ this method is based on the ratio of bond lengths in the molecules. It was thought originally that the central C = C double bond was sufficient to categorise the relative charge localised on an ET molecule, but this method was changed to use the 4 different central bonds of the molecule in order to reduce errors in the analysis. The bond lengths used are a sensitive experimental indicator to the charge supported on an ET molecule, as the bonds analysed are the most sensitive to oxidation of the molecule. This method is outlined here, the ET molecule shown in Figure 2.2.5 highlights the chemically equivalent bonds used in this analysis since oxidation of the molecule lengthens *a* and *d* and shortens *b* and *c*.

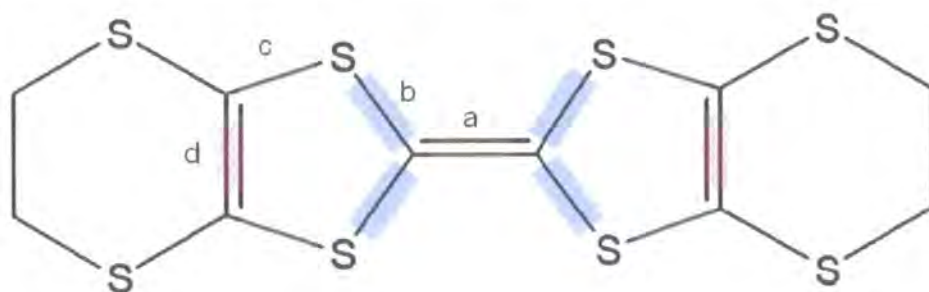


Figure 2.2.5: ET molecule showing chemically equivalent bonds, highlighted in the same colour, used in the charge analysis of the molecule.

A simple equation can then be constructed to calculate the charge supported by the molecule (Equation 2.1) from experimentally determined bond lengths.

$$Q = 6.347 - 7.463\delta, \text{ where } \delta = (b + c) - (a + d)$$

Equation 2.1: Calculation of the charge carried by an ET molecule, *a, b, c, d* are show in Figure 2.2.5.

The method was extensively tested showing reproducible results when applied to high quality structural data. Data collected on neutral species of ET molecules^{35,36} and of TTF³⁷ (gas phase from electron diffraction), have been published and give excellent agreement with this approach, the most recent of these³³ are shown in Table 2.2.1 for comparative purposes in this work. These bond lengths lead to the following result:

$$\delta = (1.756 + 1.760) - (1.343 + 1.333) = 0.84$$

$$Q = 6.347 - 7.463 \times 0.84 = 0.078 \approx 0$$

Bond	Length (Å)
<i>a</i>	1.343(4)
<i>b</i>	1.756(3)
<i>c</i>	1.760(3)
<i>d</i>	1.333(4)

Table 2.2.1: Averaged, chemically equivalent, bond lengths determined experimentally in neutral ET molecules.

The relative ordering of the charges on the ET molecules in a particular structure at a given temperature, may prove to be a useful indicator of the material's macroscopic physical properties. Takahashi³⁶ describes the existence of two kinds of ET molecules in the insulating state of a compound where half of the ET molecules become nearly neutral and the other half have a much greater associated charge density than in the metallic state. It is believed that the charge is equally spread across the ET molecules in the metallic state, therefore with the combination of these two ideas, it should be possible to follow the transitions of the electrical properties of a CT material of this type from variable temperature structural analysis. Gaultier *et al.*³⁸ completed a similar study to that described for $\text{ET}_3\text{Cl}_2 \cdot (\text{H}_2\text{O})_2$ at three temperatures 190, 130 and 10 K. The results of the study showed that charge localisation occurred to different extents in the crystallographically independent ET molecules. The amount of charge located on each ET molecule was found to be temperature dependent.

Computational approaches have, until recently, been very limited in this field, however with the increasing reliability with which theoretical structure calculations can be treated and the rapid growth in computing power this has become a possibility. French *et al.*³⁹ and Kawakami *et al.*⁴⁰ recently published results of calculations based on various systems with the common feature of the ET molecule. Although these types of calculation are outside the scope of this work, they show the vibrancy of this field as an area of interest for many research groups, ranging from analytical, synthetic, materials to theoretical chemistry.

A review of magnetic molecular conductors by Coronado and Day⁴¹ provides further detailed background to this field.

References:

- 1 McCoy, H.N.; Moore, W.C., *J. Am. Chem. Soc.*, 1911, **33**, 271.
- 2 Little W.A., *Phys. Rev.* 1964, **134A**, 1416.
- 3 Little, W.A., *Sci. Am.* 1965, **212**, 21.
- 4 Melby, L.R.; Harder, R.J.; Hertler, W.R.; Mahler, W.; Benson, R.E.; Mochel, W.E., *J. Am. Chem. Soc.*, 1962, **84**, 3374.
- 5 Coften., D.L.; Garrett, P.E., *Tetrahedron Lett.*, 1969, 2043.
- 6 Ferraris, J.; Cowan, D.O.; Walatka, V.J.; Perlstein, J.H., *J. Am. Chem. Soc.*, 1973, **95**, 948.
- 7 Williams, J.M.; Ferraro, J.R.; Thorn, R.J.; Carlson, K.D.; Geiser, U.; Wang, H.H.; Kini, A.M.; Whangbo, M-H, *Organic Superconductors Including Fullerenes*, Prentice Hall 1992.
- 8 Meissner, W.; Oschenfeld, R., *Naturwiss.*, 1933, **21**, 787.
- 9 Rohlf, James William, *Modern Physics from A to Z*, Wiley 1994.
- 10 Singleton, J., *Rep. Prog. Phys.* **63**, 1111, 2000.
- 11 Ito, H.; Hasegawa, Y.; Hanada, M.; Kato, K.; Yamada, J.; Saito, G., *Physica C* **388-389**, 2003, 593-594.
- 12 Bechgaard, K.; Jacobsen, C.S.; Mortensen, K.; Pedersen, M.J.; Thorup, N.; *Solid. State. Commun.*, 1980, **33**, 1119.
- 13 Bechgaard, K.; Carneiro, K.; Rasmussen, F.G.; Olsen, K.; Rindorf, G.; Jacobsen, C.S.; Pedersen, M.J.; Scott, J.E., *J. Am. Chem. Soc.*, 1981, **103**, 2440.
- 14 Kikuchi, K.; Ishikawa, Y.; Saito, K.; Ikemoto, I.; Kobayashi, K. *Acta Cryst.* 1988, **C44**, 466.
- 15 Beno, M.A.; Kini, A.M.; Wang, H.H.; Tytko, S.F.; Carlson, K.D.; Williams, J.M. *Acta Cryst.* 1988, **C44**, 1223.
- 16 Lang, M.; Müller, J., *Organic Superconductors*, 2003.
- 17 Ginzburg, V.L., *Phys. Today*, 1989, **42**, 9 (March).
- 18 Akutsu, H.; Akutsu-Sato, A.; Turner, S.S.; Le Pevelen, D.; Day, P.; Laukhin, V.; Klehe, A-K.; Singleton, J.; Tocher, D.A.; Probert, M.R.; Howard, J.A.K., *J. Am. Chem. Soc.*, 2002, **124**, 12430.

- 19 Akutsu, H.; Akutsu-Sato, A.; Turner, S.S.; Day, P.; Tocher, D.A.; Probert, M.R.; Howard, J.A.K.; Le Pevelen, D.; Klehe, A-K.; Singleton, J.; Laukhin, V.N., *Syn. Metals* **137**, 2003, 1239-1240.
- 20 Bender, K.; Hennig, I.; Schweitzer, D.; Dietz, K.; Endres, H.; Keller, H.J. *Mol. Cryst. Liq. Cryst.* **1984**, *108*, 359.
- 21 Graham, A.W.; Kurmoo, M. and Day, P., *J. Chem. Soc. Chem. Commun.*, **1995**, 2061-2062.
- 22 Rashid, S.; Turner, S.S.; Day, P.; Howard, J.A.K.; Guionneau, P.; McInnes, E.J.L.; Mabbs, F.E.; Clark, R.K.H.; Firth, S. and Biggs, T., *J. Mater. Chem.*, **2001**, *11*, 2095-2101.
- 23 Martin, L.; Turner, S.S.; Day, P.; Guionneau, P.; Howard, J.A.K.; Hibbs, D.E.; Light, M.E.; Hursthouse, M.B.; Uruchi, M. and Yakushi, K., *Inorg. Chem.* **2001**, *40*, 1363-1371.
- 24 Martin, L.; Turner, S.S.; Day, P.; Malik, K.M.A.; Coles, S.J. and Hursthouse, M.B., *Chem. Commun.*, **1999**, 513-514.
- 25 Martin, L.; Turner, S.S.; Day, P.; Mabbs, F.E. and McInnes, E.J.L., *Chem. Commun.*, **1997**, 1367-1368.
- 26 Setifi, F.; Golhen, S.; Ouahab, L.; Turner, S.S; and Day, P., *Cryst. Eng. Comm.*, **2002**, *1*.
- 27 Kurmoo, M.; Graham, A.W.; Day, P.; Coles, S.J.; Hursthouse, M.B.; Caulfield, J.L.; Singleton, J.; Pratt, F.L.; Hayes, W.; Ducasse, L. and Guionneau, P., *J. Am. Chem. Soc.* **1995**, *117*, 12209-12217.
- 28 Schwenk, H.; Parkin, S.S.P.; Lee, V.Y.; Greene, R.L., *Phys. Rev. B.*, **34**, *5*, 3156-3161.
- 29 Maglab 2000 probe: Oxford Instruments.
- 30 Rashid, S.; Turner, S.S.; Le Pevelen, D.; Day, P.; Light, M.E.; Hursthouse, M.B.; Firth, S. Clark, R.J.H., *Inorg. Chem.* **2001**, *40*, 5304-5306.
- 31 Akutsu-Sato, A., *Private communication, Royal Institution* 2003.
- 32 Akutsu-Sato, A.; Akutsu, H.; Turner, S.S.; Day, P.; Probert, M.R.; Howard, J.A.K.; Akutagawa, T.; Takeda, S.; Nakamura, T.; Mori, T., *Angew. Chem. Int. Ed.* **2005**, *44*, 292-295.
- 33 Akutsu-Sato, A.; Akutsu, H.; Turner, S.S.; Le Pevelen, D.; Day, P.; Light, M.E.; Hursthouse, M.B.; Akutagawa, T.; Nakamura, T., *Syn. Metals* **135-136**, 2003, 597-598

- 34 Guionneau, P.; Kepert, C.J.; Bravic, G.; Chasseau, D.; Truter, M.R.; Kurmoo, M.; Day, P., *Syn. Metals*. **86**, 1997, 1973-1974.
- 35 Kobayashi, H.; Kobayashi, A.; Sasaki, Y.; Saito, G.; Inokuchi, H., *Chem. Lett.*, 1984, 183.
- 36 Takahashi, T., *J. of Phys. and Chem. of Solids*. **62**, 2001, 105-108.
- 37 Hargittai, I.; Brunvoll, J.; Kolonits, M.; Khodorkovsky, V., *J. Mol. Struct.*, **317**, 1994, 273-277.
- 38 Gaultier, J.; Hébrard-Bracchetti, S.; Guionneau, P.; Kepert, C.J.; Chasseau, D.; Ducasse, L.; Barrans, Y.; Kurmoo, M. and Day, P., *J. Sol. State Chem.* **145**, 496-502, 1999.
- 39 French, S.A.; Catlow, C.R.A., *J. of Phys. and Chem. of Solids* **65**, 2004, 39-49.
- 40 Kawakami, T.; Taniguchi, T.; Nakano, S.; Kitagawa, Y.; Yamaguchi, K., *Polyhedron* **22**, 2003, 2051-2065.
- 41 Coronado, E.; Day, P., *Chem. Rev.* 2004, **104**, 5419-5448.

Chapter 3:

Selected studies of organic molecular crystals.

All crystals presented in this chapter were synthesised in the Royal Institution (R.I.) of Great Britain, London, where measurements on the physical properties were also conducted. The author claims no credit for these. The crystallographic studies were undertaken to increase the understanding of these compounds at the molecular level and hopefully correlate structural changes with temperature to the observed physical properties. It was believed that this increased understanding could lead to the development of molecular systems being synthesised with desired characteristics and that these materials could be of commercial importance.

3.1 The study of the structure of :



The asymmetric unit for this structure is shown below in Figure 3.1.1. The physical properties examined at the R.I. are intriguing and the graph showing temperature dependence of the electrical resistivity is displayed in Figure 2.2.2 in Chapter 2.

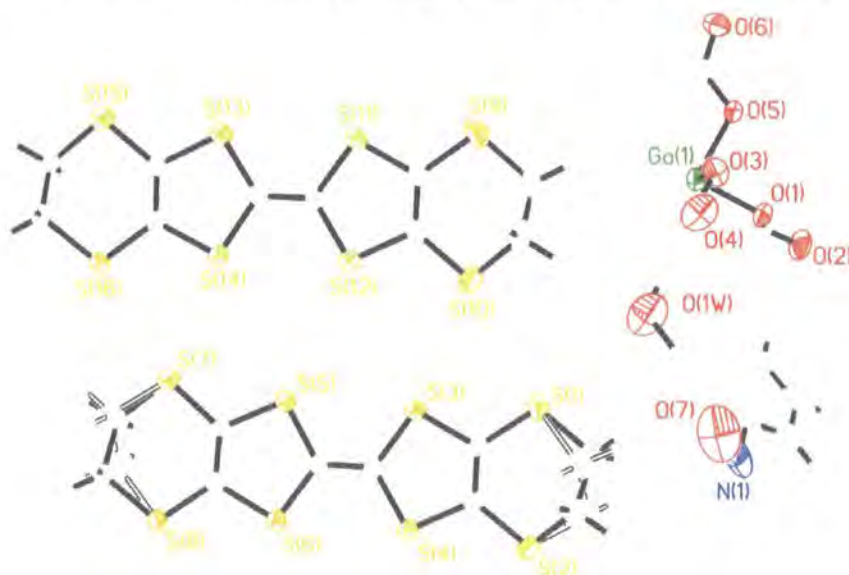


Figure 3.1.1 Asymmetric unit of β'' -(ET)₄[(H_3O) $Ga(C_2O_4)_3$]PhNO₂ at 290 K.

As with all of the molecular systems studied, the bulk properties of the material are linked fundamentally with the packing of the molecular fragments in the structure. This packing is difficult or impossible to predict, given the diversity of the molecules present in each structure, hence the enormous value of the X-ray diffraction experiment.

The crystals were all very intense dark red/black coloured needles, with shiny almost metallic faces. One problem that became apparent from a first visual survey was that many of the crystals contained obvious imperfections. The majority of the imperfections manifested as vortex shaped holes starting in the centre of the crystal broadening to one of the small faces of the crystal. This could be attributed to the crystallisation technique employed, i.e. crystallisation possibly occurring too quickly and an ordered nucleation only possible towards the outer edges of the crystal. These imperfections were not seen easily, due to the low transmittance of visible light through the sample, however they were noticed because light was reflected from the vortex faces as the crystals were manoeuvred under the microscope.

Preliminary data were collected at room temperature in order to judge the quality of the crystals until a suitable crystal was found for multi-temperature analysis. The room temperature cell parameters are shown in Table 3.1.1:

Crystal system	Monoclinic
a (Å)	10.3547(4)
b (Å)	20.1508(7)
c (Å)	35.5424(12)
β (°)	92.571(10)
Volume (Å ³)	7408.7(5)

Table 3.1.1: Room Temperature unit cell dimensions for:



Once a suitable crystal of $\beta''\text{-(ET)}_4[(\text{H}_3\text{O})\text{Ga}(\text{C}_2\text{O}_4)_3]\text{PhNO}_2$ was found, it was mounted permanently on hair fibre, using a very small amount of epoxy resin to enable room temperature and low temperature data collections.

Data were recorded on a Bruker SMART 1 K diffractometer at room temperature, to give a desired high redundancy of reflections. Due to the presence of a heavy elements (S and Ga) the crystal, although small, diffracted strongly and afforded data to the maximum resolution of the detector in its standard position ($2\theta = -30^\circ$). This allowed the data to be collected using an exposure of only 10s / frame. A hemisphere data collection therefore took approximately 14 hours.

Integration and data merging were performed by SAINT³ and structure solution and refinement carried out in the SHELXTL⁴ package. The room temperature structure was solved and refined in space group C2/c. Figure 3.1.2 shows the packed unit cell contents, viewed down the *b*-axis.

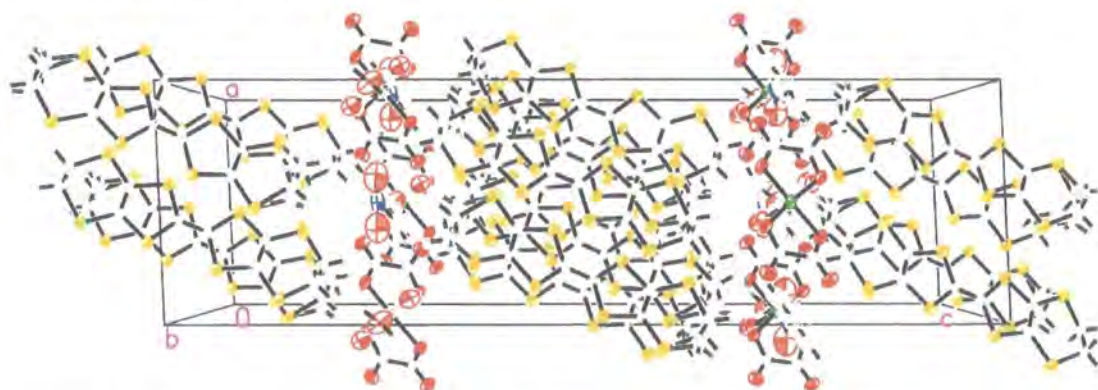


Figure 3.1.2: The packed unit cell of β'' -(ET)₄[(H₃O)Ga(C₂O₄)₃]PhNO₂ viewed down the *b*-axis (Ga: dark green, S: yellow, O: red, N: blue, C: grey, H: light green).

Although this view at first appears confusing, it clearly shows the discrete packing of the ET molecules separated from the anionic layer of the Ga-oxalate network. The interaction between these layers seems to be primarily between the end of one of the ET molecules and the nitrobenzene guest molecule that sits in the hexagonal cavity of the Ga-oxalate layer, as shown in Figure 3.1.3 below. It is noteworthy that even though this structure was determined and refined at room temperature, there is very little disorder in the structure. In fact the only disorder seen is that in the terminal ethylene groups of one of the ET molecules. This is a common feature seen in previous studies of similar compounds⁵⁻⁸.

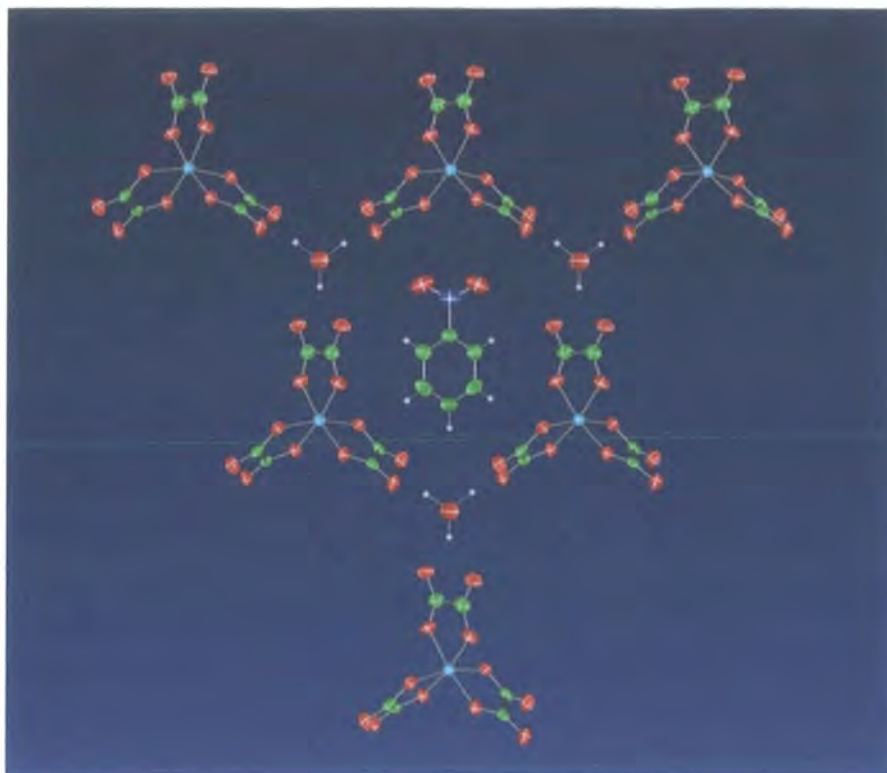


Figure 3.1.3: The hexagonal cavity formed by the Ga-oxalate species and protonated water molecules encapsulating the nitro benzene guest molecule.

This disorder was sufficient to require modelling of these ethylene groups of the ET molecule in two separate positions, equating to the flipping of the conformation of the terminal ethylene groups with approximately 60:40 % occupancies of the C atoms. Thermal parameters are quite large at room temperature and it would be impossible to resolve the fully anisotropic thermal parameters for these disordered atoms, as the values would be highly correlated with their occupancy factors and could potentially destabilise the least squares refinement. These ethylene groups are modelled with single site occupancy when the structure is cooled to temperatures lower than 100 K as the disorder is no longer present, shown in Figure 3.1.4. The disorder at various temperatures is shown in Figure 3.1.5, it displays the observed electron density maps in the mean plane of 4 partially occupied carbon atom sites of the most disordered terminal ethylene group (C1 – C2) of the ET molecule.

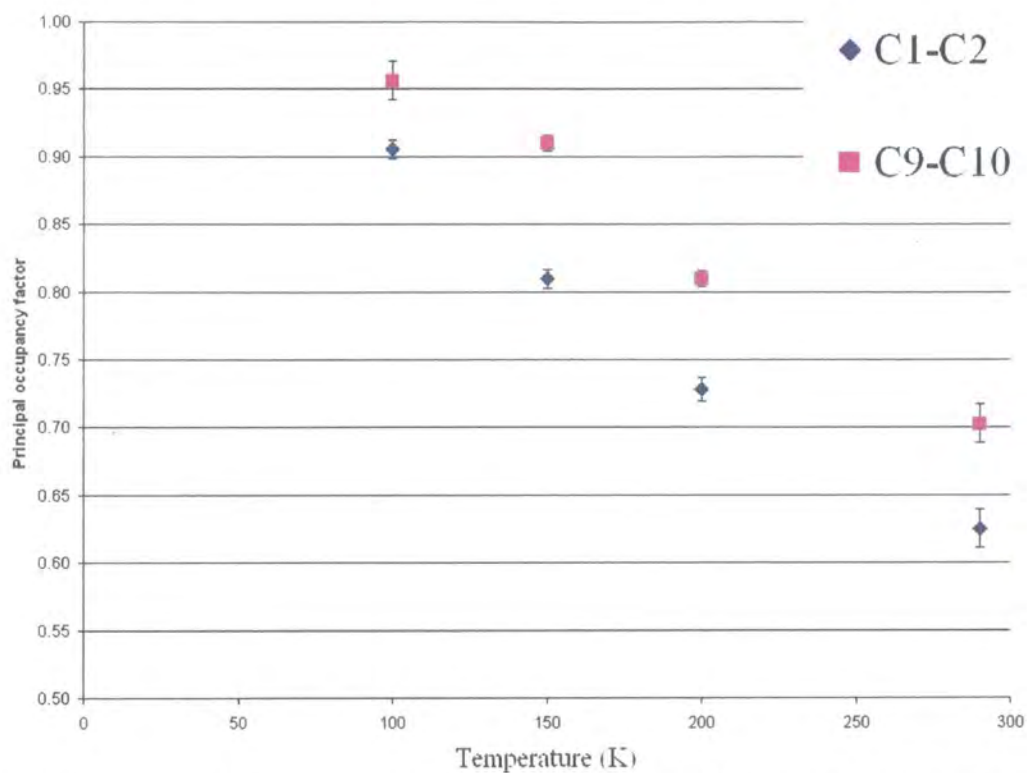


Figure 3.1.4: Graph showing the variation of occupancy factors with temperature for the disordered ethylene groups.

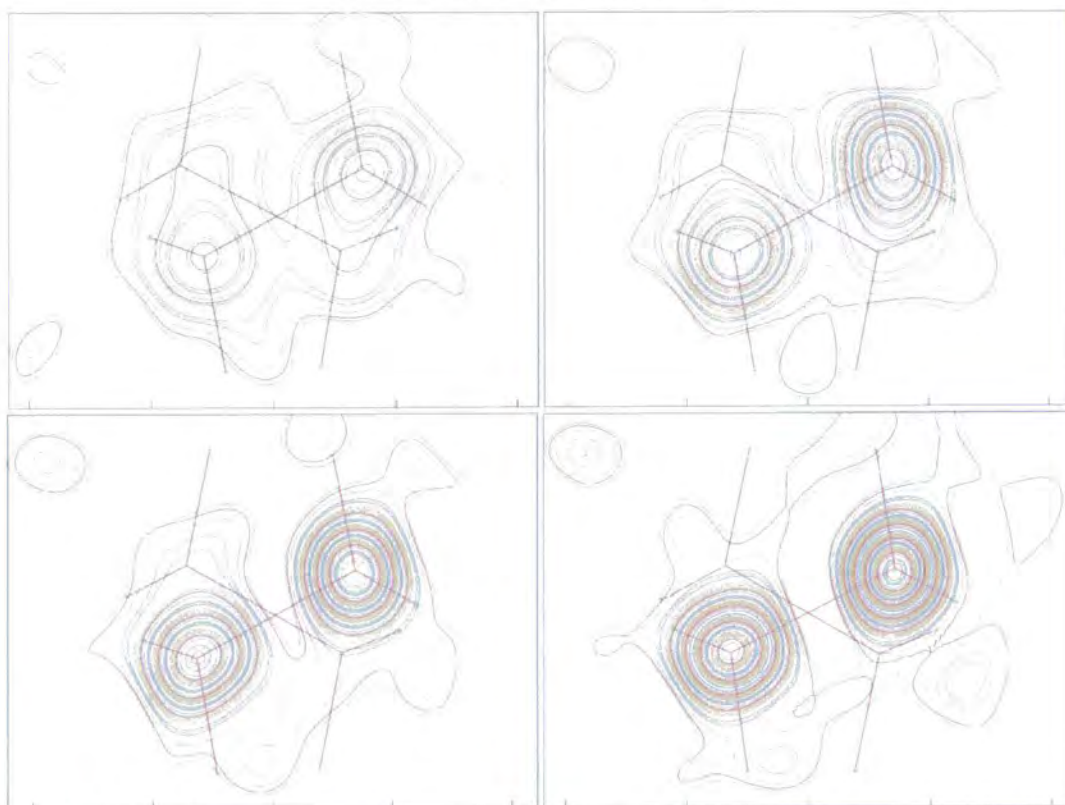


Figure 3.1.5: F_o maps viewed through the plane of the disordered terminal ethylene group (C1, C2) of the disordered ET molecule, contours at $0.1 \text{ e}/\text{\AA}^3$, upper left 290 K, upper right 200 K, lower left 150 K and lower right 100 K.

The disorder could be due to thermal energy allowing the energy barrier between the two conformations to be overcome, resulting in a smearing of atomic positions through the crystal, or it could be that statistically in every 10 ET molecules 4 are in opposite conformations i.e. a static disorder, although this is unlikely as the disorder is resolved on cooling the sample to low temperature. The presence of the disorder in one of the crystallographically independent ET molecules and not in the other would seem to highlight a difference in the energy minima in which they both sit. Analysis of the shortest intermolecular interactions (C-H...O) to these atomic sites proves inconclusive, with the disordered atoms having shorter interaction distances at the higher temperatures than the ordered atoms. The shortest interaction for the disordered ET molecule is that between the terminal hydrogen atoms and the oxygen atoms of the nitro benzene molecule (H1B...O7). This distance increases with decreasing temperature from approximately 2.38 to 2.42 Å. A secondary interaction between the other terminal hydrogen atom of the same group to an oxygen of the oxalate entity decreases with decreasing temperature from approximately 2.87 to 2.68 Å, although these O...H distances are calculated from H positions that have been placed geometrically. In contrast the ordered ET molecule is positioned so that the alternative possible conformation for the ethylene groups are sterically hindered by one of the 'arms' of the ordered Ga-oxalate entity and only one conformation is seen at all temperatures. The data were good enough to allow full anisotropic refinement of all atoms with the exception of the disordered terminal ethylene groups and all hydrogen atoms of the structure. These latter atoms were modelled as 'riding' on the atoms to which they are bonded. Multi-scan absorption corrections were applied to the data, using SADABS⁹ and a weighting scheme was only applied to the final refinement cycles. The data were refined to give the final values shown in the crystallographic data table: Table 3.1.2.

Following the satisfactory solution and refinement of this structure and after another crystal was tested and was found to give better counting statistics, a full variable temperature (VT) analysis was initiated. One of the first parameters to be studied was the unit cell volume, as this may give indications to the global changes in a structure at particular temperatures. As the properties for this material, in particular the conductivity, were measured over a wide temperature range, it was desired to measure X-ray diffraction data over as full a temperature range as was possible, with current laboratory equipment.

Formula	Ga(C ₂ O ₄) ₃ · (C ₁₀ H ₈ S ₈) ₂ · C ₆ H ₅ NO ₂ ·H ₃ O	R _{INT}	0.1312
Space Group	C2/c	R ₁ (F _o >4σF _o)	0.0636
a (Å)	10.2915(4)	R ₁ (all)	0.1488
b (Å)	20.0355(7)	R _w	0.1637
c (Å)	35.3344(12)	GoF	0.966
β°	92.510(1)	Max residual (eÅ ⁻³)	0.52
Volume (Å ³)	7278.8(5)	Min residual (eÅ ⁻³)	-1.07
Z	4	Number of reflections	40990/ 8361/ 4258
Crystal size (mm ³)	0.15 x 0.1 x 0.07	observed/unique/ (F _o >4σF _o)	
Ratio max/min transmission	0.9155	Number of parameters	458
μ mm ⁻¹	1.36		

Table 3.1.2: Crystallographic data for β''-(ET)₄[(H₃O)Ga(C₂O₄)₃]PhNO₂ at 290 K.

There are technological restrictions on the temperature range that can be achieved using X-ray diffraction in the laboratory. In the Durham laboratory the lowest temperature that could be achieved, at the time of writing, was approximately 10 K and that required the use of highly specialised equipment. The 'standard' three circle CCD diffractometers are equipped with open flow cooling devices, which afford temperatures as low as 25 K, depending on the gas employed for cooling. Therefore initially the unit cells were determined via short matrix data collections taken at intervals of 5 K. Temperatures from 25 to 170 K were collected on the SMART 1K diffractometer and from 150 to 200 K on the SMART 6K diffractometer. A further data collection was later recorded at 12 K on the Fddd diffractometer¹⁰ and using the data collection and the interpretation software MAD¹¹. This data collection at the very low temperature of 12 K was achieved using a closed cycle refrigeration unit (Displex¹²).

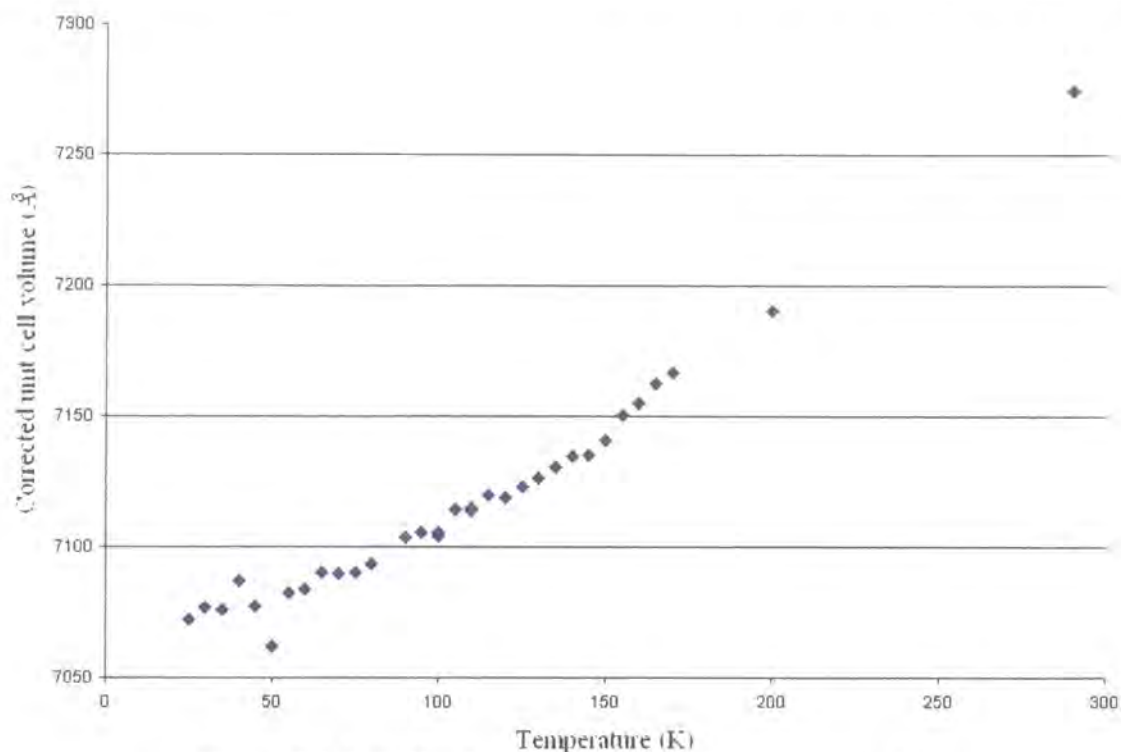


Figure 3.1.6: Cell volume variation with temperature for

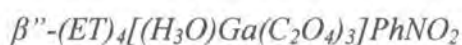


Figure 3.1.6 shows the results of the cell volume determinations from the matrix data collections. Comparison of the graph above (Figure 3.1.6) with that of resistivity vs. temperature, gives an indication that there are only very small physical changes occurring in the crystal relating to the changes in physical properties measured. If sufficient sample had been available, this variable temperature experiment would have been repeated on a high resolution powder diffractometer with a smaller separation of data points and higher accuracy of derived unit cell parameters. These measurements provided additional weight for further investigation and led to the collection of full datasets at: 200, 150 K on the SMART 6K diffractometer, 100 and 30 K on the SMART 1K diffractometer, and later 12 K on the Fddd diffractometer. It was hoped that this would allow any structural change to be noted and analysed fully, given that there were no abrupt changes in the unit cell volume, it was thought to be unlikely that the system changed drastically from that at room temperature. The graph above shows the unit cell volume after a correction has been applied to all the data collected on the SMART 1K. This correction was necessary as the data from these experiments had shown that differences in unit cell volumes of approximately 0.5 – 1 % were seen between

diffraction patterns measured on different Bruker diffractometers at the same recorded temperature, uncorrected data shown in Figure 3.1.7.

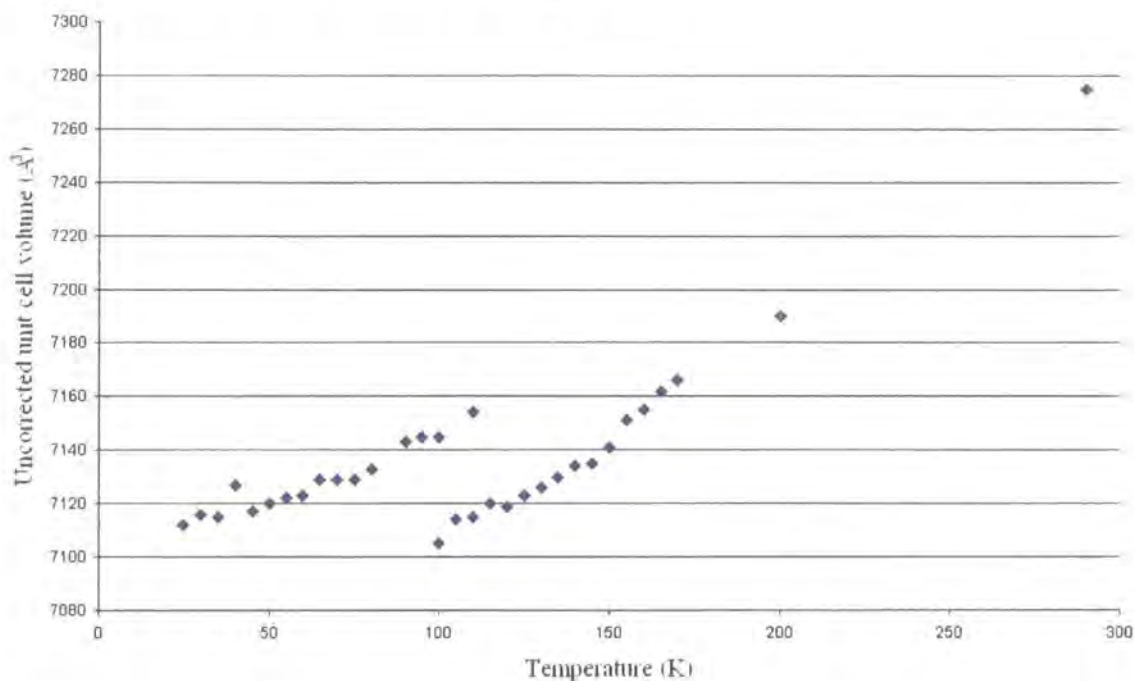


Figure 3.1.7: Graph showing the uncorrected unit cell volumes, and the disconnection at the same temperature of data collected on different SMART diffractometers.

This correction has been applied by the scaling of the unit cell axes and the β angle using the ratio of those values collected on different machines at the same temperature. Graphs of these corrected values plus those measurements taken on the SMART 6K diffractometer were then plotted and a 2 parameter polynomial expression fitted to the data. These expressions were used to regain the ‘correct’ unit cells for all data refinements to allow more rigorous comparison of bond lengths. The plots and correction expressions can be found on the CD inside the back cover of this thesis, Appendix D. It is the large size of the unit cells of β'' -(ET)₄[(H₃O)Ga(C₂O₄)₃]PhNO₂ and similar materials that has allowed the 0.5 – 1% variation to become apparent, together with the requirement for the study to record diffraction data over a large range of temperatures. Although many experiments were conducted to find the sources of these errors, they still remain unknown. One remaining possible cause of the error on the SMART 1K is that the phosphor of the detector is not exactly perpendicular to the 2-*theta* arm. This could have occurred at the time the phosphor was replaced some years ago, although the new alignment was checked by the Bruker engineers at the time.

The principal atomic sites for any expected deviation from the room temperature model were the disordered terminal ethylene groups of the ET molecules and any consequent interaction with the nitrobenzene guest molecule. The two moieties are shown in Figure 3.1.8. The nitrobenzene molecules are situated in the hexagonal cavities in the Ga-oxalate water network as shown earlier in Figure 3.1.3, the honeycomb of the Ga-oxalate water network has been removed for clarity.

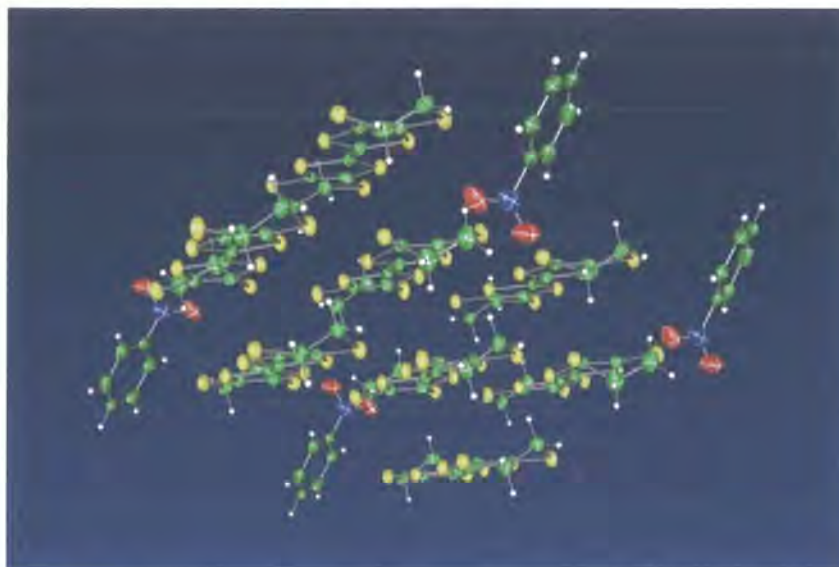


Figure 3.1.8: Orientation of the nitrobenzene to the ET molecules at 100 K.

As can be seen from Figure 3.1.8, the disorder in the ethylene groups has been resolved and is no longer observed at 100 K. Only a minor disorder was present at 150 K and below that temperature none was seen. This observed low temperature ordering of the terminal ethylene groups suggests that the disorder at higher temperatures was a result of thermal barriers to ‘flipping’ being overcome, the barrier depends highly on the local environment allowing the two conformations to exist (see later discussion).

The angle that the plane of the phenyl ring of the nitrobenzene makes with the plane of the Ga atoms was found to be 31° at room temperature and does not change by more than 0.4° on cooling from room temperature to 30 K; indeed the angle is still only 32.1° at 12 K. However the torsion angle of the nitro group to the phenyl ring changes more significantly with temperature. At room temperature the nitro group is twisted only 0.9° out of the plane of the Ga atoms making the torsion angle about the N – C bond $32.00(29)^\circ$ and at 12 K this torsion angle has increased to $39.99(61)^\circ$. The energetically expected torsion angle is 0° as the nitro group is expected to be in the plane of the

phenyl ring¹⁵, hence the distortion from this lowest energy conformation must be due to quite specific intermolecular interaction. The change in torsion angle appears to be near linear with temperature shown in Figure 3.1.9, however the angle calculated from the 12 K data appears to break the trend, although as mentioned this data is less well resolved.

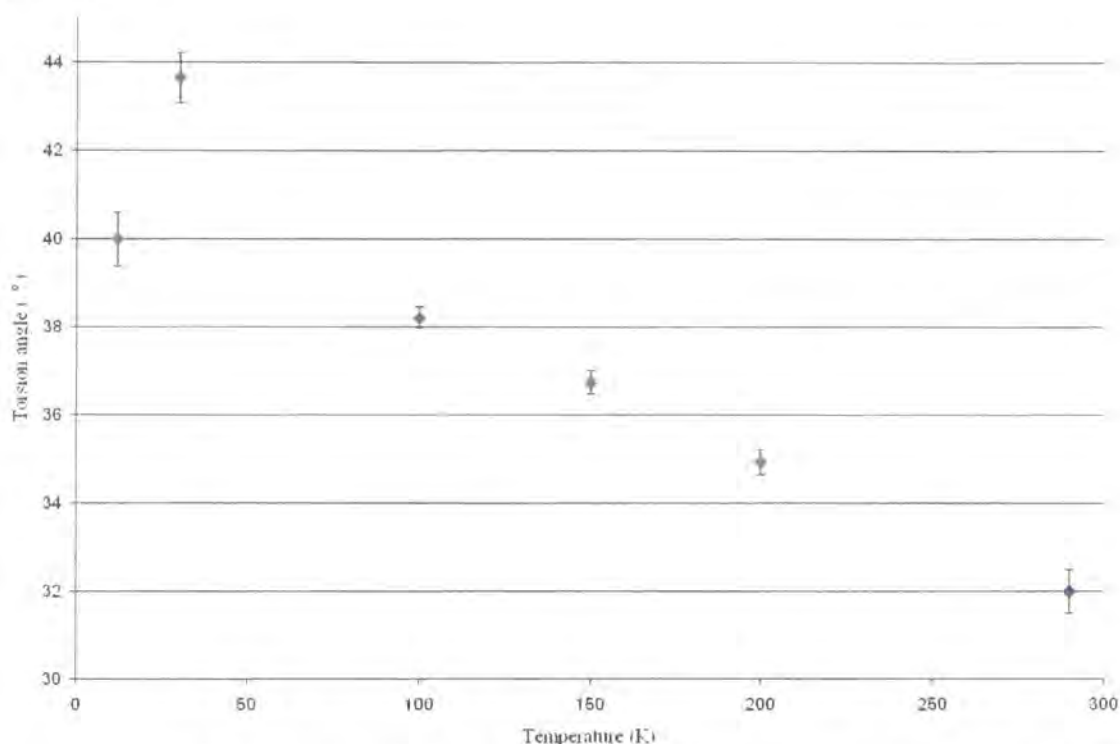


Figure 3.1.9: Variation of torsion angle in the nitro benzene molecule, in β'' - $(ET)_4[(H_3O)Ga(C_2O_4)_3]PhNO_2$, with temperature.

This change in torsion angle of the nitro group is suspected to contribute to the difference in conductivity properties of this material, if the inter- and intra-molecular orbital interactions are altered considerably due to this motion. The principal intermolecular interaction of the nitro group is with the terminal ethylene group of the disordered ET molecule (O7 of the nitro group and H1B of the ethylene group), this is the molecule that has a disorder in its terminal groups at higher temperatures. Although this interaction distance is relatively long (approximately 2.4 Å) it could be the driving force behind the rotation of the nitro group from the plane of the phenyl ring. It would be very interesting to calculate the exact electron density of these structures and other structural parameters above and below the superconducting transition temperature i.e. to conduct a charge density experiment. This would enable the bond path diagrams to be calculated which would clearly show these types of interaction and clarify their

importance. This would only be possible if crystals of suitable quality were available and if facilities were to accessible to conduct X-ray diffraction experiments throughout the whole temperature range (2 – 300 K). Another possible cause of the increase in torsion angle is due to the contraction of the cavity in which the nitrobenzene resides, the increase in torsion angle maintains the separation of the oxygen atoms of the nitro group and the oxalate entities. The rotation in this case would be forced through the electrostatic repulsion of the oxygen atoms.

Another interaction that does change with the temperature and one that is more likely to result in the electrical conduction properties is that of the S ... S contacts between ET molecules. The principal S ... S contacts are listed, with the interaction distances in Table 3.1.3 below.

	290 K	200 K	150 K	100 K	30 K	12 K
S10 – S1 Å	3.5939(24)	3.5472(16)	3.5188(15)	3.4917(14)	3.4749(22)	3.4740(30)
S10 – S3 Å	3.5079(22)	3.4620(15)	3.4375(14)	3.4142(13)	3.3936(23)	3.3885(31)
S14 – S7 Å	3.3742(22)	3.3473(15)	3.3375(14)	3.3302(13)	3.3156(23)	3.3144(32)
S16 – S7 Å	3.3198(23)	3.3116(15)	3.3046(14)	3.2990(13)	3.2846(21)	3.2881(30)
S6 – S2' Å	3.5033(22)	3.4729(15)	3.4613(14)	3.4523(13)	3.4400(23)	3.4305(32)
S8 – S2' Å	3.4151(22)	3.3965(14)	3.3860(14)	3.3779(13)	3.3659(21)	3.3584(30)
S2 – S11* Å	3.6531(22)	3.6180(15)	3.6006(15)	3.5874(14)	3.5745(22)	3.5747(34)

*generated by symmetry operation (2-y, 1-y, 1-z), *Interlayer contact identified using Mercury⁶.

Table 3.1.3: S – S interaction lengths calculated at the temperatures for which full structure solutions were available.

There are some definite trends to be seen when these interaction distances are displayed graphically, Figure 3.1.10. Most notably there is a difference in the rate of decrease of interaction lengths for the different contacts. It has been suggested previously that compounds containing ET molecules can form a conduction band through overlapping molecular orbitals, forming a 2-dimensional Fermi surface¹⁷.

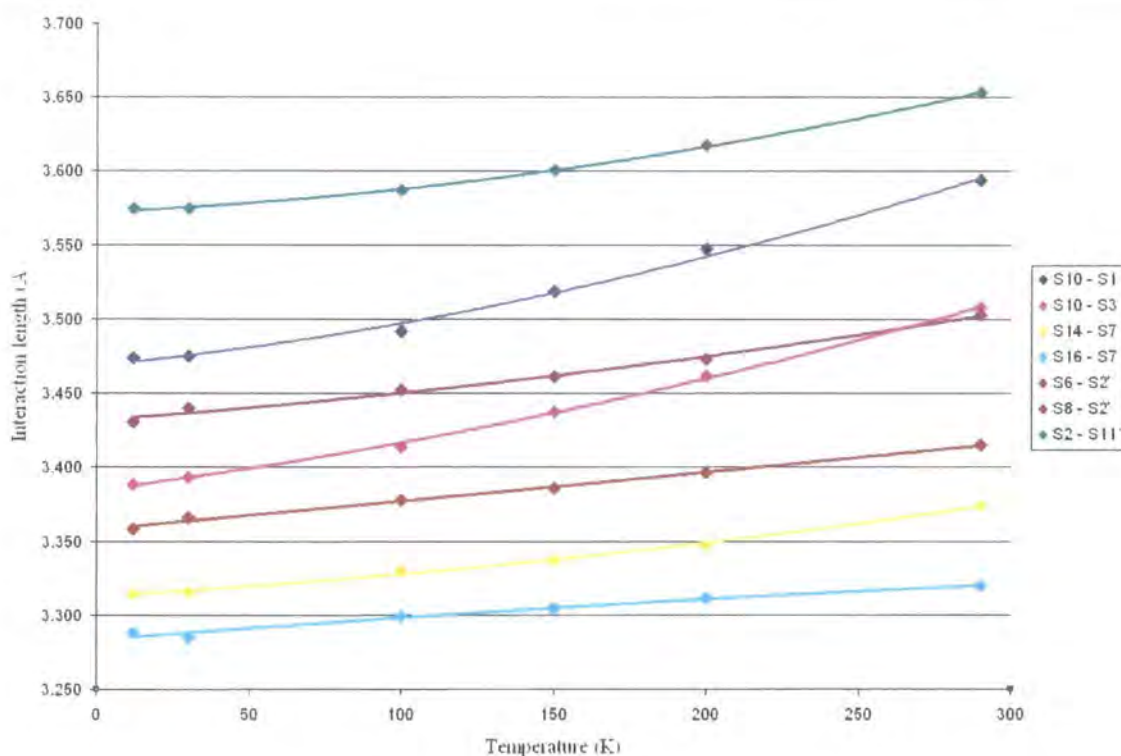


Figure 3.1.10: Graph showing the changes in the major S – S interactions in β'' -
 $(ET)_4[(H_3O)Ga(C_2O_4)_3]PhNO_2$.

One other molecular parameter that was analysed after a notable change had been observed, was the length central C = C double bond of the ET molecules. These bond lengths are shown in Table 3.1.4, and have very strange broad trends, the C5=C6 bond increases on cooling, and the C15=C16 bond shortens on cooling.

Temp. (K)	C5 = C6	C15 = C16
12	1.376(11)	1.353(12)
30	1.366(8)	1.368(8)
100	1.368(5)	1.355(5)
150	1.363(5)	1.357(5)
200	1.362(5)	1.361(5)
290	1.348(7)	1.359(7)

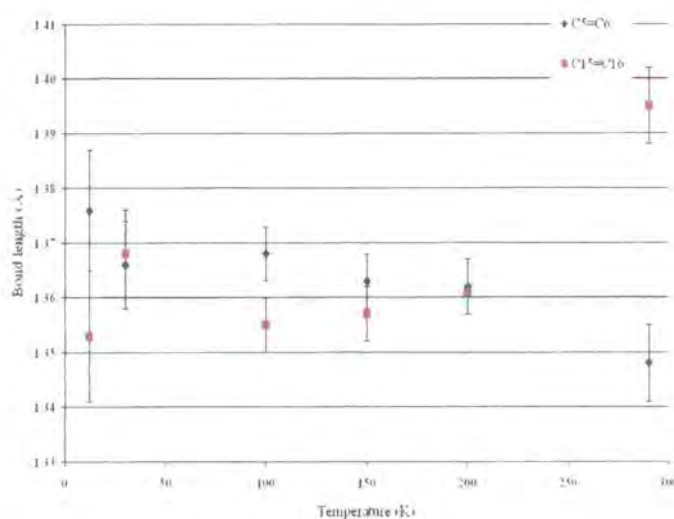


Table 3.1.4: C = C double bond lengths in the independent ET molecules, also shown graphically (right).

Although the changes in bond length are relatively small, even in comparison to the errors, they show a definite trend, however the values of the bond length variations are within 3σ and therefore no firm conclusions can be drawn. The changing bond lengths suggest a movement of charge in the structure upon cooling, which has major implications for the conduction band and the electrical properties of the molecule. It is reasonable to assume that the charge transfer to each of the ET molecules is not equal, and that each molecule supports a different charge. These results on the C = C bond lengths confirm this, but they also show that the charge localisation changes on cooling the system.

The charges carried by the ET molecules according to Guionneau *et al.*¹⁸ (Equation 2.1) method are shown in Table 3.1.5. These calculated charges show that there is indeed charge localisation at lower temperatures, reaching a final ratio of 0.70(12) : 0.41(12) at 12 K, if this is related to the graph of electrical resistance, this could explain the semiconductor properties. The conductivity of these materials is highly sensitive to the ET molecules a partial charges¹⁸.

Temp. (K)	Central bond	a (Å)	b (Å)	c (Å)	d (Å)	delta δ	Q
12	C5-C6	1.376(11)	1.734(5)	1.751(5)	1.352(9)	0.756(16)	0.70(12)
	C15-C16	1.353(12)	1.746(5)	1.753(5)	1.351(8)	0.795(16)	0.41(12)
30	C5-C6	1.366(8)	1.740(3)	1.755(3)	1.352(6)	0.777(11)	0.55(8)
	C15-C16	1.368(8)	1.744(3)	1.756(3)	1.347(6)	0.784(11)	0.49(8)
100	C5-C6	1.368(5)	1.738(2)	1.745(2)	1.353(4)	0.762(7)	0.66(5)
	C15-C16	1.355(5)	1.745(2)	1.754(2)	1.344(4)	0.800(7)	0.38(5)
150	C5-C6	1.363(5)	1.739(2)	1.753(2)	1.347(4)	0.782(7)	0.51(5)
	C15-C16	1.357(5)	1.743(2)	1.752(2)	1.344(4)	0.795(7)	0.42(5)
200	C5-C6	1.362(5)	1.738(2)	1.752(2)	1.338(4)	0.790(7)	0.45(5)
	C15-C16	1.361(5)	1.742(2)	1.754(2)	1.338(4)	0.796(7)	0.40(5)
290	C5-C6	1.348(7)	1.740(3)	1.739(3)	1.356(6)	0.776(10)	0.56(7)
	C15-C16	1.359(7)	1.739(3)	1.744(3)	1.360(6)	0.765(10)	0.64(7)

Table 3.1.5: Calculated charges (Q) supported by ET molecules calculated using Equation 2.1.

The structural solutions below 100 K show the presence of a few weak systematic absence violations, suggesting the symmetry is being broken by some new / or changed aspect of the structure. All attempts to solve and refine in a lower symmetry were unsuccessful due to the high correlations of many parameters in the refinement. The data from all temperatures presented, have been solved and refined in the space group $C2/c$. The systematic absence violations seen (at 30 K and 12 K) were very weak and very few in number, 51 systematic absence violations from 10061 reflections in the worst case (12 K), and any move away from $C2/c$ symmetry must be very slight. The data collected on the Fddd diffractometer were far less redundant than those collected on the SMART diffractometers due to the differences in data collection modes between area detectors and single point detectors. There was an additional problem with the data collection on the Fddd diffractometer in that the temperature began to drift after a few days into the experiment. The data collection was eventually stopped when the temperature reached 18 K, as worries about any subsequent changes in the structure outweighed the need for more data. The number of data was fewer than required for a stable anisotropic refinement and therefore a reduction in the number of parameters was required. This was achieved through the use of constraints. It was chosen to constrain the U_{ij} matrices of paired atoms, in the same ET molecules, in similar environments to be equal. This allowed full refinement and resulted in acceptable refinement statistics. Since the derived structural parameters fitted with the general trends of parameters seen at other temperature the refined values can be accepted. The refinement of the 30 K data collected on the SMART 1K diffractometer gave a best fit when another minor disorder was included. The phenyl ring of the nitro benzene was modelled as being slightly off the crystallographic 2-fold axis, which does run through the centre of the molecule at all other temperatures. This required modelling 50% occupied atoms either side of the 2-fold axis and constraints for the atoms to form a flat hexagonal ring. These 6 half occupied atomic sites were situated very close to each other since the deviation away from the crystallographic axis was small (0.17 – 0.28 Å). The restriction was achieved using the EQIV and FREE commands in XL to generate the additional 6 symmetry equivalent C atoms in the refinement input file and then force them not to be bound to each other.

It is well known that cooling crystal samples normally provides the experimentalist with generally higher quality data and a reduction in thermal motion of the atoms in the crystal.

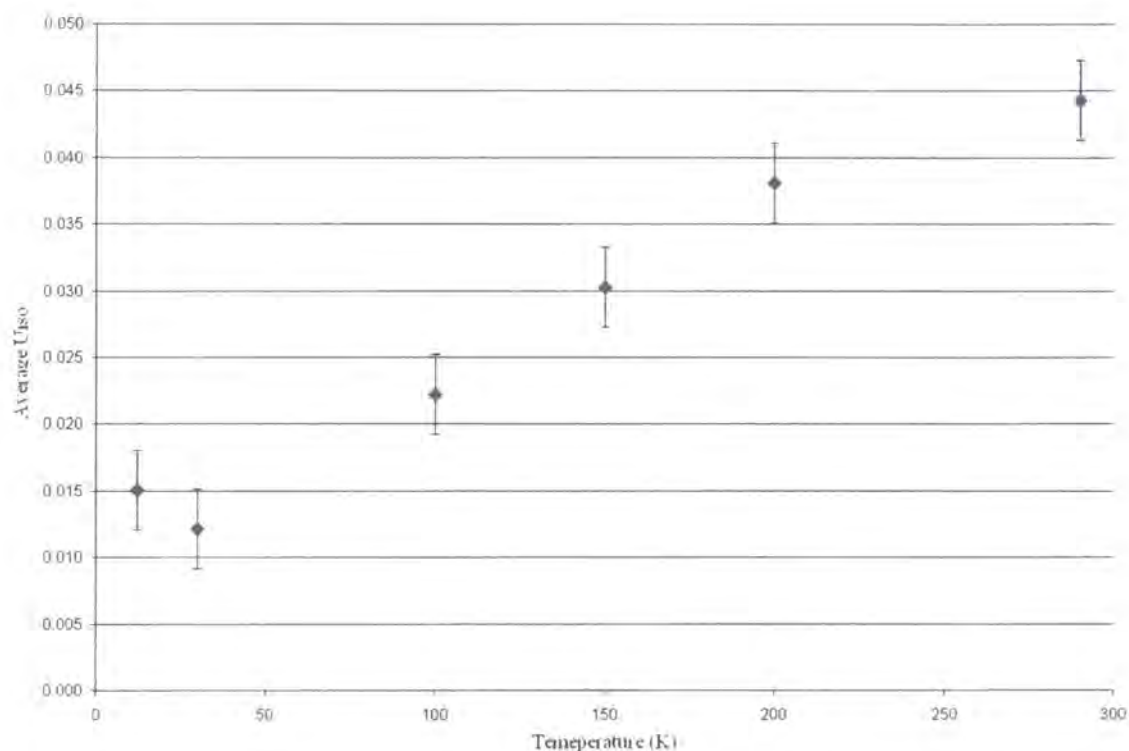


Figure 3.1.11: Average spherical thermal parameters at various temperatures for β'' - $(ET)_4[(H_3O)Ga(C_2O_4)_3]PhNO_2$.

Since there is an abundance of data on β'' - $(ET)_4[(H_3O)Ga(C_2O_4)_3]PhNO_2$ it would seem pertinent to analyse this trend, therefore average values of the U_{iso} value were calculated for all atoms in the asymmetric unit, for which a U_{ij} matrix was refined, for each data collection temperature. These results are plotted in the graph in Figure 3.1.11. The expected decrease in U_{iso} value is observed with decreasing temperature. The upturn at 12 K is probably not an artefact it is more likely a resultant feature of the heavy constraints that were applied to that model to stabilise the refinement.

Selected crystallographic data for structural studies below 290 K are shown in Table 3.1.6 below and full data can be found in Appendix D.

Formula	200 K	150 K	100 K	30 K	12 K
Space Group	C2/c	C2/c	C2/c	C2/c	C2/c
a (Å)	10.2726(4)	10.2637(3)	10.2557(3)	10.246(2)	10.244(2)
b (Å)	19.9241(7)	19.8777(7)	19.8421(6)	19.811(4)	19.806(4)
c (Å)	35.1522(12)	35.0652(12)	34.9833(11)	34.898(7)	34.878(7)
β°	92.9250(10)	93.1200(10)	93.2880(10)	93.48(3)	93.52(3)
Volume (Å ³)	7185.3(4)	7143.4(4)	7107.2(4)	7071(2)	7063(2)
Z	4	4	4	4	4
μ mm ⁻¹	1.378	1.386	1.393	1.400	1.402
R _{INT}	0.0981	0.0880	0.0805	0.1152	0.0638
R ₁ (F _o >4 σ F _o)	0.0434	0.0430	0.0414	0.0690	0.1068
R ₁ (all)	0.1022	0.0933	0.0838	0.0919	0.1393
R _w	0.0930	0.0941	0.0917	0.1443	0.2653
GoF	0.810	0.881	0.905	1.115	1.036
Max residual (eÅ ⁻³)	0.662	0.763	0.796	0.643	3.494*
Min residual (eÅ ⁻³)	-0.513	-0.532	-0.528	-0.819	-3.470*
Number of reflections	71548 /	35677 /	35497 /	20311 /	10061 /
observed / unique / (F _o >4 σ F _o)	7867 / 4050	7825 / 4399	7781 / 4690	7179 / 5390	8097 / 5896
Number of parameters	452	452	452	443	298

*these peaks are within 0.79 Å of the Ga atom and are either due to serious termination errors or evidence of the breaking symmetry

Table 3.1.6: Selected crystallographic data over the range of temperatures studied.

3.2 The study of the structure of:

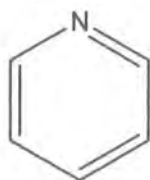


Figure 3.2.1: Pyridine is the guest molecule in $\beta''\text{ET}_4[(\text{H}_3\text{O})\text{Ga}(\text{C}_2\text{O}_4)_3]\text{C}_5\text{H}_5\text{N}$

The compound, $\beta''\text{ET}_4[(\text{H}_3\text{O})\text{Ga}(\text{C}_2\text{O}_4)_3]\text{C}_5\text{H}_5\text{N}$, was found to be iso-structural at room temperature (290 K) with the nitrobenzene compound described in section 3.1. The guest molecule is smaller than in the previous study while the cavity formed by the Ga-oxalate layer is still the same size, and therefore it came as no surprise that when the pyridine molecule was located, it was rotationally disordered. With no functional group attached to the C_5N ring there are no stabilising intermolecular interactions to fix the orientation of the pyridine molecule, leaving the molecule free to 'rotate'.

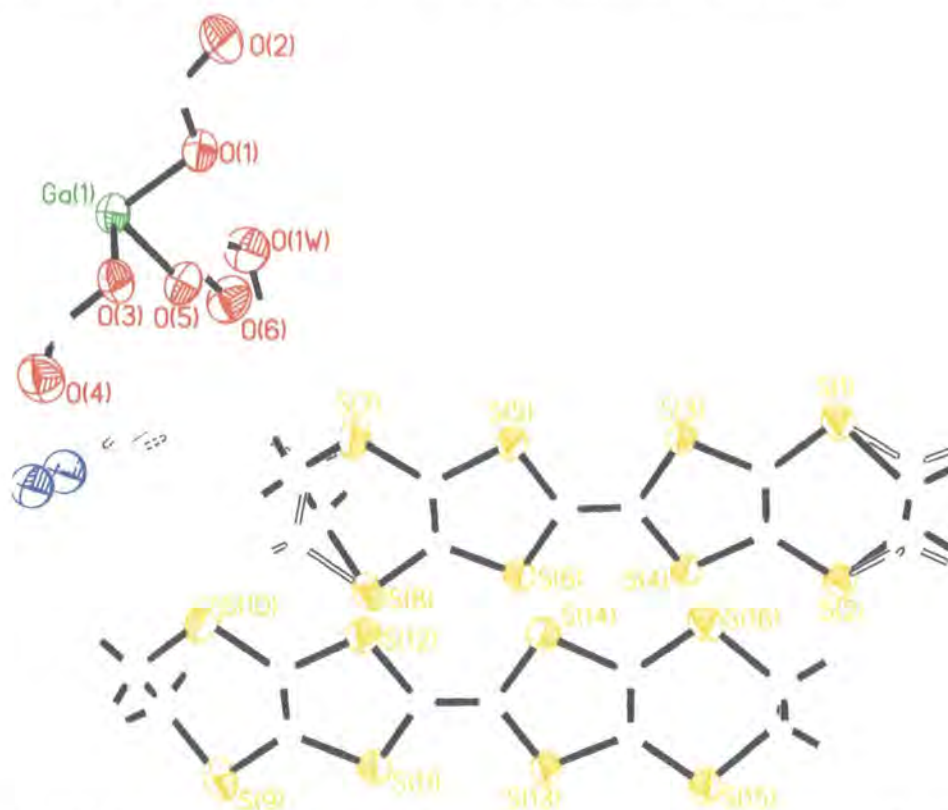


Figure 3.2.2: Asymmetric unit of pyridine guest complex, Ga: dark green, S-yellow, O-red, N-blue, C-grey, H-green, pyridine not labelled for clarity.

The 290 K structure, resolved from data collected on a SMART 1K diffractometer, resulted in the familiar disorder in the terminal ethylene groups of one of the ET molecules, along with severe rotational disorder in the pyridine guest molecule. These disorders were modelled in the refinement resulting in the crystallographic parameters shown in Table 3.2.1.

Formula	$\text{Ga}(\text{C}_2\text{O}_4)_3 \cdot (\text{C}_{10}\text{H}_8\text{S}_8)_2 \cdot \text{C}_6\text{H}_5\text{N} \cdot \text{H}_3\text{O}$
Crystal size (mm^3)	0.15 x 0.08 x 0.07
Space Group	C2/c
a (\AA)	10.3605 (9)
b (\AA)	19.9645 (17)
c (\AA)	35.4283 (31)
β°	92.760(2)
Volume (\AA^3)	7319.6(11)
Z	4
Ratio max/min transmission	0.8760
$\mu \text{ mm}^{-1}$	1.35
R_{INT}	0.0793
$R_1 (F_o > 4\sigma F_o)$	0.0498
R_1 (all)	0.1184
R_w	0.1360
GoF	0.841
Max residual ($\text{e}\text{\AA}^{-3}$)	0.79
Min residual ($\text{e}\text{\AA}^{-3}$)	-1.11
Number of reflections observed/unique/($F_o > 4\sigma F_o$)	35352 / 7895/ 3561
Number of parameters	413

Table 3.2.1: Crystallographic data for $\beta''\text{ET}_4[(\text{H}_3\text{O})\text{Ga}(\text{C}_2\text{O}_4)_3]\text{C}_5\text{H}_5\text{N}$ at 290 K.

The angle that the mean plane of the pyridine molecule makes to the plane of the Ga atoms was found to be 35.9° , slightly higher than that found for the nitrobenzene at the

same temperature, there is no a priori reason for this and it could be a result of the disorder.

Low temperature data were collected on the same crystal as it had yielded good refinement statistics once the disorder had been modelled. The crystal was cooled to 30 K on a SMART 1K diffractometer using a Helix cryo-cooler, since a previous data collection had been performed on this crystal at 120 K^{1,2}. The data once again looked good, with sharp reflection profiles and good integration statistics. The 30 K structure was originally solved in space group C2/c, the same space group as the 290 K structure, although some systematic absence violations were noted, albeit with relatively low intensities. The 30 K structure was initially solved to be iso-structural with the room temperature data, however refinement proved this to be incorrect with several parameters becoming increasingly unstable. The listing file (.lst) from refinement program (XL) showed that the systematic absence violations were consistent with the loss of the c-glide (*hkl* : *even zero odd* respectively), and it was decided these reflections could not be ignored. The data were then passed through XPREP to provide the correct initial raw data files required for a C2 system. The structure was resolved, providing all the basic molecular fragments, and the refinement was recommenced.

Correlations in the structure immediately became a problem, with changes in one half of the structure being matched by near equal and opposite moves in the other half. This near linear correlation between certain parameters was not surprising as the structure is obviously very close to being C2/c, this problem required a new refinement technique to be applied. A feature found in SHELXTL to allow proteins and other large structures to be refined is a BLOC refinement. This refinement effectively splits the model into smaller moieties refining them independently, thus negating the destabilisation of the least squares (L.S.) refinement by the correlations. BLOC allows the refinement of each 'half' of the structure separately and hence removes the major problems of correlation. Non correlated parameters i.e. FVAR were refined in all cycles of L.S. procedure. With this problem eliminated, refinement progressed until it became apparent that the Ga sites were further split away from their current positions. The Ga atoms lie on a 2 fold rotation axis in the structure whether solved in space group (S.G.) C2/c or C2. The shift away from this axial position was manifest in large peaks and holes appearing in the difference Fourier map on either side of the two fold axis, equivalent to those seen in

the 12 K structure of β'' -(ET)₄[(H₃O)Ga(C₂O₄)₃]PhNO₂. This small shift of the Ga atoms in the structure posed the question; was this feature a disorder in the crystal or was it a true move away from the supposed C centred symmetry, making the system really primitive? The latter was considered first. If the symmetry had indeed dropped to primitive, then the model would become very large, well in excess of 1000 atoms, giving rise to a computational problem as well as a refinement one. A system of that size requires a very large number of observed reflections to give an acceptable data : parameter ratio. These data were not available, since the crystal quality was not high enough to provide sufficient high angle reflections, and no other crystals were available of better quality.

A structure solution was attempted in space group P-1 and this appeared to be successful initially but full refinement was impossible due to the very low data parameter ratio, along with massive inter-parameter correlations. The refinement cycle time for an isotropic model was also very high, even with the most powerful computer in the laboratory, for which refinement cycles required approximately 30 minutes each. Until further data could be collected, from crystals of higher quality, this approach was abandoned and concentrations returned once again to the C2 model, adding disorder that would mirror some of the consequences of lowering the symmetry. A 'simple' twin refinement was also attempted in XL using the TWIN and BASF commands. The BASF factor refined to ~0.64 suggesting that the crystal may be twinned. The twinning type could not be determined from the limited data. The final crystallographic parameters for this refinement, which ceased at the isotropic level, are given in Table 3.2.2

Formula	Ga(C ₂ O ₄) ₃ · (C ₁₀ H ₈ S ₈) ₂ ·C ₆ H ₅ N·H ₃ O
Space Group	C2
a (Å)	10.3017 (4)
b (Å)	19.7026 (9)
c (Å)	34.8506 (15)
β°	93.802(2)
Volume (Å ³)	7058.1(5)
Z	4
μ mm ⁻¹	1.40
R _{INT}	0.0632
R ₁ (F _o >4σF _o)	0.1127
R ₁ (all)	0.1462
R _w	0.2967
GoF	1.690
Max residual (eÅ ⁻³)	1.80
Min residual (eÅ ⁻³)	-4.17
Number of reflections observed/unique/(F _o >4σF _o)	32590 / 9735 / 7292
Number of parameters	440

Table 3.2.2: Crystallographic data for β''ET₄[(H₃O)Ga(C₂O₄)₃]C₅H₅N at 30 K.

The refinement statistics are not satisfactory, however they derive from a highly disordered model for which anisotropic temperature factors could not be refined. This is a considerable drawback given the number of atoms in the unit cell. In total, the refinement had to be conducted in 24 separate parts, 12 allowing the movement of each molecule individually, and then 12 to allow each molecules' U_{iso} to refine. There are still many unresolved problems with this structure, and further data collection from new crystals of higher quality will be required in order to describe the structure more accurately. Despite these difficulties, the overall molecular connectivity has been confirmed and similarities and differences with the [PhNO₂] structure can be discussed at low resolution. Full crystallographic data tables can be found in Appendix D.

3.3 The study of the structure of: $\beta''(ET)_4[(NH_4)M(C_2O_4)_3]218\text{-crown-6-ether}\cdot(H_3O)_2\cdot(H_2O)_5$; $M = Ga^{19}$ or Cr

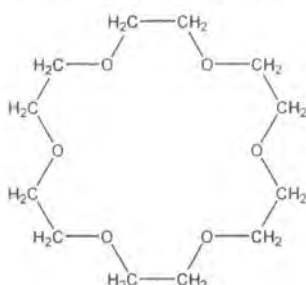


Figure 3.3.1: 18-crown-6-ether, the guest molecule in $\beta''(ET)_4[(NH_4)M(C_2O_4)_3]218\text{-crown-6-ether}\cdot(H_3O)_2\cdot(H_2O)_5$.

The guest molecule for this compound is clearly much larger than any presented thus far, although this seems a fairly minor change it will be shown how dramatic an effect this has on the crystal structure. The ET charge transfer salts studied so far have had packing arrangement that could be described as ABAB, in that the ET molecules form layers that are separated by layers of Ga-oxalate grids. The same description of this structure would be ABCBABC²⁰, however the Ga-oxalate layers alternate chirality, as in the other salts, so a more accurate description is ABCDABCDA shown in Figure 3.3.2 below.

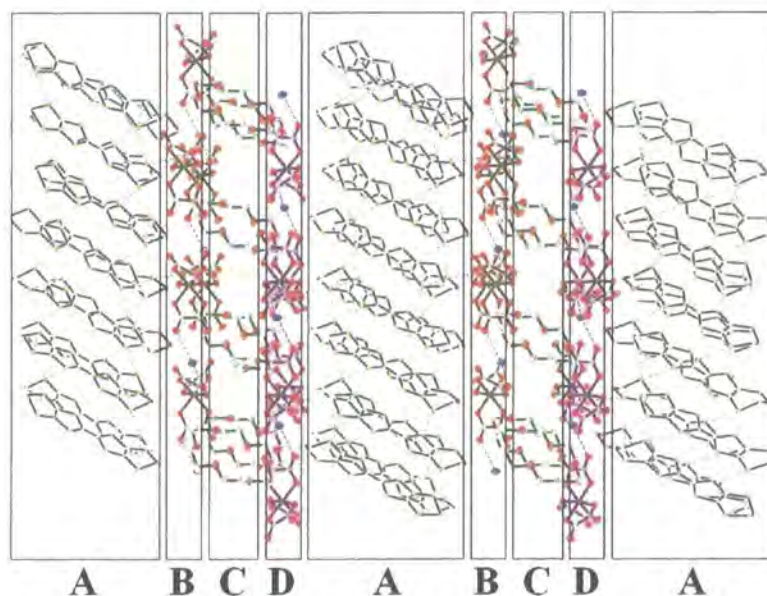


Figure 3.3.2: Packing diagram showing the layering in $\beta''(ET)_4[(NH_4)M(C_2O_4)_3]218\text{-crown-6-ether}\cdot(H_3O)_2\cdot(H_2O)_5$ at 30 K, the water molecules and hydrogen atoms have been removed for clarity, view is perpendicular to the a - c plane.

Data were recorded at 120 K for both the Cr and Ga salts, which were found to be isostructural. The crystal size for the Cr sample (0.18 x 0.08 x 0.01 mm³) was far smaller than the Ga salt (0.3 x 0.25 x 0.02 mm³), and required a much higher exposure time to generate sufficiently high counting statistics for an accurate structure determination. The exposure time for the Cr salt was 90s/frame, and only 10s/frame for the Ga salt. With this consideration, only the Ga salt was cooled to 30 K and data collected to enable resolution of the water molecules and their protons. Data were collected at 30 K on a SMART 1K diffractometer and at 120 K on a SMART 6K diffractometer. Table 3.3.1 contains the final crystallographic parameters for all data collections.

	Ga 120 K	Ga 30 K	Cr 120 K
Space Group	P-1	P-1	P-1
a (Å)	10.2094(2)	10.2070(3)	10.2154(3)
b (Å)	11.1931(2)	11.2012(3)	11.2334(4)
c (Å)	24.2193(4)	24.2433(6)	24.1231(8)
α°	88.478(1)	88.417(1)	88.509(1)
β°	88.428(1)	88.502(1)	88.433(1)
γ°	63.704(1)	63.447(1)	63.683(1)
Volume (Å ³)	2480.00(8)	2478.15(12)	2480.08(14)
Z	2	2	2
μ mm ⁻¹	1.300	1.300	0.978
R _{INT}	0.0751	0.0262	0.0320
R ₁ (F _o >4 σ F _o)	0.0484	0.0357	0.0487
R ₁ (all)	0.0938	0.0466	0.0997
R _w	0.1171	0.0794	0.1073
GoF	0.903	1.021	0.998
Max residual (eÅ ⁻³)	1.047	0.854	1.509
Min residual (eÅ ⁻³)	-1.110	-0.913	-0.942
Number of reflections observed/unique/(F _o >4 σ F _o)	41319 / 19906 / 12003	23758 / 10910 / 9167	21950 / 14308 / 8899
Number of parameters	636	598	643

Table 3.3.1: Selected crystallographic parameters for $\beta''(ET)_4[(NH_4)M(C_2O_4)_3]_2$ 18-crown-6-ether·(H₃O)₂·(H₂O)₅.

The water molecules not shown in Figure 3.3.2 are located in the channels through the crystal structure afforded by the cavity of the 18-crown-6-ether, this can be clearly seen in Figure 3.3.3. The proton positions for the Ga salt at 120 K were taken from the 30K data, and were not located in the 120 K data from the Cr salt, as there was no supporting low temperature data available.

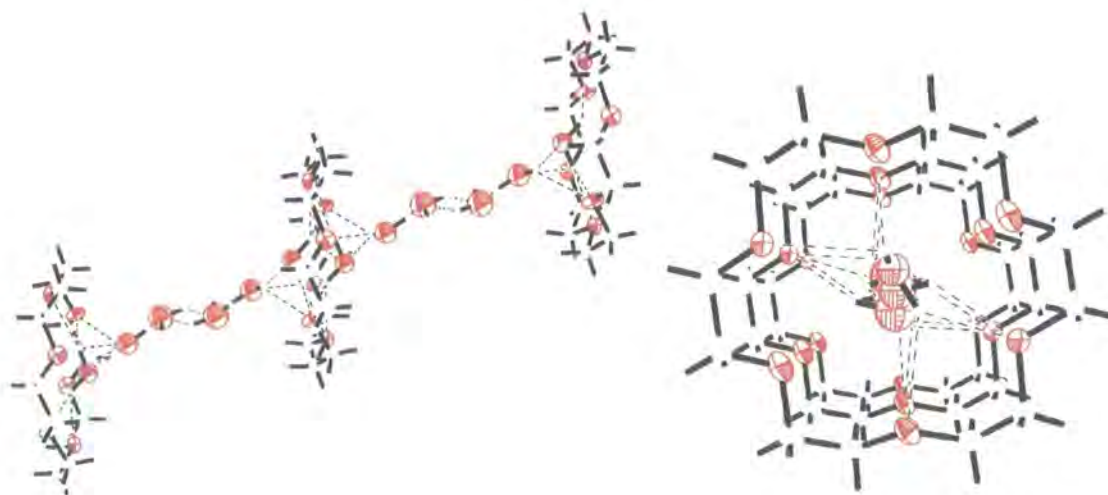


Figure 3.3.3: Crown ether channels containing water molecules at 30 K.

There are another two water molecules, located off the stack axis, which appear to interact with the Ga-oxalate layers. The inter-layer cavity formed by the M-oxalate layers (M= Ga or Cr) that encompasses the crown ether is different from that seen for all the other studies presented. This is due to the necessary expansion of the cavity to accommodate such a large guest molecule forming a structure with two M-oxalate layers for each layer of guest molecule. This altered cavity is shown in Figure 3.3.4.

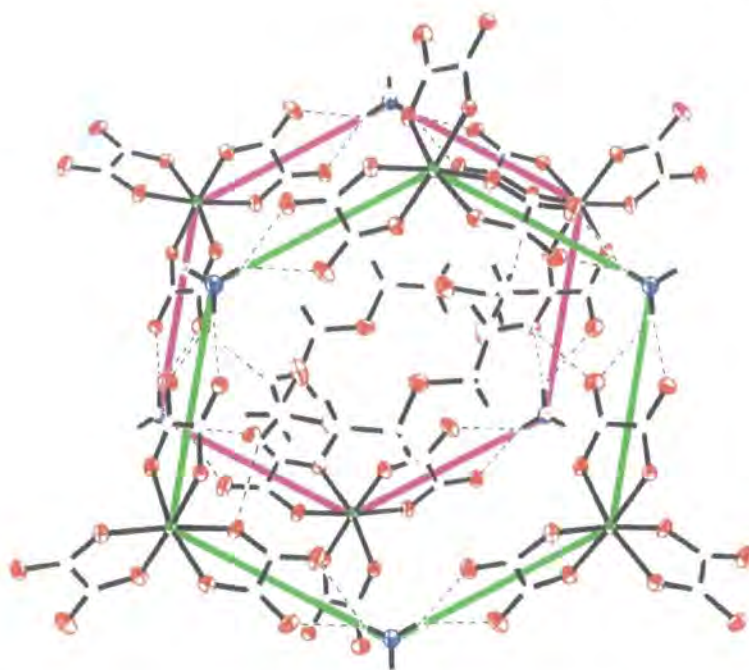


Figure 3.3.4: The crown ether cage formed from Ga-oxalate layers, above (green) and below (pink) the crown ether guest molecule.

The remaining cations required for electro-neutrality of the structure are located in the crown ether channels, as protonated water molecules. Though not all protons could be located from the X-ray diffraction data, sufficient numbers were observed to allow remaining hydrogen atoms to be placed in chemically sensible positions to complete the model. The presence of this chain of water molecules through the crystal structure is thought to facilitate one of this crystal's exceptional physical properties, that of being a proton conductor. Details of the conductivity properties can be found in reference 19. Figure 2.2.3 based on preliminary resistivity measurements, does not show clear evidence of any superconductivity as the temperature is decreased.

There are a number of short S – S contacts, shown in Figure 3.3.5 and Table 3.3.2. These contacts are thought to be those involved in forming the necessary Fermi surface for the electrical conductivity properties this crystal shows.

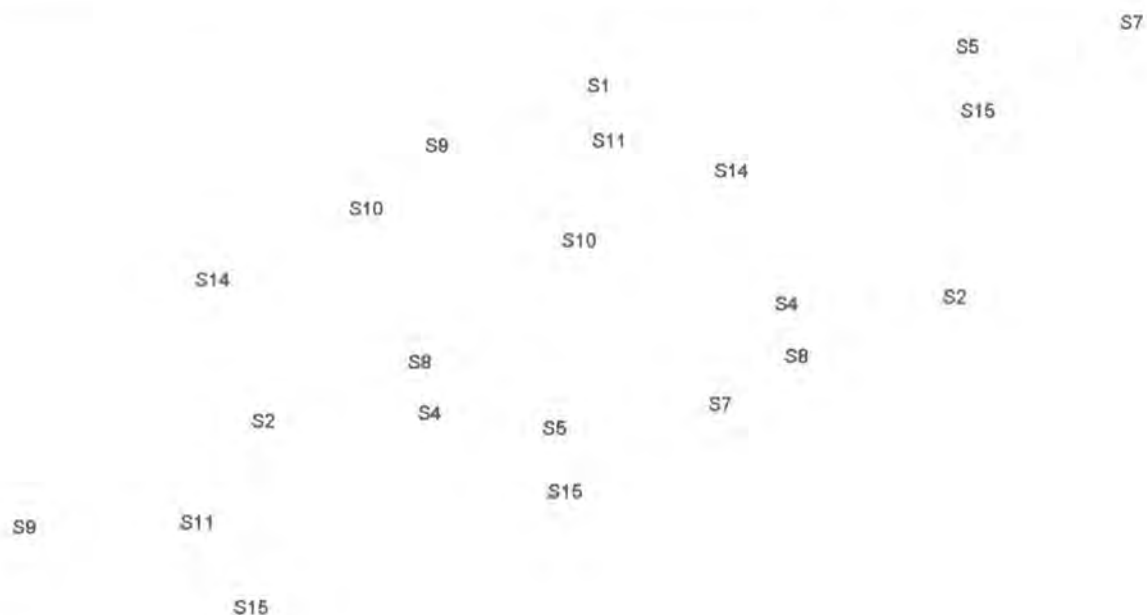


Figure 3.3.5: Short S – S contacts in $\beta''(ET)_4[(NH_4)M(C_2O_4)_3]_2 18\text{-crown-6-ether} \cdot (H_3O)_2 \cdot (H_2O)_{5.7}$ at 30 K

	Length (Å)		Length (Å)
S8 – S4 ¹	3.4417(8)	S15 – S7 ²	3.4848(8)
S8 – S2 ¹	3.3184(8)	S1 – S11 ³	3.3251(8)
S15 – S2 ¹	3.5798(8)	S1 – S9 ³	3.2828(8)
S15 – S5 ²	3.4982(8)	S10 – S14 ⁴	3.5824(8)

Table 3.3.2: Short S – S contacts in $\beta''(ET)_4[(NH_4)M(C_2O_4)_3]_2 18\text{-crown-6-ether} \cdot (H_3O)_2 \cdot (H_2O)_{5.7}$ at 30 K, symmetry operations ¹ = (1-x, -y, 1-z), ² = (-1+x, y, z), ³ = (1+x, y, z), ⁴ = (1-x, 1-y, 1-z).

An interesting feature of this structure is that the central C = C bond does not seem to vary widely with changes in temperature, and the bond lengths are similar for both independent ET molecules within experimental error. The similarity in the C = C double bond length shows that both of the ET molecules play an equal part in carrying the charge transferred to the organic layer.

Charges calculated as described earlier (Equation 2.1) are shown in Table 3.3.3. these show that within experimental error these charges are all equal. Interestingly the

calculated charge for both independent ET molecules is above the expected 0.5, although no explanation for this has been found.

Temperature (K)	Central bond of ET	a (Å)	b (Å)	c (Å)	d (Å)	delta δ	Q
30	C5-C6	1.372(3)	1.742(1)	1.756(1)	1.360(2)	0.766(4)	0.63(3)
	C15-C16	1.374(3)	1.745(1)	1.757(1)	1.359(2)	0.769(4)	0.61(3)
120	C5-C6	1.375(3)	1.736(1)	1.751(1)	1.353(2)	0.759(4)	0.68(3)
	C15-C16	1.372(3)	1.740(1)	1.752(1)	1.356(2)	0.764(4)	0.65(3)

Table 3.3.3: Calculated charges carried by the ET molecules in $\beta''(ET)_4[(NH_4)M(C_2O_4)_3]_2 18\text{-crown-6-ether} \cdot (H_3O)_2 \cdot (H_2O)_5$.

Full crystallographic data tables for

$\beta''(ET)_4[(NH_4)M(C_2O_4)_3]_2 18\text{-crown-6ether} \cdot (H_3O)_2 \cdot (H_2O)_5$ are found in Appendix D:

3.4 The study of the structure of: κ -(ET)₂Cu(SCN)₂

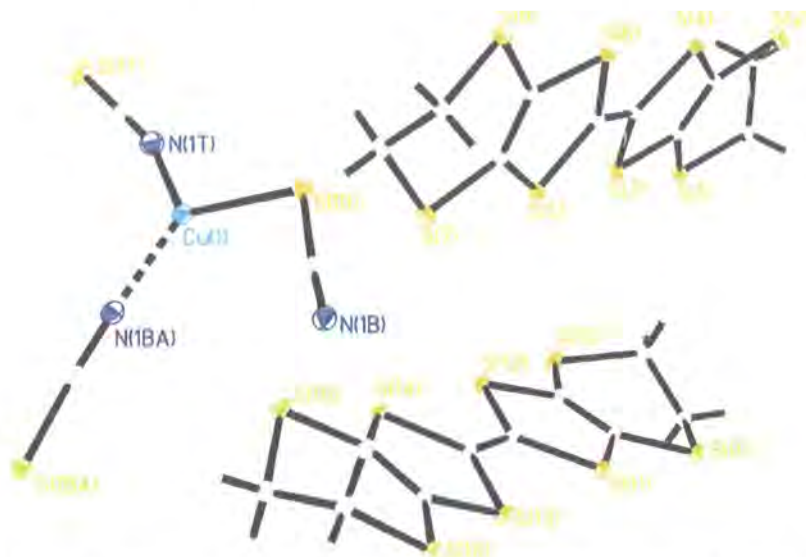


Figure 3.4.1: Thermal ellipsoid plot at 50% probability for κ -(ET)₂Cu(SCN)₂ at 60 K, symmetry equivalent ligand present (connected though dashed bond).

This structural study was undertaken in collaboration with Anne-Katrin Klehe (Clarendon laboratory, University of Oxford), to assist in the analysis of a high pressure single crystal neutron diffraction structure at 30 K. It was thought that a very low temperature X-ray diffraction structure would provide a starting point for a neutron dataset that had not been resolved. The crystals supplied were exactly those that were used in the neutron diffraction experiment on SXD (ISIS) at 30K, this required the extraction of the crystal from the neutron mount before any experiment could be performed. The experiment on SXD had been a multi-crystal diffraction experiment, but the sample provided, contained only one single crystal that had been cracked. The other two crystals had been destroyed in the neutron experiment and were no longer ‘single’. This remaining ‘single’ crystal had to be separated into the two components, along the fracture line, and the smaller block was used for the single crystal diffraction experiment on the SMART Apex diffractometer. This small block was still many times the size on the incident X-ray beam being $0.8 \times 0.7 \times 0.4 \text{ mm}^3$. Rather than cut this, risking losing the whole crystal, the experiments were conducted with this very large crystal, knowing from experience that with high redundancy, the multi-scan corrections could remove errors introduced from an oversized crystal. To quote Dr David Watkin (University of Oxford):

“it is better to use a good large crystal than a good small one”, BCA Autumn Conference 2002.

Experiments were therefore carried out at 30 and 60 K, the crystallographic details of which are found in Table 3.4.1 below. Data were collected at two temperatures to check for any change in the structure, or any crystallographic phase transition that may assist in the solution of the neutron diffraction data.

	30 K	60 K
Space Group	P2 ₁	P2 ₁
a (Å)	12.7788(11)	12.7859(7)
b (Å)	8.3882(8)	8.3907(4)
c (Å)	16.3434(15)	16.3411(9)
β°	111.498(3)	111.417(2)
Volume (Å ³)	1630.0(3)	1632.06(15)
Z	2	2
Ratio max/min transmission	0.558	0.556
μ mm ⁻¹	1.85	1.84
R _{INT}	0.0217	0.0183
R ₁ (F _o >4σF _o)	0.0197	0.0184
R ₁ (all)	0.0203	0.0191
R _w	0.0694	0.0631
GoF	1.211	1.243
Max residual (eÅ ⁻³)	0.68	0.63
Min residual (eÅ ⁻³)	-0.66	-0.46
Number of reflections observed / unique / (F _o >4σF _o)	13221 / 7165 / 7133	13560 / 7254 / 7201
Number of parameters	389	389

Table 3.4.1: Crystallographic data for κ-(ET)₂Cu(SCN)₂.

The quality of the data is shown clearly in Table 3.4.1, with residual electron density very low and data that are very self-consistent. The only hint that the data were collected from an unusual sample is the value of the maximum : minimum transmission ratio reported by the multi-scan correction. The thermal ellipsoid plot shown in Figure 3.4.1 also shows no unusual features from the refinement.

This molecular superconductor has been known since 1988²¹⁻²³ and has been the subject of many studies, as it was the highest temperature molecular superconductor, $T_c \approx 10.4$ K, known for two years until the discovery of κ -(ET)₂Cu[N(CN)₂]Br²⁴ with $T_c \approx 11.6$ K. The NCS ligand provides two different functions, as a bridging ligand between copper centres and then as a terminal ligand that is only bound to one copper centre. Ligand atoms were given a trailing character using the nomenclature from prior studies, *b* – bridging and *t* – terminal ligand atoms. The Cu atoms are 3 coordinate planar and form infinite chains through the crystal, shown in Figure 3.4.2.

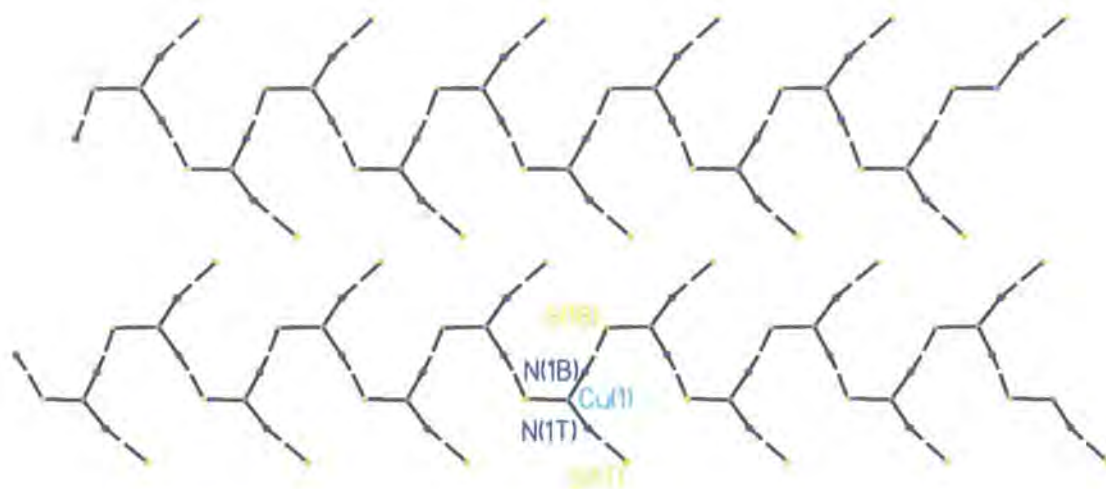


Figure 3.4.2 Infinite Cu chains formed through the crystal, viewed perpendicular to the *a-b* plane.

Table 3.4.2 shows the bond lengths found in the ligand species. There appears to be no real change between the structure at 30K and at 60 K, a feature further confirmed by the C = C double bond lengths shown for the ET molecules in Table 3.4.3. There is a clear difference however in the bonding of the bridging and terminal ligands, with the N1 – Cu1 bond being lengthened in the bridging ligand.

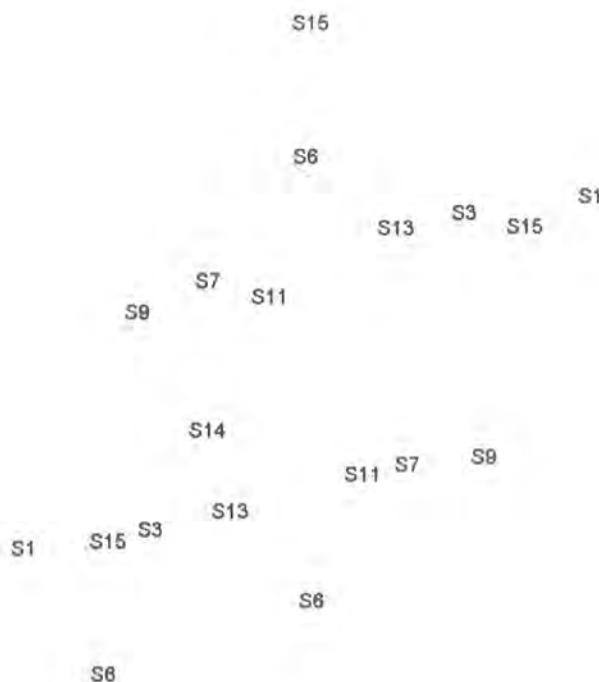
	Terminal		Bridging	
	30 K	60 K	30 K	60 K
N1 – C1	1.167(4)	1.163(3)	1.163(3)	1.162(3)
C1 – S1	1.640(3)	1.638(3)	1.655(2)	1.655(2)
S1 – Cu1	-	-	2.2365(8)	2.2341(7)
N1 – Cu1	1.919(2)	1.920(2)	1.934(2)	1.9312(19)

Table 3.4.2: Ligand bond lengths in κ -(ET)₂Cu(SCN)₂.

	C5 = C6	C15 = C16
30 K	1.372(3)	1.358(3)
60 K	1.372(3)	1.363(3)

Table 3.4.3: Crystallographically independent ET molecule C=C double bond lengths present in κ -(ET)₂Cu(SCN)₂.

The important intermolecular S – S contacts were also determined for κ -(ET)₂Cu(SCN)₂ at 30 K. They are presented in Table 3.4.4 and correspond to the contacts shown in Figure 3.4.3

Figure 3.4.3: S – S contacts for κ -(ET)₂Cu(SCN)₂ at 30 K

	Length (Å)		Length (Å)
S1 – S15 ¹	3.5082(10)	S7 – S13 ¹	3.5385(9)
S3 – S15 ¹	3.5250(10)	S7 – S11 ¹	3.5574(10)
S6 – S15 ²	3.4880(8)	S7 – S14	3.5629(8)
S6 – S13 ³	3.5462(8)		

¹symm (1-x, 1/2+y, 1-z), ²symm (-1+x, y, z), ³symm (1-x, -1/2+y, 1-z),

Table 3.4.5: Short S – S contacts for κ -(ET)₂Cu(SCN)₂ at 30 K.

Full crystallographic details for κ -(ET)₂Cu(SCN)₂ can be found in Appendix D. Details of the refined structure were sent to assist in the neutron data reduction solution and refinement. No further information on the progress of this analysis is available to the author at this time.

The calculated charges of the independent ET molecules are shown in Table 3.4.5. They show no major redistribution in charge, but this is only over a small temperature range although the results still appear to show the presence of a greater localisation of charge on one ET molecule.

Temperature (K)	Central bond of ET	a (Å)	b (Å)	c (Å)	d (Å)	delta δ	Q
30	C5-C6	1.372(3)	1.741(1)	1.753(1)	1.359(2)	0.763(4)	0.65(3)
	C15-C16	1.358(3)	1.747(1)	1.755(1)	1.354(2)	0.790(4)	0.45(3)
60	C5-C6	1.372(3)	1.740(1)	1.750(1)	1.359(2)	0.759(4)	0.68(3)
	C15-C16	1.363(3)	1.745(1)	1.754(1)	1.353(2)	0.783(4)	0.51(3)

Table 3.4.6: Calculated charges (Q) carried by the ET molecules in κ -(ET)₂Cu(SCN)₂, see Equation 2.1.

3.5 The study of the structure of:

$\alpha\beta$ -(ET)₄[(H₃O)Ga(C₂O₄)₃]PhN(CHO)CH₃

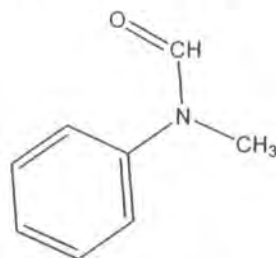


Figure 3.5.1: The guest molecule for $\alpha\beta$ -(ET)₄[(H₃O)Ga(C₂O₄)₃]PhN(CHO)CH₃.

This compound, $\alpha\beta$ -(ET)₄[(H₃O)Ga(C₂O₄)₃]PhN(CHO)CH₃, was submitted for full variable temperature structural analysis by Dr S.S. Turner (R.I. then University of Exeter), it is structurally very different from the other compounds presented in this chapter. The major difference is in the packing of the ET layers, which alternate between α and β layers between the metal oxalate layers shown in Figure 3.5.2.

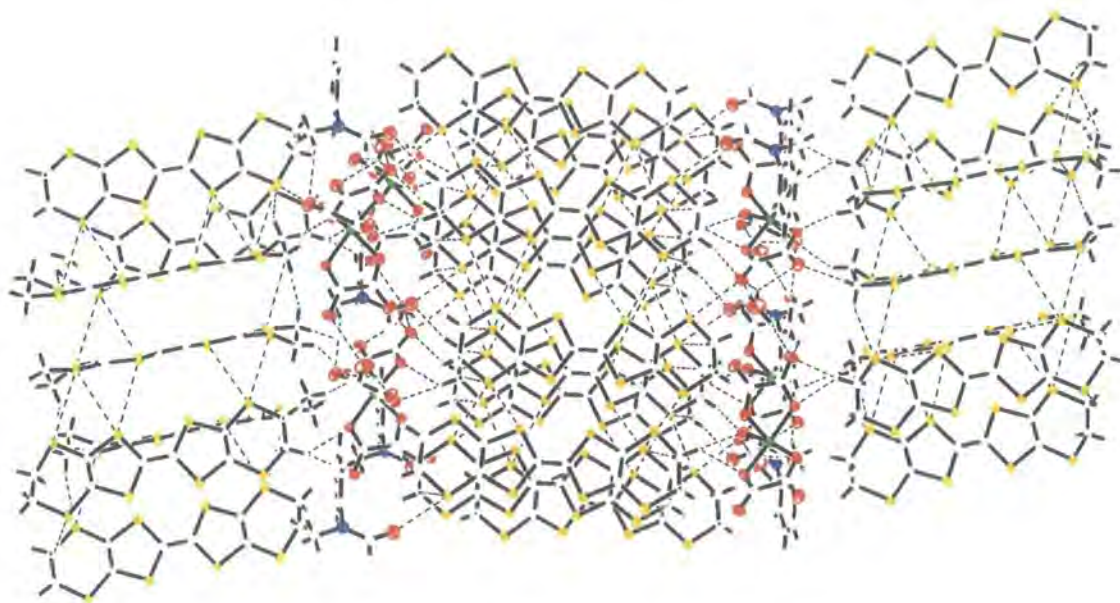


Figure 3.5.2: Packing diagram of $\alpha\beta$ -(ET)₄[(H₃O)Ga(C₂O₄)₃]PhN(CHO)CH₃ at 190 K, showing the alternating stacking of the ET molecules.

The guest molecule also has a bulkier functional group on the phenyl ring this functional group alters how the guest molecule is placed in the cavity formed by the metal oxalate layer. The phenyl ring, of the guest molecule, is forced to one side of the cavity and the aldehyde group to the other, the cavity is also elongated along the length of the guest molecule shown in Figure 3.5.3.

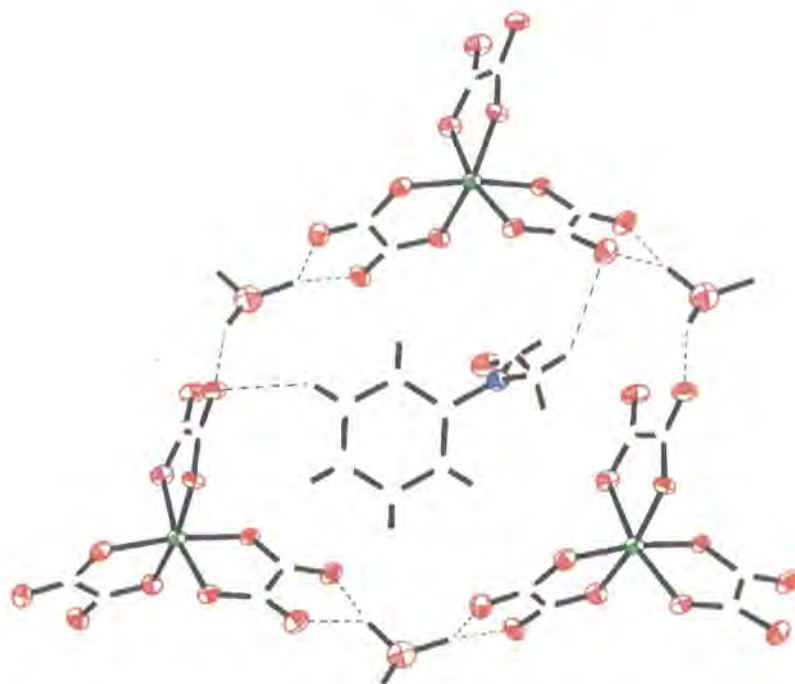


Figure 3.5.3: The cavity in the metal oxalate layer containing the guest molecule in $\alpha\beta$ - $(\text{ET})_4[(\text{H}_3\text{O})\text{Ga}(\text{C}_2\text{O}_4)_3]\text{PhN}(\text{CHO})\text{CH}_3$ at 190 K.

At the time of writing the physical property measurements were unavailable to the author. The crystals, in common with this group of compounds, were very dark red/black, but they appeared to be of an excellent quality and an ideal size for X-ray diffraction measurements. This promised much for the structural analysis of this material. A room temperature (290 K) X-ray structure analysis was carried out, using data collected on a SMART Apex diffractometer, in order to confirm the crystal quality. The resulting crystallographic parameters are listed in Table 3.5.1 below, together with data collections at four different temperatures: 270, 250, 230 and 210 K.

The results of the room temperature data collection were very good and therefore the sample was cooled to 90 K to assess the potential of very low temperature studies. The diffraction pattern obtained from a quick matrix data collection at 90 K showed the crystal had passed through some near destructive transition, as the diffraction pattern had degraded in quality to a very large extent. Another crystal was mounted and flash cooled to 90 K in an attempt to avoid catastrophic transition, this failed and the diffraction pattern obtained was once again unusable. It was thought that passing through the transition slowly may allow the crystal to react better to the changing conditions so various rates of cooling were attempted on different crystals, all with

similar results. Cooling at 5 K an hour to 90 K resulted in the diffraction pattern shown on the left in Figure 3.5.4 and on the right is the diffraction pattern of the same crystal in a very similar orientation at 290 K.

Formula	290 K	270 K	250 K	230 K	210 K
Space Group	P-1	P-1	P-1	P-1	P-1
a (Å)	9.696 (1)	9.659 (1)	9.610(2)	9.611(1)	9.589(1)
b (Å)	11.233 (1)	11.223 (1)	11.200(2)	11.213(1)	11.202(1)
c (Å)	37.984 (4)	37.959 (5)	37.899(7)	37.950(3)	37.951(5)
α°	81.904(2)	81.807(2)	81.723(3)	81.738(1)	81.669(2)
β°	85.377(2)	85.375(2)	85.355(3)	85.363(1)	85.345(2)
γ°	65.276(2)	65.405(2)	65.498(3)	65.598(1)	65.649(2)
Volume (Å ³)	3719.7(7)	3702.4(8)	3672.2(12)	3684.6(5)	3673.6(8)
Z	2	2	2	2	2
μ mm ⁻¹	1.33	1.34	1.35	1.34	1.35
R _{INT}	0.0269	0.0284	0.0346	0.0285	0.0362
R ₁ (F _o >4 σ F _o)	0.0490	0.0454	0.0477	0.0535	0.0661
R ₁ (all)	0.0821	0.0722	0.0760	0.0812	0.0983
R _w	0.1043	0.1030	0.1102	0.1026	0.1243
GoF	1.010	1.005	0.987	1.096	1.176
Max residual (eÅ ⁻³)	0.64	0.54	0.60	-0.49	0.54
Min residual (eÅ ⁻³)	-0.43	-0.44	-0.35	-0.40	-0.43
Number of reflections observed	24898 / 13738 /	24385 / 13538 /	24629 / 13622 /	24684 / 13632 /	23948 / 13333 /
/ unique / (F _o >4 σ F _o)	9571	9846	9868	10153	9634
Number of parameters	931	931	931	931	931

Table 3.5.1: Crystallographic data for: $\alpha\beta$ -(ET)₄[(H₃O)Ga(C₂O₄)₃]PhN(CHO)CH₃ at temperatures shown.

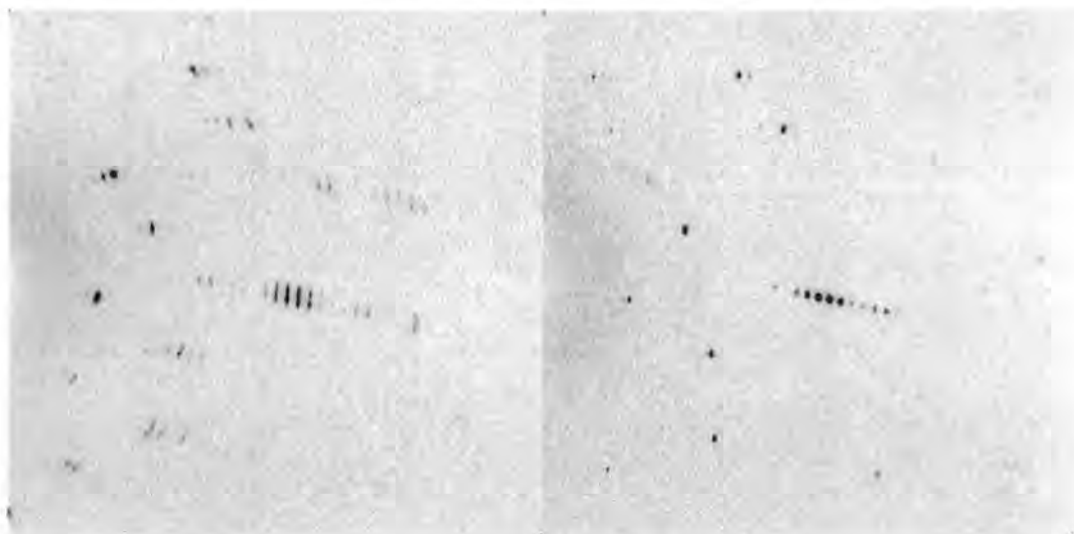


Figure 3.5.4: Diffraction pattern images at 90 K and 290 K, images created using *FRM2FRM*²⁵.

As no methods of cooling were found to achieve the desired results structural determinations were undertaken at 20 K intervals cooling from room temperature. The results of the first 4 of these data collections are shown in Table 3.5.1. Below this the deterioration in the diffraction pattern became markedly more noticeable and integration statistics decayed rapidly the final successful structure solution and refinement was carried out at 190 K, crystallographic parameters are found in Table 3.5.2. Results of measurements of the crystal at lower temperatures are not presented, with the exception of a 90 K dataset used for comparison. The onset of this degradation in data quality is apparent in the refinement statistics becoming worse for the lower temperatures and the 270 K structure affording the 'best' results.

The reflections appear at first to broaden and stretch, indicating an increasing mosaicity in the crystal, eventually becoming highly overlapped with the neighbouring reflections. Attempts were made to overcome this by using a larger sample to detector distance to allow greater separation of the reflections, then to use a large integration box size to capture the whole reflection profile. Results from these attempts were no better. The diffraction pattern suggests the crystal is losing some internal order possibly moving to an incommensurate state. The latter of these appears to be quite likely, as when the samples are warmed again, to room temperature good diffraction patterns are generally found, with only minor degradation from the original diffraction. With this in mind, attempts were made to establish the Q – vector for the structure, if this could be found

then the structure could still be resolved with special treatment. Unfortunately this was not possible for any of the samples investigated.

Notwithstanding a crystal was cooled very slowly to 30 K, in the hope that the transition would be passed though before reaching the base temperature and the crystal would return to an ordered state. The absence of 30 K data in this thesis for this compound because no resolution of the transition could be achieved, indeed not even a satisfactory unit cell size could be determined at 30 K.

Using the best of the 90 K datasets collected, an integration was performed on the data, knowing that the results would be of poor quality. The results are shown in Table 3.5.2. The 'solution' of this data occurred perfectly with very convincing figures of merit, the refinement was however not ideal. Heavy constraints had to be applied to the C atom thermal parameters to avoid non positive definite atoms. All C atoms in similar environments were restricted to have the same U_{ij} matrix. The hydrogen atoms for the protonated water counter ion could not be found. Molecular parameters derived from this refinement should be treated with care, as the broadness of the reflections that were integrated to provide these data, induced errors in the unit cell determination and hence any parameters derived from it.

Multi temperature analysis of the structure sheds some light on the changes the crystal undergoes on cooling. Figure 3.5.5 shows an overlay of the 4 independent ET molecules at different temperatures. These overlays were created by defining a common plane for all of the molecules through the 4 central S atoms (S3*, S4*, S5*, S6* where * is A, B, C, D). This figure shows that different temperatures have some common features, the ethylene groups at one end of the ET's all have the same orientation, whilst the other end of the molecule there are two different orientations. On close inspection it can be seen that the 4 independent ET molecules behave differently with decreasing temperature, in particular one of the ET molecules has an increased curvature (deviation away from the mean plane of the molecule) on cooling, this ET molecule is located in the β stacked layer. Additionally the 4 ET molecules deviate more from their average position on cooling.

Temperature (K)	90	190
Space Group	P-1	P-1'
a (Å)	9.575(2)	9.5783(11)
b (Å)	11.243(3)	11.2092(13)
c (Å)	38.033(9)	37.9726(43)
α°	81.525(3)	81.635(2)
β°	87.715(4)	85.337(2)
γ°	65.978(3)	65.735(2)
Volume (Å ³)	3697.7(15)	3676.2(7)
Z	2	2
Ratio max/min transmission	0.706	0.716
μ mm ⁻¹	1.34	1.35
R _{INT}	0.0489	0.0373
R ₁ (F _o >4 σ F _o)	0.1544	0.0857
R ₁ (all)	0.1757	0.1103
R _w	0.3373	0.1721
GoF	1.261	1.290
Max residual (eÅ ⁻³)	1.403	0.66
Min residual (eÅ ⁻³)	-1.444	-0.71
Number of reflections observed / unique / (F _o >4 σ F _o)	23493 / 13452/ 10378	24367 / 13452 / 10378
Number of parameters	637	931

Table 3.5.2: Crystallographic data for: $\alpha\beta$ -(ET)₄[(H₃O)Ga(C₂O₄)₃]PhN(CHO)CH₃ at 90 and 190 K.

This deviation could be the cause for detrimental effect that cooling has on this sample, with the crystal entering a state with increase internal strain. Table 3.5.3 shows the central C = C double bond for the independent ET molecules at these three temperatures. It is difficult to draw any conclusions or see any clear trends given the low resolution data and the calculated errors.

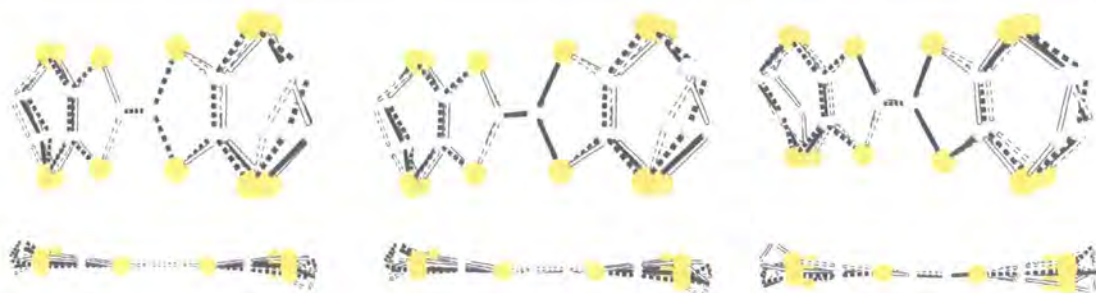


Figure 3.5.5: Overlay of 4 independent ET molecules at 290 K, 190 K and 90 K from left to right respectively. Different molecules represented by differing bond colouring.

This is the molecule that has an increased curvature on cooling. These are possible indications that the charge is localising on this molecule, the curvature of an ET molecule has previously [French⁷ *et al*], been linked to both of these parameters, the central C = C bond length and the curvature of the molecule.

C5 – C6	290 K	190 K	90 K
A	1.364(5)	1.344(11)	1.36(3)
B	1.361(5)	1.347(11)	1.31(3)
C	1.355(5)	1.354(11)	1.37(3)
D	1.346(5)	1.339(11)	1.35(3)

Table 3.5.3: ET molecules' central C = C bond lengths. Molecules A and B belong to the β -layer, molecules C and D belong to the α -layer

The calculated charges supported on the ET molecules are shown in Table 3.5.4, the lower temperature results show that the method for their calculation is dependent on high quality data being available. The 290 K show an interesting separation of charge across the independent molecules and these calculations derive from much higher quality data, before the crystal had passed through its unresolved phase transition.

Temp. (K)	ET	a (Å)	b (Å)	c (Å)	d (Å)	delta δ	Q
90	A	1.36(3)	1.764(9)	1.769(9)	1.35(1)	0.823(34)	0.20(25)
	B	1.31(3)	1.776(9)	1.770(9)	1.34(2)	0.896(38)	-0.34(38)
	C	1.37(3)	1.764(9)	1.769(9)	1.35(2)	0.818(37)	0.24(28)
	D	1.35(3)	1.753(9)	1.747(9)	1.37(2)	0.785(37)	0.49(28)
190	A	1.344(8)	1.740(4)	1.747(4)	1.361(8)	0.782(12)	0.18(9)
	B	1.347(8)	1.753(4)	1.752(4)	1.364(8)	0.794(12)	0.43(9)
	C	1.354(8)	1.749(4)	1.758(4)	1.341(8)	0.812(12)	0.28(9)
	D	1.339(8)	1.756(4)	1.763(4)	1.340(8)	0.840(12)	0.07(9)
290	A	1.364(6)	1.732(2)	1.742(0)	1.354(4)	0.757(8)	0.70(6)
	B	1.361(6)	1.742(2)	1.750(0)	1.352(4)	0.779(8)	0.52(6)
	C	1.355(6)	1.744(3)	1.754(0)	1.338(4)	0.805(8)	0.33(6)
	D	1.346(6)	1.748(3)	1.752(0)	1.340(4)	0.814(8)	0.28(6)

Table 3.5.4: Calculated charges supported by the independent ET molecules in $\alpha\beta$ -(ET)₄[(H₃O)Ga(C₂O₄)₃]PhN(CHO)CH₃. Molecules A and B belong to the β -layer, molecules C and D belong to the α -layer

3.6 The study of the structure:

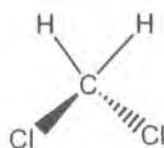


Figure 3.6.1: Dichloromethane, the guest molecule in $\beta''(ET)_4[(H_3O)Ga(C_2O_4)_3]CH_2Cl_2$

We studied another host : guest combination in this series this time with dichloromethane as the guest molecule. Crystals of this compound were of lower quality than those previously studied, although one crystal did result in good quality diffraction and data were collected on this crystal at 120 K on a SMART 1K diffractometer. The results are summarised in Table 3.6.1 below, and as for previous members of this series the symmetry of the structure appeared to agree with space group $C2/c$ and yielded a good solution and refinement. Figure 3.6.2 shows the plot of the thermal ellipsoids of the asymmetric unit for this crystal, it can be seen that there is once again a disorder in one of the ethylene groups of one of the ET molecules. There is also minor disorder in the CH_2Cl_2 molecule, which is not an uncommon feature where CH_2Cl_2 is the solvent molecule.

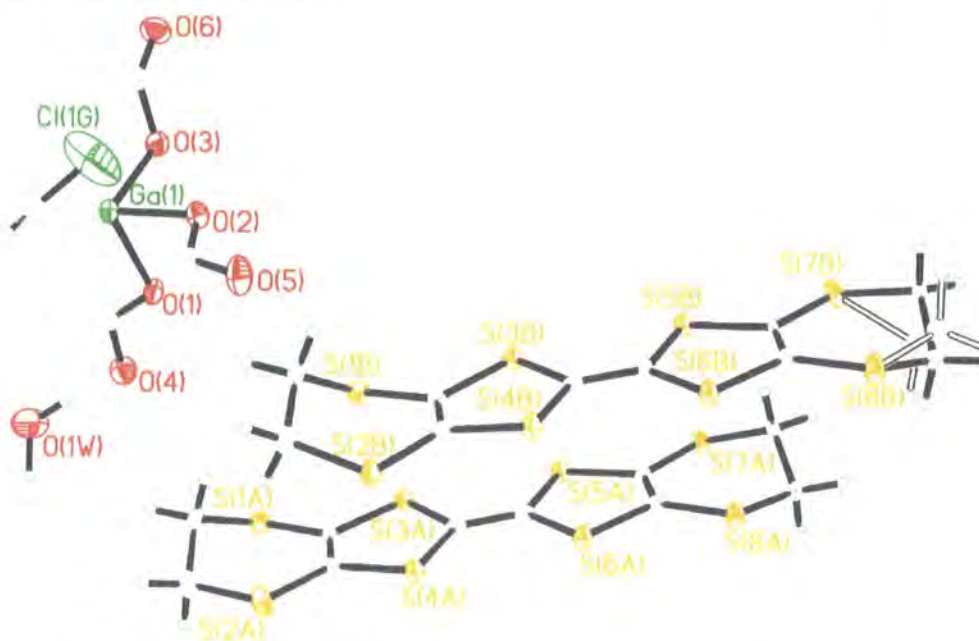


Figure 3.6.2: Thermal ellipsoid plot of $\beta''(ET)_4[(H_3O)Ga(C_2O_4)_3]CH_2Cl_2$ at 120 K ellipsoids shown at 50% probability level.

Cooling this crystal to 30 K resulted in another good diffraction pattern, despite the reflections broadening, thus showing an increased mosaicity in the sample. The integration statistics reflected this, with an increase in R_{int} compared to the higher temperature structure. The integration box size had to be increased significantly to capture the entirety of reflections along with an increase in the number of frames kept in the frame buffer during integration. Resolution of the space group was ambiguous; a significant number of systematic absence violations were present for the space group to be exactly $C2/c$ and solution of the structure occurs readily in space group $C2$ however any reasonable refinement of the data was not possible. The 'true' space group is not known, except that it has lower symmetry than $C2/c$. From the attempted solutions in both space groups, it appears that the CH_2Cl_2 molecule breaks the symmetry, attempts to refine the structure with a highly disordered molecule were inconclusive.

Space Group	$C2/c$
a (Å)	10.2661(7)
b (Å)	19.7010(14)
c (Å)	34.887(3)
β°	93.943(1)
Volume (Å ³)	7039.3(9)
Z	4
Ratio max/min trans.	0.675
$\mu \text{ mm}^{-1}$	1.48
R_{INT}	0.0783
$R_1 (F_o > 4\sigma F_o)$	0.0757
R_1 (all)	0.1228
R_w	0.1178
GoF	1.159
Max residual (eÅ ⁻³)	1.782
Min residual (eÅ ⁻³)	-1.358
Number reflections observed/unique/($F_o > 4\sigma F_o$)	29925 / 8157/ 5598
Number of parameters	434

Table 3.6.1: Selected crystallographic details for $\beta''(\text{ET})_4[(\text{H}_3\text{O})\text{Ga}(\text{C}_2\text{O}_4)_3]\text{CH}_2\text{Cl}_2$ at 120 K.

The limited 120 K data afford a minor structural analysis to be completed. The frequently observed disorder in a terminal ethylene group is present, even at 120 K. Analysis of the central C = C double bond length of the independent ET molecules shows it to be the same within experimental error, so it appears that there has been no charge localisation onto a single ET molecule, at least not at this temperature. This is confirmed by the calculation of the molecules' charge (see Equation 2.1), resulting in charges of 0.42 and 0.46. These results are not conclusive however as the data quality restricts any high level analysis of the structure.

Crystallographic tables for $\beta''(ET)_4[(H_3O)Ga(C_2O_4)_3]CH_2Cl_2$ are found in Appendix D.

3.7 References

- 1 Akutsu, H.; Akutsu-Sato, A.; Turner, S.S.; Day, P.; Tocher, D.A.; Probert, M.R.; Howard, J.A.K.; Le Pevelen, D.; Klehe, A-K.; Singleton, J.; Laukhin, V.N., *Syn. Metals* **137**, 2003, 1239-1240.
- 2 Akutsu, H.; Akutsu-Sato, A.; Turner, S.S.; Le Pevelen, D.; Day, P.; Laukhin, V.; Klehe, A-K.; Singleton, J.; Tocher, D.A.; Probert, M.R.; Howard, J.A.K., *J. Am. Chem. Soc.*, 2002, **124**, 12430.
- 3 SAINT -NT, Data Reduction Software, version 6.12; Bruker Analytical X-ray Instruments Inc.: Madison, Wisconsin.
- 4 SHELXTL, version 5.1; Bruker Analytical X-ray Instruments Inc.: Madison, Wisconsin.
- 5 Geiser, U., *Proceedings of the 28th Int. School of Crystallography, Erice, Italy, 1999*.
- 6 Martin, L.; Turner, S.S.; Day, P.; Guionneau, P. Howard, J.A.K; Uruichi, M. Yakushi, K., *J. Mater. Chem.*, 1999, **9**, 2731-2736.
- 7 French, S.A.; Catlow, C.R.A., *J. Mater. Chem.*, 2001, **11**, 2102-2107.
- 8 Rahal, M.; Chasseau, D.; Gaultier, J.; Ducasse, L.; Kurmoo, M.; Day, P., *Acta Cryst.*, 1997, **B53**, 159-167.
- 9 G. M. Sheldrick, SADABS, Empirical Absorption Correction Program. University of Göttingen, Germany, 1998.
- 10 Copley, R.C.B.; Goeta, A.E.; Lehmann, C.W.; Cole, J.C.; Yufit, D.S.; Howard, J.A.K.; Archer, J.M.; *J. Appl. Cryst.*, 1997, **30**, 413-417.
- 11 Allibon, J.R., 1996, *MAD Diffractometer Control Software – AlphaVMS version*. Institute Laue-Langevin (DPT/SCI), Grenoble, France.
- 12 APD 202 Displex cryogenic refrigerator.
- 13 J. Cosier and A.M. Glazer, *J. Appl. Cryst.*, 1986, **19**, 105.
- 14 A.E. Goeta; L.K. Thompson; C.L. Sheppard; C.W. Lehmann; J. Cosier; C. Webster; J.A.K. Howard *Acta Cryst.*, **C55**, 1999, 1243-1246.
- 15 Sharma, S.; Paulus, H.; Weiden, N.; Weiss, A.L., *Z. Kristallogr.*, **171**, 101-112.
- 16 Bruno, I.J.; Cole, J.C.; Edgington, P.R.; Kessler, M.K.; Macrae, C.F.; McCabe, P.; Pearson, J.; Taylor, R., *Acta Cryst.*, **B58**, 389-397, 2002.
- 17 Kittel, C., *Quantum Theory of Solids*, Wiley, New York, 1963.

- 18 Guionneau, P.; Kepert, C.J.; Bravic, G.; Chasseau, D.; Truter, M.R.; Kurmoo, M.; Day, P., *Syn. Metals*. **86**, 1997, 1973-1974.
- 19 Akutsu-Sato, A.; Akutsu, H.; Turner, S.S.; Day, P.; Probert, M.R.; Howard, J.A.K.; Akutagawa, T.; Takeda, S.; Nakamura, T.; Mori, T., *Angew. Chem. Int. Ed.* **2005**, *44*, 292-295.
- 20 Akutsu-Sato, A.; Akutsu, H.; Turner, S.S.; Le Pevelen, D.; Day, P.; Light, M.E.; Hursthouse, M.B; Akutagawa, T.; Nakamura, T., *Syn. Metals*. **135-136**, 2003, 597-598.
- 21 Urayama, H.; Yamochi, H.; Saito, G.; Nozawa, K.; Sugano, T.; Kinoshita, M.; Sato, S.; Oshima, K.; Kawamoto, A.; Tanaka, J. *Chem. Lett.* **1988**, *55*.
- 22 Gärtner, S.; Gogu, E.; Heinen, I.; Keller, H.J.; Klutz, T.; Schweitzer, D., *Solid State Commun.* **1988**, *65*,1531.
- 23 Carlson, K.D.; Geiser, U.; Kini, A.M.; Wang, H.H.; Montgomery, L.K.; Kwok, W.K.; Beno, M.A.; Williams, J.M.; Cariss, C.S.; Crabtree, G.W.; Whangbo M.-H.; Evain, M., *Inorg. Chem.* **1988**, *27*, 965.
- 24 Kini, A.M.; Geiser, U.; Wang, H.H.; Carlson, K.D.; Williams, J.M.; Kwok, W.K.; Vandervoort, K.G.; Thompson, J.E.; Stupka, D.L; Jung, D.; Whangbo M.-H., *Inorg. Chem.* **1990**, *29*, 2555.
- 25 FRaMe to FRaMe image file format conversion utility. Version 1.0.10
Copyright 1997-1999 Bruker AXS.

Chapter 4:

Introduction to charge density theory and experiments.

4.1 Theoretical introduction

As with many divisions of modern science, X-ray crystallography is founded on a variety of assumptions. The particular experiment undertaken and the desired results often predetermine which assumptions and hence in X-ray experiments, which scattering formalism should be imposed. X-ray crystallography has become a very powerful and widely used tool for the characterization of crystalline compounds. The application of structural solution to confirm chemical connectivity is based on the standard spherical independent atom (IAM) formalism, in which the molecule is approximated by the promolecule and the atoms are treated as spherical, non-interacting objects, where all of the associated electron density is assumed to be found.

$$\rho_{IAM}(r) = \sum_k \rho_k^o(r - R_k)$$

Equation 4.1.1: The spherical atom formalism, where ρ_k^o is the electron density of the k^{th} atom centred at R_k .

If the experimentalist desires to understand more fully the electronic structure i.e. bonding interactions and lone electron pair locations, then a more rigorous formalism must be imposed to allow for the deviation from the spherical atom model. Herein lies a brief summary of the various formalisms that have been introduced and developed, eventually leading to the widely used Hansen and Coppens¹ formalism. This formalism has been applied in one guise or another, in many of the charge density refinement packages – such as the one used throughout this work: XD².

In 1915 Debye wrote:

“The experimental study of the scattering of atoms, in particular light atoms, should get more attention, since along this way it should be possible to determine the arrangement of the electrons in the atoms”

4.1.1 Shortfalls of the IAM model

It is well known and understood that the atom as an independent object exists in a somewhat different state to that when it is bound in a molecule. The deviation from the independent atom can be observed most clearly for the lighter elements, where the ratio of *valence* electrons to *core* electrons is at its greatest. Take for example, the special case of a hydrogen atom which contains only one valence electron and no core electrons. It was noted early in the development of crystallographic studies that H-X bonds (where X is another atom and most commonly: N, C, O) were significantly shorter than was expected³ and indeed had been found from other analysis techniques⁴. This is a resultant problem from using the IAM model, as the formalism assumes that an atom will be located at a peak in electron density. The electron density of an hydrogen atom contributes 100% to its valence and therefore when it is bound to another atom, the centre of the hydrogen atom appears to be ‘inside the bond’! This effectively causes any least squares refinement program to move the hydrogen atom in the model closer to the bound atom, thus apparently shortening the bond. Another major inadequacy with the IAM is that the formalism does not allow for partial charge transfer between atoms. This means that all bonds are classed as being non polar, a result that contradicts even the basic electronegativity principles in modern chemistry.

4.1.2 The Spherical Kappa formalism

An intuitive improvement to the IAM is to separate the core (ρ_{core}) and the valence (ρ_{valence}) electron density of an atom in the model and allow ρ_{valence} to expand. This became known as the Kappa formalism owing to the κ expansion parameter of the valence electron density of an atom.

$$\rho_{\text{atom}} = \rho_{\text{core}} + P_v \kappa'^3 \rho_{\text{valence}}(\kappa'_r)$$

Equation 4.1.2: The Kappa formalism, where P_v is the population of the valence shell and κ' denotes an expansion or contraction coefficient for the valence shell.

This formalism can allow charge transfer between atoms i.e. allowing a theoretical implementation of the polarisability of a bond/molecule. The formalism still treats ρ_{core} and ρ_{valence} as spherical in the model. Although this treatment is itself flawed in that the valence electrons ideally should not be treated as spherical, it does largely give good agreements to the relative charges of atoms in molecules, showing the correct correlations to the electronegativity of those atoms. Figure 4.1.2 shows a schematic of the X-ray scattering factor of a non hydrogen atom, showing the difference between the core and valence electron scattering powers.

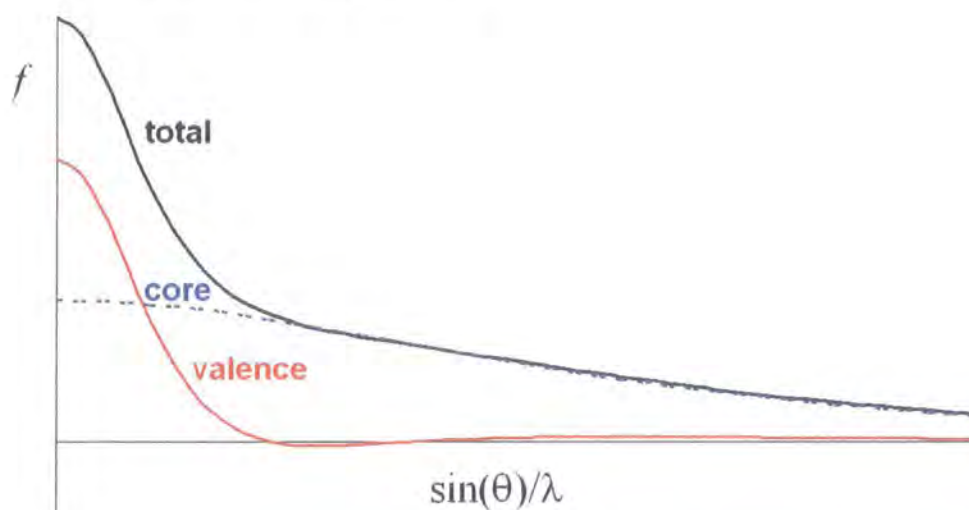


Figure 4.1.2: X-ray scattering factor schematic, for non hydrogen atoms, taken from presentation by Piero Macchi European Charge Density Meeting 2003.

4.1.3 Multipole model for Aspherical atoms

The need has been shown for a descriptor that allows for non spherical components of the valence density, and the most successful resolution of this has been through the use of atom-centered, multipolar functions where once again the electron density associated with an atom is divided into its *core* and *valence* terms. The valence electrons are then fitted to a multipolar expansion. The multipolar functions chosen are the spherical harmonic expansions, leading to dipole, quadrupole, octupole and hexadecapole expansions of the valence density. These allow for the non atom-centered electron density that can be seen to reconstruct many known bonding features to be refined. This formalism of Hansen and Coppens, shown in Equation 4.1.3, remains to date the most complete description of electron density in a form that can be analysed by X-ray diffraction.

$$\rho_{at}(r) = \rho_c(r) + P_v \kappa^3 \rho_v(\kappa r) + \sum_{l=0}^{l_{\max}} \kappa^{l^3} R_l(\kappa' r) \sum_{m=0}^{+l} P_{lm} d_{lm\pm}(\vartheta, \varphi)$$

Equation 4.1.3: The multipole formalism where:

ρ_c and ρ_v are the spherical core and valence densities respectively;

P_v represents the valence population;

κ represents expansion or contraction of the valence density;

κ' represents the expansion or contraction of the spherical harmonics;

l represents the level of the multipole expansion;

m corresponds to the orientation of l terms;

P_{lm} is the population constant for a given l and m ;

$d_{lm\pm}$ are the density-normalised real spherical harmonics expressed in polar coordinates

R_l represents the radial functions.

It is a treatment that allows the flexibility for polarisation, bonding orbitals and later has been shown to allow rigorous topological analysis of the results. The experimentalist, after a successful multipolar refinement has access to a vast array of chemically/physically important information e.g. d -orbital populations in organometallic compounds, dipole moments and thereby dipole enhancement due to crystal field effects when compared to quantum mechanical calculations and electrostatic potential fields.

This formalism has been implemented in a variety of least squares refinement programs for example POP⁵, VALRAY⁶ and XD². XD was the refinement and analysis package chosen for all of the studies presented in this thesis.

4.2 Experimental considerations: data collection and reduction.

4.2.1 Is there a need for a change from the standard experimental procedure?

To exploit fully the advanced formalism proposed and implemented by Hansen and Coppens, X-ray diffraction data of exceptional quality are required. It would be naïve of the experimentalist to expect that the standard machine settings would give data to the required level of precision. Much thought must be placed into both what is desired from the experiment and how the experiment should be conducted. All experimental discussions presented here relate to studies conducted using a Bruker SMART 6K diffractometer. The '*factory*' settings of the machine have been optimised for data collections relating to small organic structures, in order to give a reasonable degree of accuracy and rapid data collection times. These settings prove to be sufficient, with minor alterations, for the majority of routine studies conducted on the diffractometer. They do not stand up to the rigours of a charge density refinement and fail to deliver the required information of the precise accuracy required.

The choice of crystal also becomes an area where standards have to be higher than in a routine structure analysis. The increased number of parameters in the refinement needed to satisfy the multipole expansion terms, require a far greater number of observations for the refinement to be stable and meaningful. Since in a given volume of reciprocal space, there are only a finite number of reflections to be measured, the only route to increasing the number of observations is to expand the volume of reciprocal space sampled. Standard experiments collect data to approximately 60° in 2θ for Mo K_α , whereas in a charge density analysis, data are sampled to a minimum of 100° in 2θ for the same radiation. This requirement of diffraction data at much higher angles requires the crystal to be of very high quality. Defects or abnormalities in a crystal are a cause for its diffraction limit as they reduce the natural order of the crystal, upon which all diffraction experiments are based. Also lowering the temperature of the sample for

the data collection increases the number of high angle data that are accessible due to the reduction of the thermal motion in the sample.

4.2.2 Use of machines – adapting the collection strategy

As discussed above the settings of the instrument used for ‘ordinary’ structures is inadequate and one respect of this failing, is the need for finer ‘slicing’ of reciprocal space. An accurately measured peak profile is essential for the data collection to extract any subtle features of the electron density. The possibility of missing subtle, yet important features in the diffraction data, which could have far reaching implications in the overall results, has been shown previously in our laboratory when a phase transition was not seen using a 0.2° omega scan, only when this scan width was halved (0.1°) was the transition seen⁷. The general approach for charge density collections in the Durham laboratory historically has been to use 0.1° omega scans. However, this is dependent on the specific experiment, as it is preferable to have the reflections covering more than one frame to allow highly accurate peak profiles to be modelled. Also with smaller omega scans the very weak reflections stand out against the background more obviously as the crystal is in the required diffraction orientation for a greater length of time. It should be noted that this is directly in contradiction to techniques used by other manufacturers to gain their optimum data quality. The finer slicing of reciprocal space also means that the data collection strategy needs to be modified even to collect a typical volume of diffraction data, as for any given data collection, with a given number of frames being collected, a smaller volume of reciprocal space is sampled. Therefore the experimentalist must increase the number of frames collected in each ‘run’ to complete a desired 180° rotation in *omega* for a given phi angle.

The data/parameter ratio discussed above explains the need for collecting reflections to much higher values of *theta*. From a data collection point of view, this requires the detector to be positioned in at least 2 positions. The high angle data not only increase the number of observations accessible in the experiment, but also provide the opportunity to refine atomic positions separately from the multipole values. It is widely recognised that the diffraction intensity at high *theta* is due principally to the contribution of the *core* electrons, see Figure 4.1.2. To refine positions purely from

these data, can remove potential errors introduced by the effect of bonding density on the positioning of the atoms in the asymmetric unit. The bonding density affects the atomic positions in this way when the ratio of core to bonding density is low, such as in bonds involving hydrogen atoms, or when triple bonds are found between lighter elements.

4.2.3 Redundancy and pre-calculated completeness

Data are collected to as high a completeness and redundancy as is reasonably possible. The discussion of the need for higher redundancy values has been addressed earlier in this work, but requires reinforcement here, as the accuracy of the determination of the intensity of reflections is absolutely paramount in these studies. Preferentially, the average redundancy of a reflection collected should be of the order greater than 12 with a minimum of no less than two measurements. This helps to improve the accuracy of the measurement and thereby the weight it carries in refinement. It is difficult experimentally and sometimes impossible to collect 100% of the data to the highest angle, without changing the crystal's fixed orientation with respect to the machine's setting angles, as the machine has some physical restrictions on its motion, the greatest of these being the limitation in χ . This is a problem that is inherent in the modern 3 circle diffractometer, a problem overcome by the Kappa orientation that is fast becoming the preferred mode, in which there is a small amount of possible movement of the χ angle. The only possible solution to overcome this problem with a true 3 circle diffractometer, would be to remount the crystal in a different orientation, which could introduce other errors into the experiment since the crystal will be exposed to extreme variation in temperatures. With this in mind data are nominally collected to greater than 98% completeness to a resolution in $\sin\theta/\lambda$ of 1.04 \AA^{-1} for charge density studies. ASTRO⁸ is the program used to calculate the completeness and redundancy of a data collection before the experiment is completed, it utilises the orientation matrix of the sample and the configuration of the diffractometer to determine which data are collected in each user input strategy. The program also can display to the user any reciprocal space that is not sampled to allow the data collection to be altered to gain greater completeness.

4.2.4 Duration of the diffraction experiment

With such high demands on the completeness and redundancy of data, the length of the data collection is significantly increased. This is not without its drawbacks and restrictions. The cost of the experiment is relatively insignificantly increased but the demand for the equipment can mean that continuous running for one experiment has to be carefully planned. More importantly the stability of the apparatus is challenged as the machinery needs to run constantly for up to a week without any minor failures, especially in terms of the cryo-refrigeration, which can have catastrophic effects if the crystal either warms up or ice forms around it, which can happen on open flow cryo-refrigeration devices. The temperature of the experiment and its stability are of utmost importance; reduced thermal vibrations increase the inherent order in the system and as such increase the number and intensity of observed reflections. Mallinson⁹ showed that experiments could have up to 150 fold increase in the intensity at $\sin\theta/\lambda = 1.0\text{\AA}^{-1}$ for measurements taken at 100 K compared to 298 K, and that the observable data can be increased by a factor of 2 on cooling to 10 K from 100 K. Any variation in temperature during the experiment therefore has a great impact on the measured intensities. A succinct explanation of this can be found in the text edited by Domenicano and Hargittai¹⁰ (page 240).

4.2.5 Data processing

The integration of the data: a more careful approach is required, as with all parts of the experiment, compared to that of the 'standard' X-ray experiment. The software is semi intelligent with respect to the volume for each reflection to be integrated i.e. that the physical size of the reflections will increase with increasing angle. This should mean that the data can be consolidated in a single integration, giving easy access to statistics for the entire data collection on the same scale. Experience shows that this increased integration box size is not computed satisfactorily, along with some other parameters that change at higher angles, such as the scaling of the data to a degrees per minute value. Hence the preferred method is to integrate in separate 'batches' for each position of the detector. The separate integrations are merged after the integration has been carried out and are discussed below.

Two main approaches for ‘merging’ are used:

XPREP¹¹: This is the more standard approach and it is integral to the SHELXTL¹¹ package. It appears to have problems with the scaling of one merged raw file and another, although there are options for linear scaling between the data files and isotropic scaling, (see later for a detailed description). Errors were attributed to this batch scaling after rigorous testing of refinement strategies were completed¹³.

SORTAV¹⁴: This program offers a higher degree of flexibility to the treatment of the merging, scaling and corrections applied to the data, allowing machine dependent settings to be input for specific corrections. Output from this program is much more verbose than other programs, giving greater detail about potential problems with the data, for example which of the reflections are being removed, and which are being scaled and the scaling factor. The output can show the user if there is a problem with the data, but not where this problem originates.

Absorption and other systematic error corrections:

Most corrections to the data are applied at the point of integration (Lorentz polarisation, face plate transmission lengths, initial scaling). Further corrections to the data may be desired to account for systematic errors introduced by non spherical crystals providing non-uniform transmission lengths and absorption corrections for crystals containing heavy elements. Two main programs can be used for this: SORTAV¹⁴ and SADABS¹⁵, both will be discussed at length in later sections.

4.3 Interpretation of results

Most of the interpretation of the results presented in this thesis are based on the theory of Bader “Atoms in molecules” (AIM)¹⁶. The electron density of a material, $\rho(r)$, has a real physical value at each point in space, classified as a scalar field defined over 3 dimensional space. Such a scalar field’s topological properties can be summarised by the number and type of ‘critical points’ that are located in the field, critical points being

where the gradient of the field is zero, i.e. $\frac{d\rho}{dr} = 0$. There are 4 possible stable critical points of $\rho(r)$ each associated with a particular element of a structure. Each critical point has an associated rank (w) and signature (σ) being categorised (w, σ) . The rank of a critical point is equal to the number of non zero curvatures of ρ at the critical point. The signature is equal to the algebraic sum of the signs of the curvatures of ρ at the critical point. The four stable critical points are shown in Table 4.3.1.

Type of critical point (w, σ)	Explanation
(3, -3)	These occur at all nuclear positions, as all of the curvatures are negative.
(3, -1)	These are bond critical points (bcp), see Figure 4.3.1. These must exist between atoms that are bonded.
(3, +1)	These are ring critical points (rcp), which possess two local minima which correspond to the plane of the ring.
(3, +3)	These occur at a point that is a minima in all three dimensions and occur in the centre of atom cages (ccp).

Table 4.3.1: Types of stable critical point and their chemical meaning.

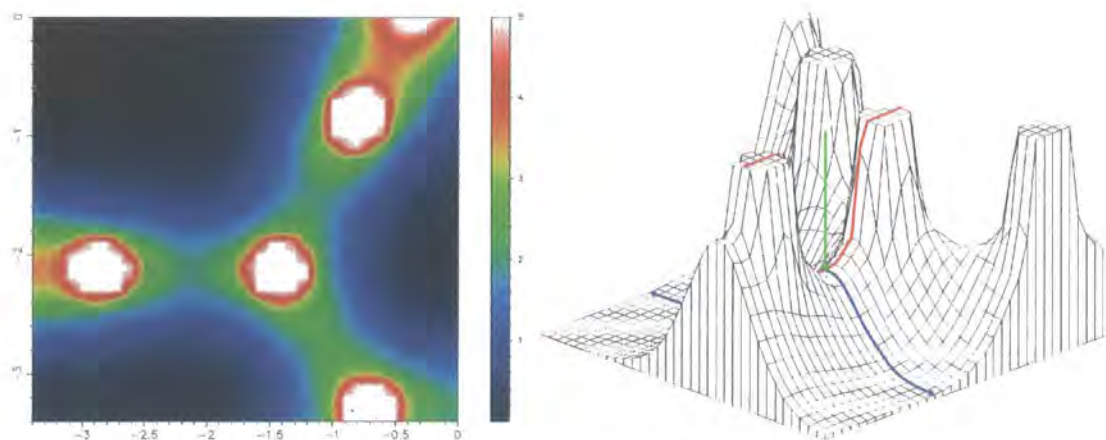


Figure 4.3.1: Plots of the charge density (ρ) displaying C-C and C=C bonds in the TCNQ molecule, showing a b.c.p at the intersection of the arrows; peaks in the maps indicating atomic positions; generated using Mapview¹⁷.

From the plots shown in Figure 4.3.1 it can clearly be seen that on travelling from one atom to the next along the bond (following the red arrow) the electron density passes through a local minima thus has a positive curvature. To traverse the bond the electron

density has a local maxima, be it either in the plane of the molecule (following the blue arrow), or perpendicular to that plane (following the green arrow), thus having a negative curvature. This gives all traditional bonds between atoms a critical point with a signature of -1, and since all of the curvatures are non zero a rank of 3, fully categorising the bond critical point as (3, -1).

Much of the early interpretation of experimentally determined charge densities revolved around the *deformation density* function. The deformation density is constructed by subtracting the promolecule density ($\rho^{\text{pro}}(r)$) from the experimentally determined electron density ($\rho^{\text{obs}}(r)$). This serves two general purposes. The chemically interesting electron density has features that are swamped in the total density by the much higher atom centred density, thus removing the large atomic peaks i.e. $\rho^{\text{pro}}(r)$, these interesting features can be seen. Figure 4.3.2 shows a deformation density map where the bonding density can be easily identified; even the greater density associated with the $\text{C} \equiv \text{N}$ triple bonds is observable.

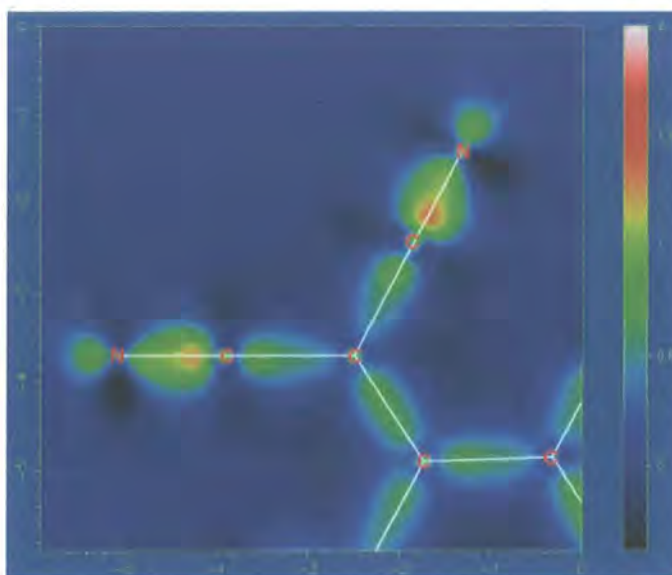


Figure 4.3.2: Deformation density plot through the mean plane of the cyano-groups of a TCNQ molecule.

The Laplacian is another important function of the electron density it is defined in Equation 4.3.1

$$\nabla^2 \rho(r) = \partial^2 \rho(r) / \partial x^2 + \partial^2 \rho(r) / \partial y^2 + \partial^2 \rho(r) / \partial z^2$$

Equation 4.3.1 The Laplacian of the electron density.

The Laplacian has some features that underpin its great functionality for classifications in topological analyses. One very important feature is that the Laplacian is invariant under rotation of the coordinate system, which allows direct comparison of features where the local coordinate systems are not coincident.

A fundamental use of the Laplacian is the classification of the types of interactions in molecules. In general, regions of space where the Laplacian is negative, have a concentration of electronic charge, therefore a plot of the negative Laplacian $[-\nabla^2(\rho)]$ has maxima at regions of electron density accumulation and minima at regions of depletion. The value of the Laplacian at the bond critical point (bcp) also gives a strong indication to the type of interaction present. A positive value of the Laplacian at the bcp is indicative of closed shell interactions, classically ionic, whereas a negative value indicates a more covalent nature of the bond. This simple interpretation is not sufficient when heavier elements are present, however it is sufficient for majority of the material presented in this thesis.

Another feature of the negative Laplacian of ρ , is that the positions of atom electron lone pairs can be seen clearly, as shown in Figure 4.3.3. The lone pairs are so well pronounced owing to the sensitive nature of the Laplacian function.

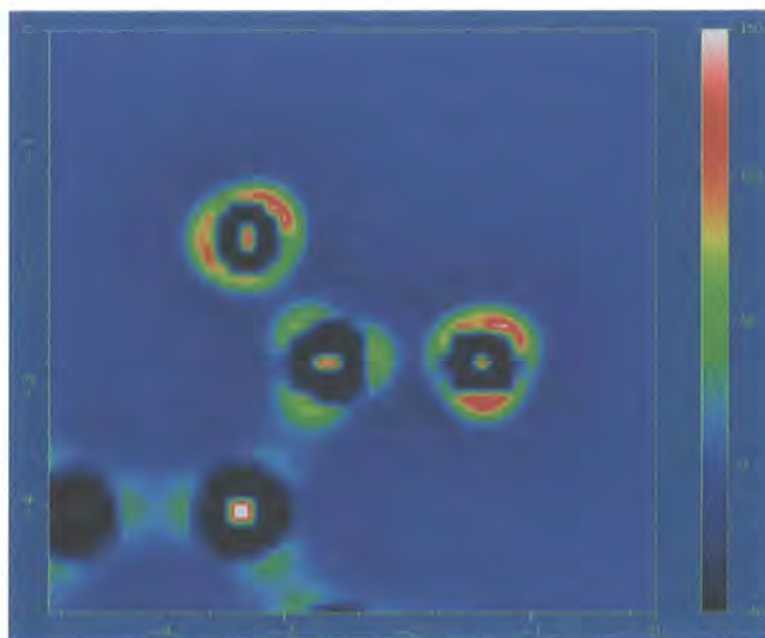


Figure 4.3.3: Negative Laplacian showing O electron lone pairs in the nitro group of NN-dimethyl-paranitro-aniline (NNDPNA, see section 5.5).

One other widely analysed function of the topology of the charge density, is the ellipticity of a given bond (ϵ). This is a measure of how far a bond deviates from the classical cylindrical shape which has an $\epsilon = 0$. Most notable is the deviation from cylindrical nature when π -bonding is present above and below the plane of the σ -bond, and then the return to cylindrical bonding for triple bonds.

AIM gives the possibility for the comparison of the results achieved from experimental charge density studies with purely quantum mechanical approaches to molecular calculations both in the crystal and in the isolated molecule. The evidence of molecular properties being enhanced in the crystalline state, especially the molecular dipole moment, can potentially be analysed though AIM but remains outside the main scope of this thesis.

For a full reference text on AIM, the reader is directed to “Atoms in Molecules A Quantum Theory” R. F. W. Bader¹⁶, the founding text for this subject.

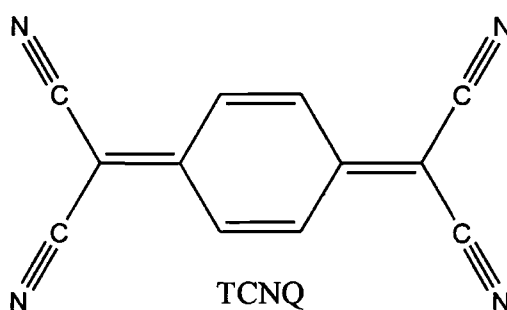
4.4 References

- 1 Hansen, N.K.; Coppens, P., *Acta Cryst.* **A34**, 1978, 909-921.
- 2 Koritzánszky, T.; Howard, S.; Mallinson, P.R.; Su, Z.; Richter, T.; Hansen, N.K., XD – A computer program package for multipole refinement and analysis of electron densities from diffraction data. User manual, Freie Universität Berlin, 1997.
- 3 Desiraju, G.R. and Steiner, T.S., *The Weak Hydrogen Bond In structural Chemistry and Biology*, page 7 (IUCr Oxford University Press).
- 4 Allen, F.H., *Acta Cryst.* **B42**, 1986, 515-522.
- 5 Craven, B.M.; Weber, H.P.; He, X. (1987). Technical Report TR-87-2. Department of Crystallography, University of Pittsburgh, PA 15620, USA.
- 6 Stewart, R.F.; Spackman, M.A.; Flensburg, C. (1998). *VALRAY98 Users Manual*. Carnegie Mello University, USA, and University of Copenhagen, Denmark.
- 7 Yufit, D.S. private communication, University of Durham 2004.
- 8 ASTRO, Data Collection Software, version 1.2; Bruker Analytical X-ray Instruments Inc.: Madison, Wisconsin.
- 9 Mallinson, P.R. (1995). '*Multipole Analysis of Experimental Charge Densities*', course notes from '*International School and workshop in Charge Density Analysis*' (La Plata, Argentina), p.9.
- 10 Domenicano, A. and Hargittai, I., '*Accurate Molecular Structures Their determination and importance*', page 240 (Oxford University Press).
- 11 XPREP – Reciprocal space exploration Version 6.12, Bruker Analytical X-ray instruments Inc.: Madison, Wisconsin
- 12 SAINT -NT, Data Reduction Software, version 5.0; Bruker Analytical X-ray Instruments Inc.: Madison, Wisconsin.
- 13 Probert, M.R.; Turner, M.J., unpublished work, University of Durham 2004.
- 14 Blessing, R.H., *Crystallogr. Rev.* **1**, 3-58, 1987.
- 15 G. M. Sheldrick, SADABS, Empirical Absorption Correction Program. University of Göttingen, Germany, 1998.
- 16 Bader, R.F.W. (1990). '*Atoms in Molecules: a Quantum Theory*', Oxford: Clarendon Press.
- 17 Farrugia, L.J., *J. Appl. Cryst.* 1999, **32**, 837-838.

Chapter 5

Charge Density Studies:

5.1 TCNQ (7,7,8,8-tetracyano-p-quinodimethane)



The initial background for this study stems from TCNQ's great importance in the field of molecular conductors, it being the first great electron acceptor molecule widely used in charge transfer salts. Indeed TCNQ mixed with TTF formed the 'first true organic metal' TTF-TCNQ [Ferraris *et al*¹]. There are charge density studies in the literature on the derivatives of this molecule², however TCNQ has not been studied more widely in its native form. The basic crystal structure of TCNQ has been known since 1962 [Melby *et al*³], showing that the molecule crystallises in the centrosymmetric space group C2/c. Pertinent crystallographic data are given in table 5.1.1.

a	8.8718(2)	N ^o of atoms* in asymmetric unit	8
b	6.9067(2)		
c	16.3977(4)	N ^o atoms on special positions	0
β	98.284(1)		
Z	4		

Table 5.1.1 – TCNQ crystallographic data at 120 K * non hydrogen atoms.

The above table shows the unit cell for this crystal structure is relatively small and the asymmetric unit is very small, containing only 8 independent non-hydrogen atoms, resulting in a system that should allow the recovery of the full experimental electron density using X-ray diffraction.

Crystals of quality suitable for charge density analysis by X-ray diffraction were provided by Dr A. S. Batsanov, to whom the author is very grateful; these crystals had previously been grown for machine calibration purposes. A relatively small ($0.2 \times 0.18 \times 0.12 \text{ mm}^3$), pale orange crystal was permanently mounted on a hair fibre prior to data collection on a SMART 6K diffractometer at 120 K. Preliminary data were taken to assess the quality of the crystal, analysing the frame data for any inconsistencies. Rocking curves of several reflections were analysed and it was decided that the 'standard' width (0.3°) of ω -scan for data collection was too wide, as these reflections were very sharp, suggesting a high quality crystal with low mosaicity. A final value of a 0.2° ω -scan was chosen for the data collection in this experiment. This value was chosen ensure $>80\%$ of reflections spanned more than one frame, a condition required for accurate integration of the data. Crystal faces were measured for use in absorption corrections and they are shown in Figure 5.1.1 and Table 5.1.2 below.



h	k	l	Dist.(mm)
0	0	1	0.060
0	0	-1	0.060
1	-1	0	0.090
-1	1	0	0.090
-1	1	2	0.085
-1	-1	-2	0.085
1	1	0	0.100
-1	-1	0	0.100
0	-1	1	0.100

Figure 5.1.1 and Table 5.1.2, the recorded crystal faces and their dimensions.

Owing to the increased number of parameters present in multipole refinements, data were collected to a higher 2θ angle than for 'standard' experiments and hence a large

portion of reciprocal space was sampled. The data collection parameters are outlined in Figure 5.1.2. The data collection strategy was analysed prior to data collection using the program ASTRO⁴ to determine the data coverage, including maximum resolution and mean redundancy of the data collection. Figure 5.1.2 shows the data were collected with two different detector positions (2-Theta) with two different exposure times. The different values of the detector position to allow higher resolution data to be measured. The different exposure times are necessary due to the atomic form factors for X-ray scattering i.e. scattered intensity decreases with increasing diffraction angle. Satisfactory counting statistics were obtained by increasing the exposure time at high angle to 3 times that at low angle hence increasing the signal to noise ratio significantly.

Run#	Frame#	2-Theta	Omega	Phi	Chi	Axis	Width	#Frames	Time
1	001	-30.00	-30.00	0.00	54.74	2	-0.200	900	10.00
2	001	-30.00	-30.00	90.00	54.74	2	-0.200	900	10.00
3	001	-30.00	-30.00	180.00	54.74	2	-0.200	900	10.00
4	001	-30.00	-30.00	270.00	54.74	2	-0.200	900	10.00
5	001	-30.00	-30.00	45.00	54.74	2	-0.200	900	10.00
6	001	-30.00	-30.00	135.00	54.74	2	-0.200	900	10.00
7	001	-30.00	-30.00	225.00	54.74	2	-0.200	900	10.00
8	001	-30.00	-30.00	315.00	54.74	2	-0.200	900	10.00
Run#	Frame#	2-Theta	Omega	Phi	Chi	Axis	Width	#Frames	Time
1	001	-70.00	-70.00	0.00	54.74	2	-0.200	900	30.00
2	001	-70.00	-70.00	60.00	54.74	2	-0.200	900	30.00
3	001	-70.00	-70.00	120.00	54.74	2	-0.200	900	30.00
4	001	-70.00	-70.00	180.00	54.74	2	-0.200	900	30.00
5	001	-70.00	-70.00	240.00	54.74	2	-0.200	900	30.00
6	001	-70.00	-70.00	300.00	54.74	2	-0.200	900	30.00

Figure 5.1.2 Data collection strategy.

Data were then integrated using the standard SAINT⁵ software package. Special care was taken to minimise any systematic errors that could be introduced to the data at this time by careful monitoring of the integrated voxels, and analysis of the program's statistical output, making corrections to the integration as needed, for example changing integration volumes around reflections. This output gives detailed information on errors in the collected data/methodology of integration especially on the positions of predicted and observed reflections. Careful analysis of this output is important to not allow a propagation of errors from an inappropriate integration into the final models.

At this stage, as with many 'standard' structural analyses, data were corrected by the multi-scan method present in SADABS⁶, merged using XPREP⁷, then solved and refined in the SHELXTL⁸ program suite. Figure 5.1.3 shows the refined model resulting from a spherical atom treatment, only the asymmetric unit is labelled for clarity. Table 5.1.3 shows the crystallographic information for this refinement. It

should be noted that this refinement was conducted on the restricted low angle dataset only (60° 2- θ).

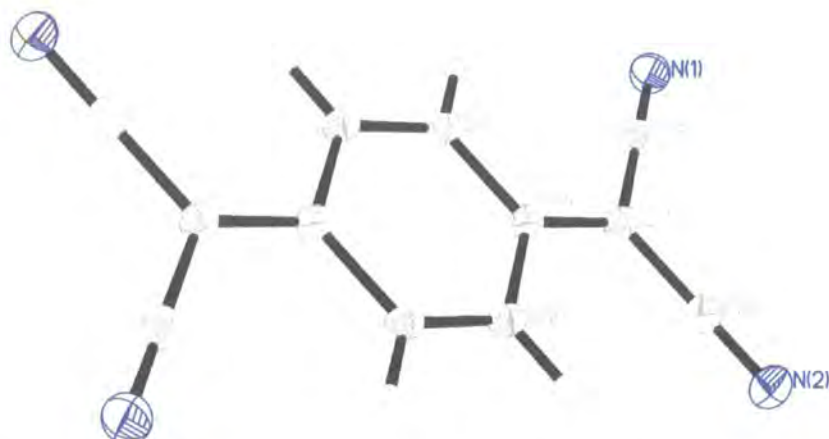


Figure 5.1.3 Thermal ellipsoid plot of TCNQ shown at 50% probability.

Formula	$C_{12}H_4N_4$
Space Group	C2/c
a (Å)	8.8718(2)
b (Å)	6.9067(2)
c (Å)	16.3977(4)
β°	98.284(1)
Volume (Å ³)	994.28(4)
Z	4
Ratio max/min transmission	0.888
μ mm ⁻¹	0.09
R _{INT}	0.0251
R ₁ ($F_o > 4\sigma F_o$)	0.0468
R ₁ (all)	0.0522
R _w	0.1345
GoF	1.065
Max residual (eÅ ⁻³)	0.99
Min residual (eÅ ⁻³)	-0.24
Number reflections observed/unique/($F_o > 4\sigma F_o$)	44630/2109/1872
Number of parameters	73

Table 5.1.3 Spherical atom refinement data at 120 K.

After spherical refinement the structure would normally be prepared for publication, however this model is taken as the starting point for multipolar refinement. The treatment of all data must first be managed, and as this work will show, the method that should be taken is unclear at the outset and gives no guarantee as to the desired results. Throughout this work multiple approaches to the data treatment have been made and the final results presented herein are from the ‘best’ refinements i.e. those resultant in the lowest residuals and maintaining both chemical and physical sense.

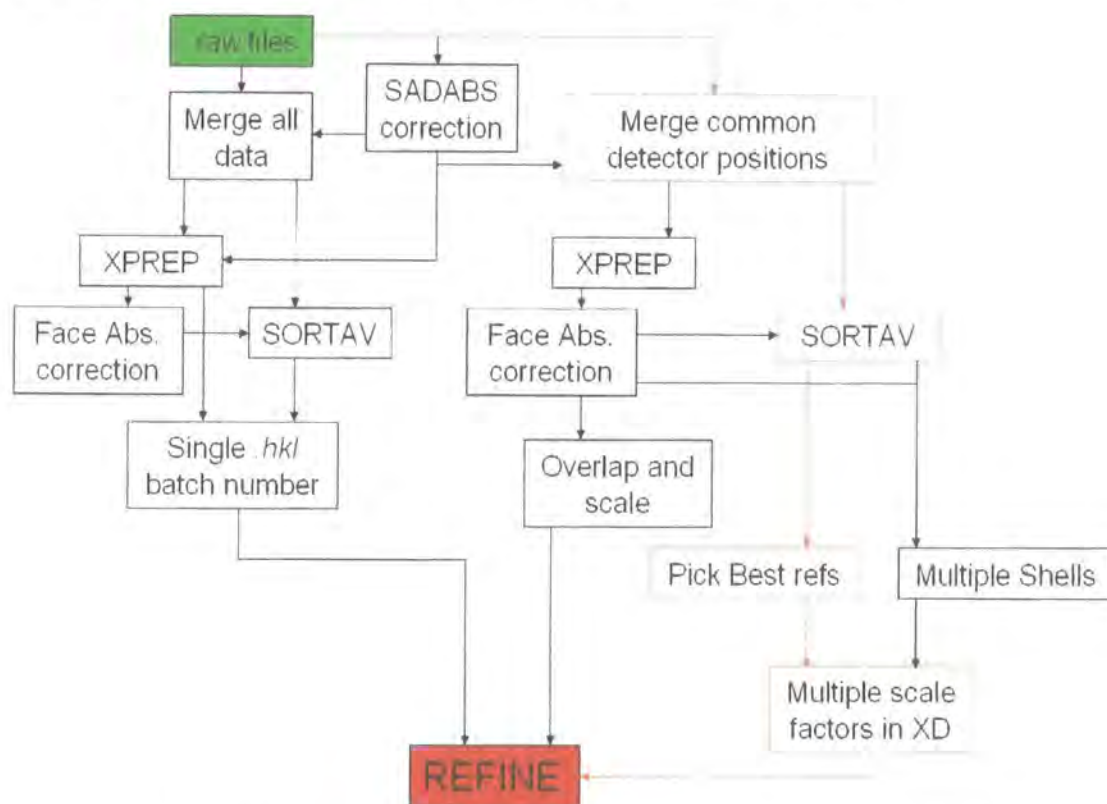


Figure 5.1.4 Flow chart from .raw files to .hkl file for refinement.

Figure 5.1.4 shows a scheme of some possible routes to a final .hkl file, but it does not cover every option and assumes that the initial integration of the frame data has been performed correctly. The route highlighted in orange was the one that was used in the multipole expansion of the TCNQ model. The data were integrated then input into SORTAV⁹ as .raw files in two separate batches – for the low and high angle data (the two positions of the detector, and hence exposure times). SORTAV was used to refine scale factors between each run in the low and high angle batches, to correct for non uniformities of common reflections as well as applying a spherical absorption correction and removing statistical outliers before merging the data, to provide a single entry for

each *hkl*. This process generates 2 final *.hkl* files one for the low and high angle setting respectively. From these two merged *.hkl* files the ‘best reflections’ were chosen, the criteria for selection was based on the ratio of F_{obs} to σF_{obs} . Each reflection selected was assigned a batch number relating to the file from which it was chosen. These batches of reflections were then refined with different scale factors in XD. The merging process described is not a rigorous statistical approach but has proven to give more satisfactory refinements, for the data presented in this thesis, than other approaches. It is believed that a method to merge all of the data collected into one *.hkl* file is possible, however at the time of writing the programs written for this task performed poorly.

The refined SHELXTL spherical atom model is used as a starting point for the multipolar expansion, with a few minor adjustments. The first and most notable in this case is that the H atoms are extended away from the atom they are bound to. The ideal case would be to have neutron data taken at the same temperature to locate and refine the hydrogen atom positions and their U_{ij} matrices. When such data are unavailable, as in the cases presented in this work, the hydrogen atoms are moved along the bond vector to standard ‘neutron normalised’ distances. This is a well known error in the ‘standard’ X-ray model. The hydrogen atoms are also contracted by setting the κ' and κ'' values to the Stewart Davison Simpson¹⁰ (SDS) value of 1.16.

When compared to programs such as SHELXTL, the XD¹¹ refinement package is in some ways far more flexible. XD does not fully understand symmetry or special position constraints. For example if an atom is located at an inversion centre then by symmetry the dipole expansion is necessarily zero as this function is anti-symmetric with respect to inversion. XD is not programmed to restrict such an expansion so the user must not attempt to refine those parameters –this does not just affect multipoles but atomic positions and elements in the U_{ij} matrix.

The structure of TCNQ contains no atoms on special positions, making the refinement relatively straight forward. After the spherical model has been input into XD and the local coordinate systems entered, scale factor refinements are completed with all other parameters fixed. Multipole refinements increase the complexity of the model as recommended in the literature^{11b} and also allow charge transfer in the molecule. Multipoles are included to the hexadecapole level for atoms involved in triple bonds and



to the octupole level for all other non H atoms. H atoms were refined only to the dipole level and then only bond directed dipoles were included. Additionally an electro-neutrality constraint was imposed, as with all charge density refinements presented in this work.

All atom characteristics were closely analysed throughout the refinement to maintain physically sensible values, in particular the difference mean square displacement amplitudes (DMSDA) were monitored to ensure the atoms all conformed to the Hirshfeld rigid bond test¹². Hydrogen atom positions were not refined due to the unavailability of neutron data.

The final residual electron density map for TCNQ is shown in Figure 5.1.5, this residual map is constructed using all data ($F_o > 3\sigma F_o$) i.e. no 2θ cut off present, and contours are marked on at the $0.05 \text{ e}\text{\AA}^{-3}$ level. Red contours represent positive residual density, blue negative and the black dotted contours are zero.

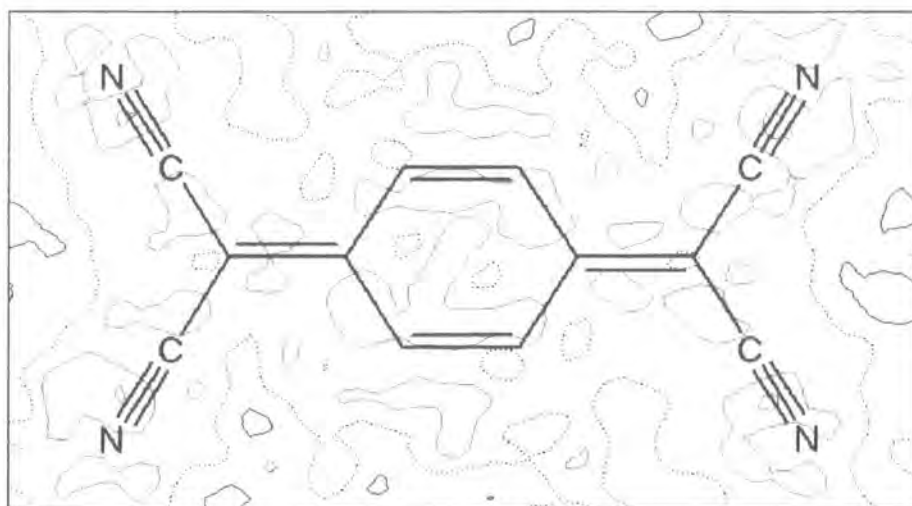


Figure 5.1.5: Residual electron density after multipole refinement.

The map can be described as flat and featureless, a strong indication of a successful multipolar refinement. The multipole expansion has successfully modelled all of the bonding density and represents a model which fits the experimental data very well, suggesting it is an accurate description of the electronic state of the molecule in the crystal. The bonding density is shown in the static deformation density map, Figure 5.1.6 below.

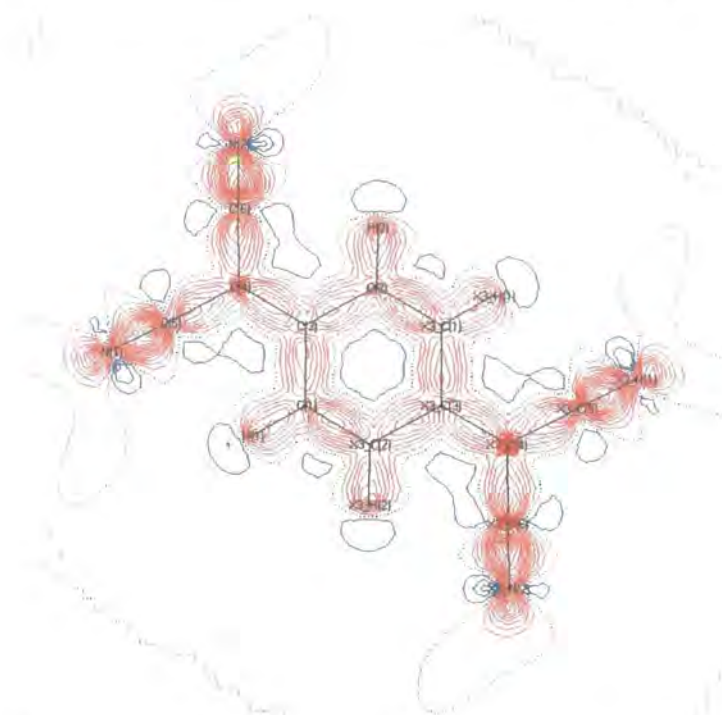


Figure 5.1.6: Static deformation density map for TCNQ.

All expected bond critical points, as defined by Bader's AIM¹³, were located and are shown in the bond path diagram, Figure 5.1.7. Table 5.1.4 shows the bcp's and the respective values of the electron density, the Laplacian and the ellipticity of the bond at its critical point. The appropriate (3, +1) ring critical point was also located.

Bond	Length (Å)	ρ (eÅ ⁻³)	$\nabla^2\rho$ (eÅ ⁻⁵)	ϵ
N(1)-C(5)	1.1575(5)	3.604(26)	-41.519(193)	0.02
N(2)-C(6)	1.1578(5)	3.690(26)	-44.814(174)	0.05
C(5)-C(4)	1.4254(4)	2.018(15)	-15.765(53)	0.08
C(6)-C(4)	1.4249(4)	2.022(15)	-16.403(51)	0.14
C(4)-C(3)	1.3805(4)	2.234(13)	-19.380(34)	0.27
C(3)-C(2)	1.4450(4)	1.995(11)	-15.753(27)	0.13
C(3)-C(1)	1.4442(4)	1.968(11)	-14.958(27)	0.16
C(2)-X3_C(1)	1.3564(4)	2.395(24)	-23.064(54)	0.26
C(1)-H(1)	-	1.865(20)	-18.918(71)	0.07
C(2)-H(2)	-	1.878(20)	-18.335(63)	0.08

X3 = symmetry operation x, +y, z

Table 5.1.4 Bond lengths and values of the electron density (ρ), the Laplacian ($\nabla^2\rho$) and the ellipticity of the bond at the bond critical points.

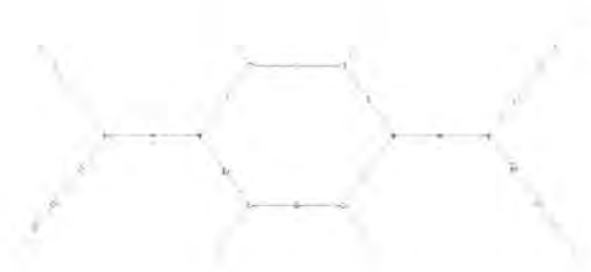


Figure 5.1.7: Bond path diagram for TCNQ.

The bond path diagram confirms the well known chemical connectivity of TCNQ and it is another indication of a successful refinement. The bond lengths and ellipticities of the bonds show that the classical description of the molecule, with alternating double and single bonds, is not entirely accurate. There is a clear distinction between the formally double and single bonds, however the single bonds appear to contain at least a small amount of π -bonding as they have ϵ values greater than zero. All C – C bonds are shorter than would be expected for single bonds and the formally C = C bonds are slightly longer than expected. The low ϵ values for the C-N triple bonds is due to the presence of π -bonding both above and below the σ -bond and to either side, resulting in a cylindrical bond.

TCNQ proved an excellent example case for understanding some of the challenges encountered in XD – charge density refinements. The availability of high quality crystals and hence data aided the learning experience, and resulted in high quality results. These results demonstrate the excellent recreation of molecular electron density from high quality X-ray diffraction data. Although TCNQ does not feature in the electron density literature in its pure form, this study now provides a good knowledge base for comparisons with either co-crystals or modified TCNQ. A summary of the final refinement parameters are given below in Table 5.1.5. Full crystallographic tables can be found in Appendix D.

$R_1 (F_o > 3\sigma F_o)$	0.0244
R_1 (all)	0.0540
R_w	0.0214
GoF	1.7751
Max residual ($e\text{\AA}^{-3}$)	0.119
Min residual ($e\text{\AA}^{-3}$)	-0.100
Number reflections observed/unique/($F_o > 3\sigma F_o$)	103971/5879/4124
Number of parameters	265
$R_1^* (F_o > 4\sigma F_o)$	0.0468
R_1^* (all)	0.0522
R_w^*	0.1345
GoF*	1.065

Table 5.1.5: Final agreement factors for multipole refined TCNQ structure at 120 K.

*Values from the spherical atom refinement for comparison, full details are found in

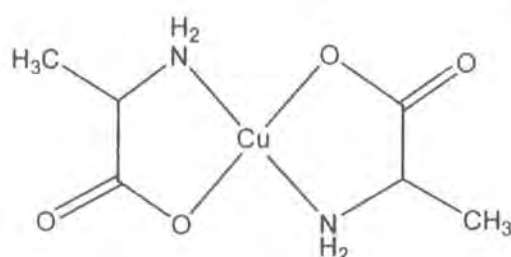
Table 5.1.3.

5.2 Probing the magnetic exchange interactions in some copper complexes

The study of exchange-coupled molecular systems has been a multidisciplinary field of continuous interest during the past few years. Major efforts have been directed to the study of systems where the magnetic interactions are transmitted through short chemical paths, which made possible the design of molecular systems with predictable magnetic properties. Among these systems, there is a significant interest in Cu(II) complexes of amino acids because they are the simplest model systems available to improve our knowledge of the metal-protein interaction in naturally occurring copper metalloproteins. This relative simplicity makes these systems accessible to a fairly complete study by solid state techniques. Furthermore, many of them exhibit interesting low-dimensional magnetic behaviour which has been studied by EPR, magnetic susceptibility and specific heat measurements.

Previous work¹⁴ on the analysis of the experimental electron density of a nitronyl nitroxide radical, showed promising results on the possibility of obtaining meaningful information about magnetic interactions through high resolution X-ray diffraction data. The structure of *Bis(D,L-alaninato)copper(II) Hydrate* was first reported by Calvo et al.¹⁵, including a discussion on the possible pathways for super-exchange interactions between the copper atom's centres. This provides a challenging experimental problem in trying to confirm these interaction pathways, though one which should be possible with the availability of high quality X-ray diffraction data exposed to multipolar electron density refinement. There is also a chance to extend this study to other copper dipeptides, on which some previous work has already been completed Facchin *et al.*^{16,17} and create a class of information relating to these species

5.2.1 Bis(*D,L*-alaninato)copper(II) Hydrate (*Cu-d-ALA-d-ALA*)



Cu-d-ALA-d-ALA

Calvo *et al.* reported this structure at room temperature, it was thought that by cooling to 110 K and recording high quality X-ray diffraction data that the proposals for the superexchange interaction (communication between sites) might be shown through a bond path between the metal sites, a charge density analysis of *bis(D,L-alaninato)copper(II) hydrate* was conducted. Data were collected at 110 K to a resolution of 0.41 Å using a Bruker SMART 1K-CCD diffractometer by Dr A.E. Goeta (University of Durham) who presented the author with the relevant integrated *.raw* files for this structure.

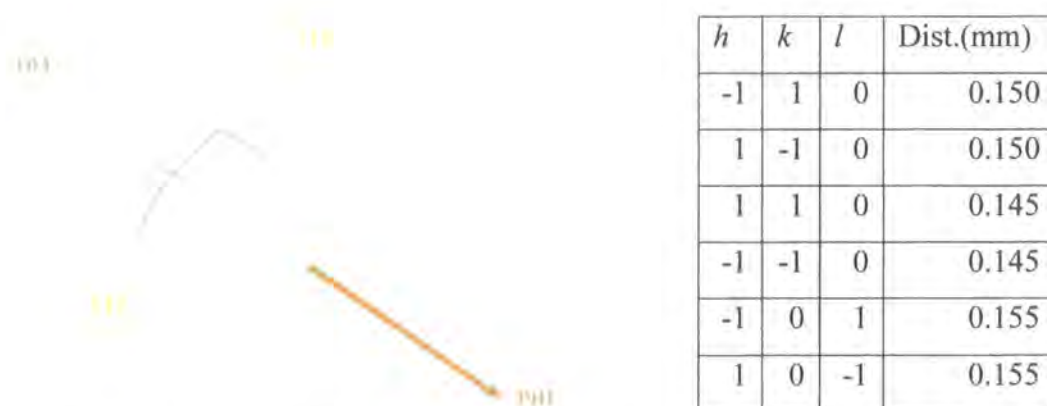


Figure 5.2.1 and Table 5.2.1, the crystal faces measured.

Given the isotropic nature of the crystal used, a face absorption correction was not applied. Instead a multi-scan correction and additional spherical absorption correction were applied using the program SADABS. The crystal transmission factors are listed along with all other final crystal data in table 5.2.2.

An initial model was found using the SHELXTL suite of refinement programs, figures 5.2.2, and 5.2.3 being taken from that refinement. Clavo *et al* reported a fully ordered

structure at room temperature, however the resultant model determined from our data at 110 K presented a slightly disordered configuration of the ligand, at the -CH and -CH₃ positions being above and below the plane of the rest of the alanine derivative, the major component being 87% occupied. The disorder has been removed from the figures for clarity. Figures 5.2.2 and 5.2.3 show the intermolecular interactions proposed by Calvo *et al*¹⁵ between the water molecule and the copper entity. The molecules form a chain with the copper atoms running through the crystal, with the water molecule adopting a tetrahedral configuration in which the oxygen atom's lone pairs would be pointing at the copper sites to produce an elongated octahedral environment at the copper centre.

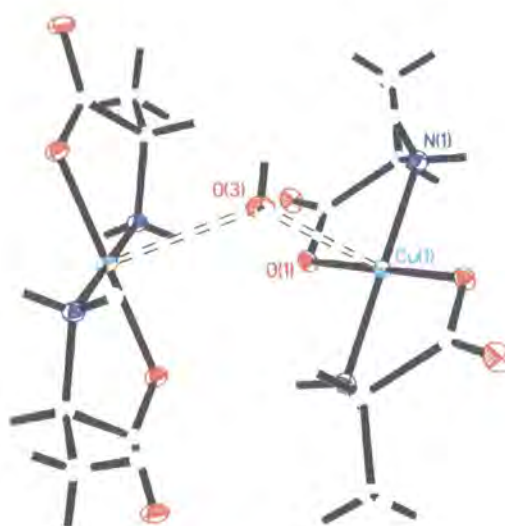


Figure 5.2.2: Thermal ellipsoid plot of Bis(D,L-alaninato)copper(II) Hydrate shown at 50% probability, showing possible coordination with water, disorder removed for clarity.



Figure 5.2.3: Copper and oxygen atoms forming chains through the structure.

Bis(D,L-alaninato)copper(II) has a relatively simple structural conformation, the copper(II) ion adopting an elongated octahedral configuration. Crystallographically the model is simplified further as the copper atom is positioned on an inversion centre, the origin of the unit cell. The asymmetric unit is completed by half a water molecule, the

oxygen of which is positioned on a 2-fold rotation axis. The number of parameters is relatively small for the starting model making the system well suited to a full charge density analysis from high resolution X-ray diffraction data, though the disorder found in the structure caused minor complications. The presence of disorder was such a concern that attempts were made by the author to recollect the data from a different crystal – though it quickly became apparent that the disorder was present in all of the crystals studied. Finally the original data collected by Dr A.E. Goeta were subjected to a full charge density analysis. The data were, as stated, treated for absorption and other corrections by SADABS then all data were merged in the program SORTAV, resulting in an *.hkl* file with only one scale factor.

The restrictions on the spherical harmonics allowed in the multipole refinement for atoms on special positions, are those that have the same symmetry as the site on which they are placed, having their principle axis in the direction of the symmetry element. The copper atom was, for example, restricted from any multipolar expansion that is anti-symmetric with respect to inversion i.e. all dipoles and all octupoles. The oxygen atom of the water molecule must have expansion terms that only contain 2-fold rotation symmetry such as the bond directed dipole. A 2-fold rotation axis also imposes the constraint that the off diagonal terms of the U_{ij} matrix must be equal to zero i.e. the U_{12} and U_{23} . It must also be noted that XD permits atoms on special positions to move away from them, therefore the position of the copper atom was fixed and only the *y* - coordinate of the oxygen in the water molecule was refined.

The charge density refinement in XD was initiated from the results of the SHELX refinement. Separate Kappa parameters were used for different atom types, and those of the same type in significantly different environments. Multipole refinement was carried out to the hexadecapole level for all non-hydrogen, non-disordered atoms. The disordered non-hydrogen atoms were refined to the octupole level with an additional constraint that the monopoles, for the major and minor species, were always kept at the refined ratio of the disorder from the spherical atom refinement in SHELXTL. Also the disordered sections were treated as rigid bodies. These constraints were to try and maintain chemical sense in the disordered section, and though the multipole populations of this region might not be physically meaningful, they will allow charge redistribution for the atoms. This approach was chosen, as the disordered region is distant from the

area of special interest lying between the water molecule and the copper centre. Since the structure is centrosymmetric the effect on the overall structure should be minimal, I do not believe this approach would be acceptable for a non centrosymmetric case – and in such a situation, where disorder and heavy elements are present, a charge density refinement may be futile.

Kappa (κ') parameter refinement was possible for all non hydrogen atoms and additionally the κ'' parameters were refined separately for the non-vanishing multipoles for the copper atom. Hydrogen atom κ' values were constrained to the Stewart Davidson Simpson¹⁰ (SDS) value.

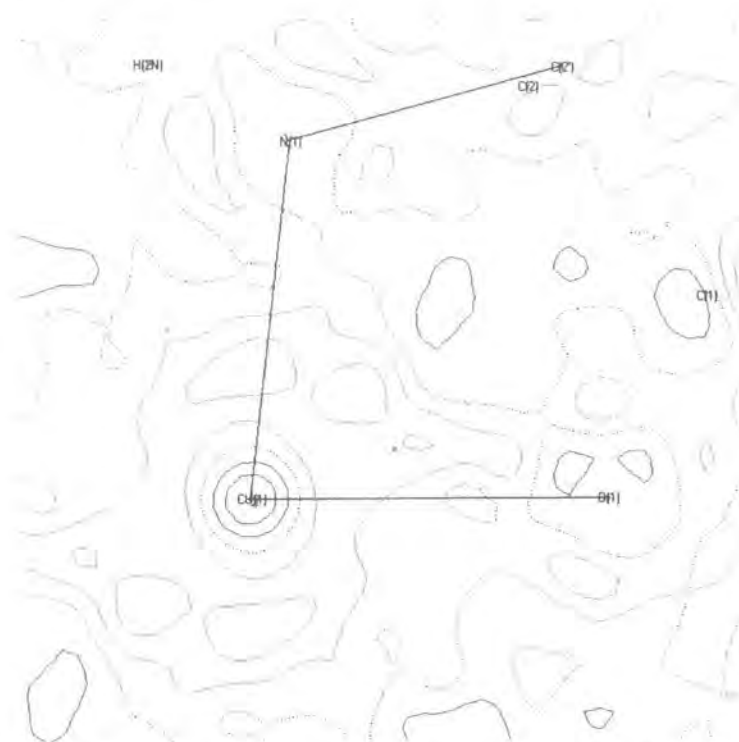


Figure 5.2.4: Residual electron density in the copper – ligand plane after multipole refinement.

The residual density, shown in Figure 5.2.4, was calculated using all data ($F_o > 3\sigma F_o$) and is drawn at the $0.1 \text{ e}\text{\AA}^{-3}$ contour level. Positive contours are once again red, negative blue and zero dotted. The residual electron density is generally flat for a compound containing a metal, showing good agreement between the multipolar model and the experimental data confirming the refinement results. The most probable cause for the residual density around the copper atom is from series termination errors in the

Fourier transformation. Residual density around the lighter atoms is much lower and comparable to other residual maps presented, from other studies. No further improvements on this residual density were found by using different refinement strategies on these data. Figure 5.2.5 shows the static deformation density through the plane of the carboxylate group from the alanine ligand, where the lone pairs of the oxygen atom being donated into the bond with the copper centre can be seen clearly.

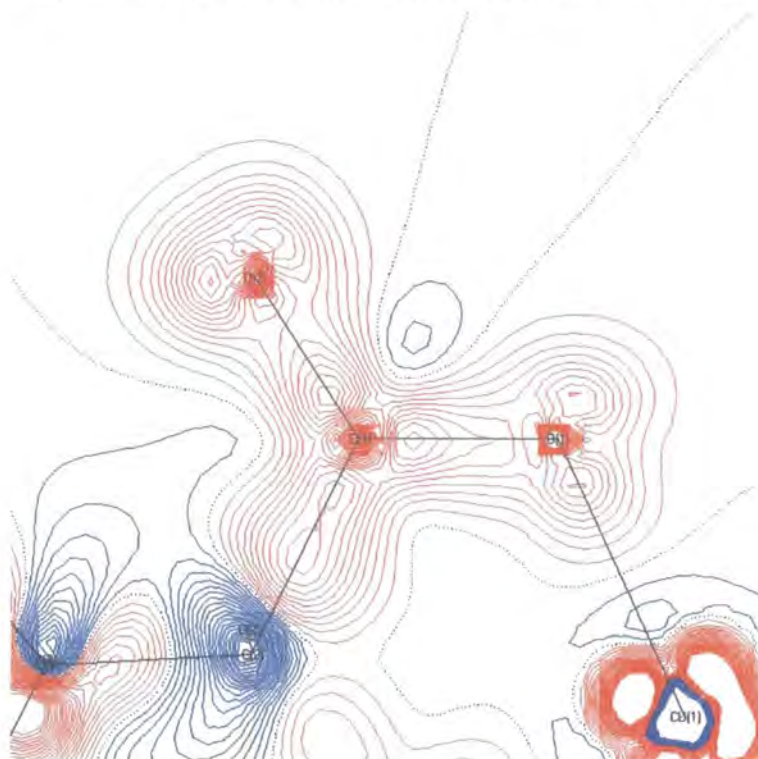


Figure 5.2.5: Static deformation density map through the carboxylate group.

Calvo *et al.* proposed that the communication between the copper centres is through the water molecule, and if this is the case a bond critical point should be found somewhere near the vector between the two atoms. This is indeed the case, the bond critical points have been located and the bond paths are shown in Figure 5.2.6 along with the static deformation density plotted through the plane of the water molecule.

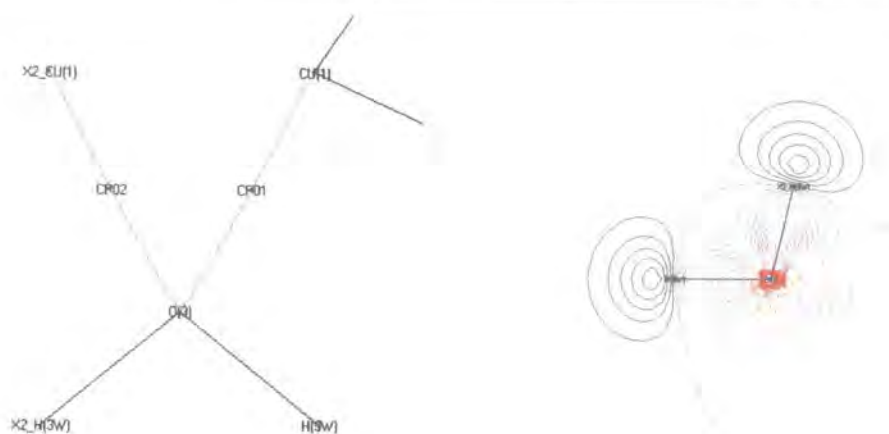


Figure 5.2.6: Bond path from O (water) to copper centre and static deformation density map through the plane of the water molecule.

I believe these results have shown that the molecular interactions in this compound can be mapped out using this high resolution crystallographic method, and that the water molecules do indeed play an important role in the physical properties of this material. These results confirm the proposals of Calvo *et al.* and show great promise for further studies. Furthermore with careful consideration, meaningful results may be obtained from moderately disordered materials, as has been shown in this case. Final agreement factors for the refinement are shown in Table 5.2.2.

Formula	$\text{Cu}(\text{NH}_2\text{CHCH}_3\text{CO}_2)_2 \cdot \text{H}_2\text{O}$
Space Group	C2/c
a (Å)	12.0490(3)
b (Å)	9.5649(2)
c (Å)	8.8803(2)
β°	110.775(1)
Z	4
Volume (Å ³)	956.89(4)
Ratio max/min transmission	0.830
$\mu \text{ mm}^{-1}$	2.28
$R_1 (F_o > 3\sigma F_o)$	0.0125
R_1 (all)	0.0296
R_w	0.0144

GoF	0.6916
Max residual ($e\text{\AA}^{-3}$)	0.270
Min residual ($e\text{\AA}^{-3}$)	-0.302
Number reflections observed/unique/($F_o > 3\sigma F_o$)	66550/6363/4959
Number of parameters	296

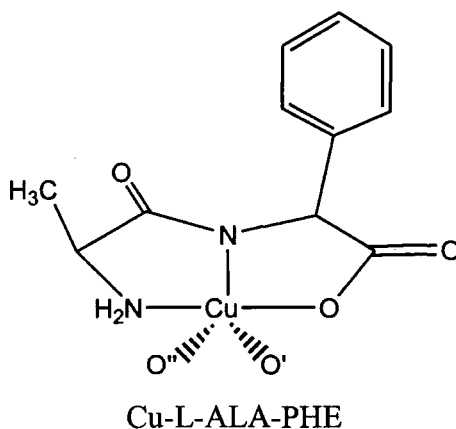
Table 5.2.2 Final crystal data for Bis(D,L-alaninato)copper(II) Hydrate at 120 K.

Bond	Length (\AA)	ρ ($e\text{\AA}^{-3}$)	$\nabla^2\rho$ ($e\text{\AA}^{-5}$)	ϵ
Cu(1)-O(1)	1.9602(3)	0.514(6)	12.231(9)	0.07
Cu(1)-N(1)	1.9877(3)	0.543(8)	10.861(14)	0.09
O(1)-C(1)	1.2772(4)	2.895(36)	-27.767(198)	0.10
O(2)-C(1)	1.2433(4)	3.105(37)	-31.560(212)	0.09
N(1)-H(1N)	-	1.725(39)	-29.786(232)	0.03
N(1)-H(2N)	-	1.947(42)	-26.744(213)	0.04
O(3)-H(3W)	-	1.865(41)	-32.294(241)	0.03
O(3)-X2_H(3W)	-	1.865(13)	-32.293(56)	0.03
Cu(1)-O(3)	2.6398(4)	0.108(0)	1.417(1)	0.09
O(3)-X2_Cu(1)	2.6398(4)	0.107(0)	1.403(1)	0.09

Table 5.2.3 Values at the bond critical points for the ordered section of the structure.

Full crystallographic tables can be found in Appendix D

5.3 Cu – L-alanine-L-phenylalanine (Cu-L-ALA-PHE)



A second system chosen in this study of copper compounds was the complex with the dipeptide L-ALA-PHE, the structure of which had previously been reported in 2000 by Facchin *et al*¹⁶. The previous work had been carried out at room temperature and showed that the crystal had a small asymmetric unit, as previously discussed this is a benefit to charge density structures. The paper also reports the experimental preparation of the sample which was followed to obtain high quality blue plate like crystals. A room temperature structural determination was conducted to evaluate the quality of the crystals and confirmed the structure reported in the literature (crystal data can found in Table 5.3.1). The high quality of the room temperature data collected suggested that the crystal was suitable for charge density analysis, especially given the promising results from the previous study of Bis(D,L-alaninato)copper(II). Although there are a greater number of parameters to refine for this compound, the lack of disorder was thought to simplify this case. The crystal was therefore permanently mounted for a charge density experiment. On cooling snapshots of the crystal diffraction pattern were taken to analyse the crystal for any adverse cooling effects – crystals can often crack and twinning on cooling can occur. The first of these ‘snapshots’ showed that the diffraction pattern had changed significantly – with a far greater number of reflections appearing on the image. This image was taken 50 K below room temperature. The cooling was stopped and a unit cell determination attempted. The resultant unit cell showed an increase in the *b*-axis. Measurement of inter reflection vectors gave an axis of approximately 30 Å and the correct cell was obtained by increasing the number of vectors used in the indexing routine to give a cell with the *b*-axis now 27 Å. The crystal was then warmed to room temperature and the diffraction obtained was not as high

quality as the first collections therefore another crystal was mounted. This crystal was cooled more slowly and the diffraction pattern analysed closely. The transition was again observed occurring at 280(2) K. Data were collected at 250 K to be confident of a complete transition; crystal data above and below the transition are found in Table 5.3.1.

	Room temp 290(2) K	250(2) K
Empirical formula	CuC ₁₂ H ₁₄ N ₂ O ₃	
Crystal system and space group	Orthorhombic / P2 ₁ 2 ₁ 2 ₁	
Crystal dimensions (mm ³)	0.24 x 0.14 x 0.07	
a (Å)	5.4105 (7)	5.4003 (9)
b (Å)	9.0646 (10)	27.2190 (44)
c (Å)	26.2663 (33)	25.5729 (45)
Volume (Å ³)	1288.2(3)	3759.0(11)
Z	4	12
μ (mm ⁻¹)	1.70	1.74
Radiation Mo Kα λ (Å)	0.71073	
R _{int}	0.0323	0.0652
Final R ₁ F _o > 4sig(F _o)	0.0311	0.1104
Final wR ₂	0.0893	0.2596
GoF	0.716	1.142
Number reflections observed/unique/(F _o >4σF _o)	16159/4549/4108	44454/13029/10703
Number of parameters	163	490

Table 5.3.1: Crystal data for Cu-ALA-PHE above and below phase transition.

The table shows that the data recorded above the transition gave significantly better refinement statistics than that recorded below it, the transition obviously causes a certain amount of internal strain on the crystal. Two images of the diffraction pattern are shown in Figure 5.3.1, these images were taken with the crystal in exactly the same orientation just above and below the phase transition. The increase in the unit cell size can clearly be seen from the increased number of reflections and the way in which it affects the unit cell size can also be approximated from where the additional reflections occur. Further cooling showed no further crystallographic change, only a slight degradation in the data quality. Attempts to trap the room temperature structure below

the phase transition by flash freezing failed – though the reason becomes apparent when the structures are analysed.

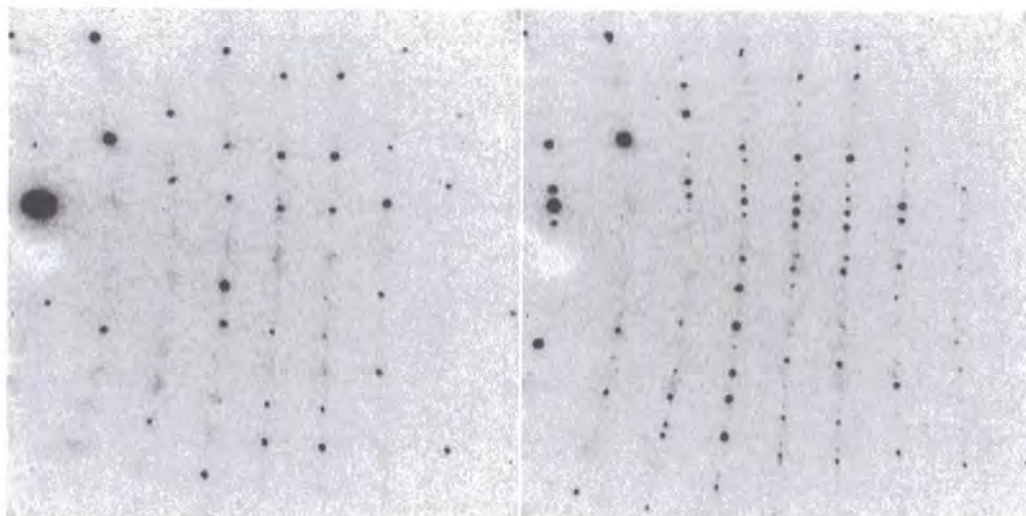


Figure 5.3.1: Images above (left) and below (right) the phase transition, images generated using *FRM2FRM*¹⁸.

The phase transition coupled with the reduction in data quality limited the analysis, and a full charge density analysis on this compound was not attempted, though ‘standard’ refinements were performed to try and understand the phase transition more completely. Crystal structure solution and refinements were carried out in the SHELXTL software package, and corrections were applied to the data using the multi-scan technique in SADABS. There is no indication in the statistics of a space group change from $P2_12_12_1$. The thermal ellipsoids of the independent atoms in each structure are shown in Figures 5.3.2 and 5.3.3 (atoms bound by dotted lines are symmetry equivalents of present atoms – showing the 1st coordination sphere of the copper atoms).

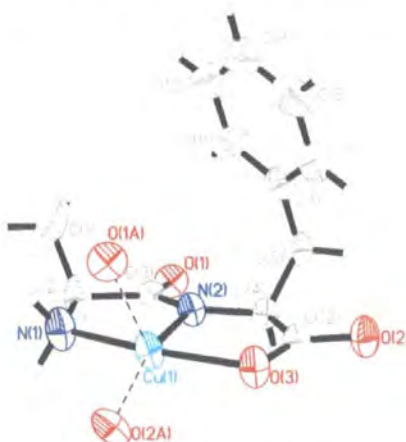


Figure 5.3.2: Thermal ellipsoid plot, shown at 50%, of room temperature structure.

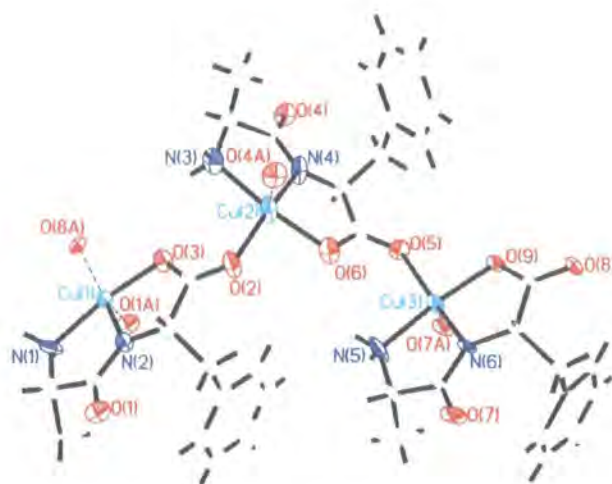


Figure 5.3.3: Thermal ellipsoid plot, shown at 50 %, of the 250K structure.

These figures clearly show the increase in the number of parameters when passing through the phase transition, but unfortunately do not clearly show any change in the structure. The copper ‘units’, the asymmetric unit at room temperature, appear to match exactly the structure below the phase transition, implying the structural change is relatively small. The deviation of the structure away from that at room temperature is so small it requires the independent ‘units’ to be overlaid in exactly the same orientation. This is a useful feature present in the XP visualisation program, any subset of atoms may be selected and their coordinates orthogonalised, then any number of these may be overlaid by defining common atoms to calculate the transformation matrix to bring all orthogonal coordinates into the same orientation. The results of this are shown in Figure 5.3.4 below, in which the pink backbone shows the three independent units below the phase transition and the green dashed backbone is the room temperature structure. It can clearly be seen from this figure that the deviation is indeed very small, one unit almost perfectly matches the room temperature structure and the other two units have minor torsional changes of the ‘arms’ of the ligand with respect to the plane of the copper bound atoms.

The changes in this structure appear to stem from very minor effects and demonstrate how the structure lies in a very shallow energy minimum. The conformational changes appear to be due to nothing more than a thermal contraction of the unit cell – shortening some of the bonds present in the structure, which in turn forces these small shifts. The

changes are abrupt and occur within a small temperature range of approximately 2-3 K suggesting this is regarded as a 1st order transition.

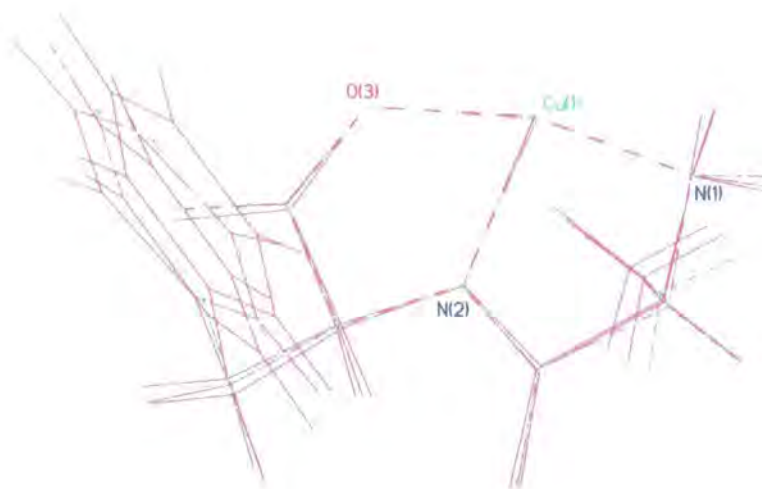
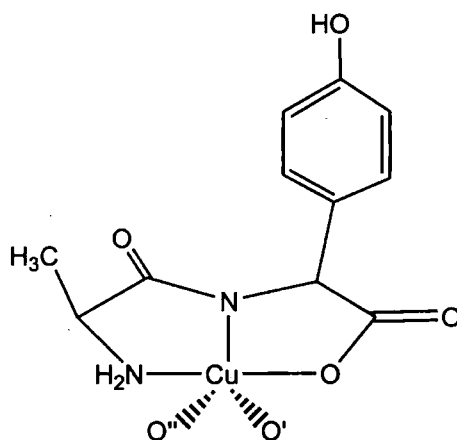


Figure 5.3.4: Trace of overlay of the three independent centres at 250 K (pink) and the room temperature framework (dashed green).

It is worth noting how dramatic an effect a small structural change may have on the diffraction pattern of the crystal, once again confirming the powerful nature of X-ray crystallography as an analytical tool.

Although a charge density study of this compound was unfortunately not possible, a novel phase change has been recorded and analysed, full structural details including bond lengths and angles can be found in Appendix D.

5.4 Cu – L-alanine-L-tyrosine

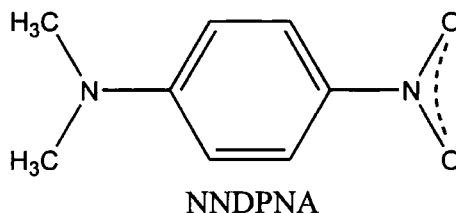


Cu – L-ALA-L-TYR

After the unexpected nature of the structural parameters of Cu-ALA-PHE, another crystallisation was attempted for the above compound, again following the method of Facchin *et al*¹⁶. Although a reaction was observed in solution and the identifying deep blue colour of an aqueous Cu(II) complex could be seen, attempts to crystallise this solution failed, and this analysis was subsequently stopped at a very early stage.

This final failure saw the termination of the study of these compounds at this time, although it has uncovered some interesting structural features and shown the power of the techniques.

5.5 NNDPNA (*N,N*-dimethyl-*para*-nitro-aniline)



This study was embarked upon in collaboration with Mr M.J. Turner (University of Durham) who is studying molecules with potential non-linear optical responses. The reason for the charge density analysis was to calculate the dipole enhancement of the molecule in the solid state compared to the gas phase. MJT has conducted preliminary calculations on the gas phase structure as a comparison point for this analysis, Borbulevych *et al*¹⁹ have also performed calculations on NNDPNA and these results are also compared. The crystals were grown by slow evaporation from an ethanol solution (MJT) and the author claims no credit for this or the calculations performed in the gas phase.

Data were collected on a Bruker SMART 6K diffractometer at 120 K affording very high diffraction quality to a resolution of 0.44 Å. Preliminary scans showed the reflections were very sharp, and therefore the scan width was reduced to allow accurate data collection and integration. The final result was a 0.1° ω -scan which allowed >80% of the reflections to cover more than one frame. Integration was performed using the SAINT software package and absorption corrections made by the multi-scan method in SADABS. Merging data from the two different detector settings was conducted independently and then the 'best' reflections were chosen from these two merged files, using the method described previously in section 5.1. This is equivalent to the method used for the TCNQ refinement. Crystallographic data can be found in Table 5.5.1 below.

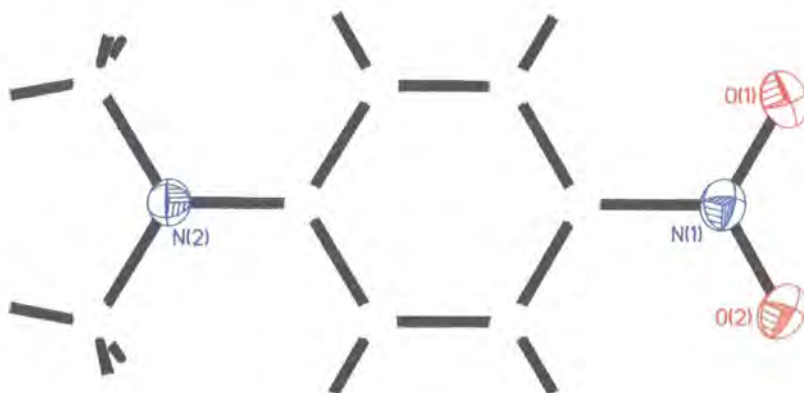


Figure 5.5.1: Thermal ellipsoid plot of NNDPNA at 120 K with atomic labelling.

The preliminary structure solution and refinement were performed in the SHELXTL suite, a plot of the molecule showing the thermal ellipsoids at 50 % is shown in Figure 5.5.1.

Empirical formula	$C_8H_{10}N_2O_2$
Crystal system and space group	Monoclinic / $P2_1$
Crystal dimensions (mm^3)	0.20 x 0.10 x 0.08
a (\AA)	3.8872(1)
b (\AA)	10.4997(3)
c (\AA)	9.6190(3)
β ($^\circ$)	90.019(1)
Volume (\AA^3)	392.59 (2)
Z	2
μ (mm^{-1})	0.10
Radiation (\AA) Mo K α λ (\AA)	0.71073
Number of unique refs	4380
R_{int}	0.0178
Final R_1 $F_o > 4\text{sig}(F_o)$	0.0311
Final wR_2	0.0903
GoF	1.055
Number reflections observed/unique/ $(F_o > 4\sigma F_o)$	27493/4594/4022
Number of parameters	330

Table 5.5.1: Crystallographic data for NNDPNA at 120 K.

The β angle is very close to 90° tempting belief that the system is orthorhombic, but the monoclinic cell is the true setting and this confirms the structures previously published by Mak *et al.*²⁰ at an undisclosed temperature, but presumably room temperature and by Borbulevych *et al.* at 110 K.

The necessary non-centrosymmetric symmetry for non-linear optical materials does increase the difficulty in the charge density refinement as the dependence of the structure on the calculated phases is so important – indeed it has been suggested in the literature that the retrieval of a true experimental electron density, from X-ray diffraction experiments, for non centrosymmetric structures is ‘impossible’²¹. This has been shown experimentally not to be the case²² and a number of electron density analyses of structures in non-centrosymmetric space groups have been published.

No atoms in NNDPNA are located on special positions however there is one restriction that the refinement program XD requires to be input. Whereas programs such as XL in the SHELXTL package are able to automatically fix the origin in space groups where necessary, XD is not capable of doing this, therefore in the charge density refinement of NNDPNA the y-ordinate of one of the atoms is not refined, this inhibits the structure from moving randomly along the 2_1 axis, on which the origin of the space group $P2_1$ is positioned.

To aid the initial refinement H-atom monopole populations were decreased to 0.9, effectively giving the H-atoms a +0.1 charge, this charge was transferred onto the atom to which they are bonded. This was then fixed until later in the refinement when other multipole parameters were closer to their true values. The approach was chosen as the initial refinements were not particularly stable and it was always the correlation between the H-monopole parameter and its U_{iso} value that destabilised the least squares routine. All non hydrogen atoms were refined to the octupole level, with no restrictions. Kappa parameters were all kept fixed at their initial values, the parameters being too unstable in this system to be refined and not providing any improvement in refinement results when refinements were attempted. The final residual electron density map is plotted through the plane of the molecule in Figure 5.5.2. All data were used to generate this plot.

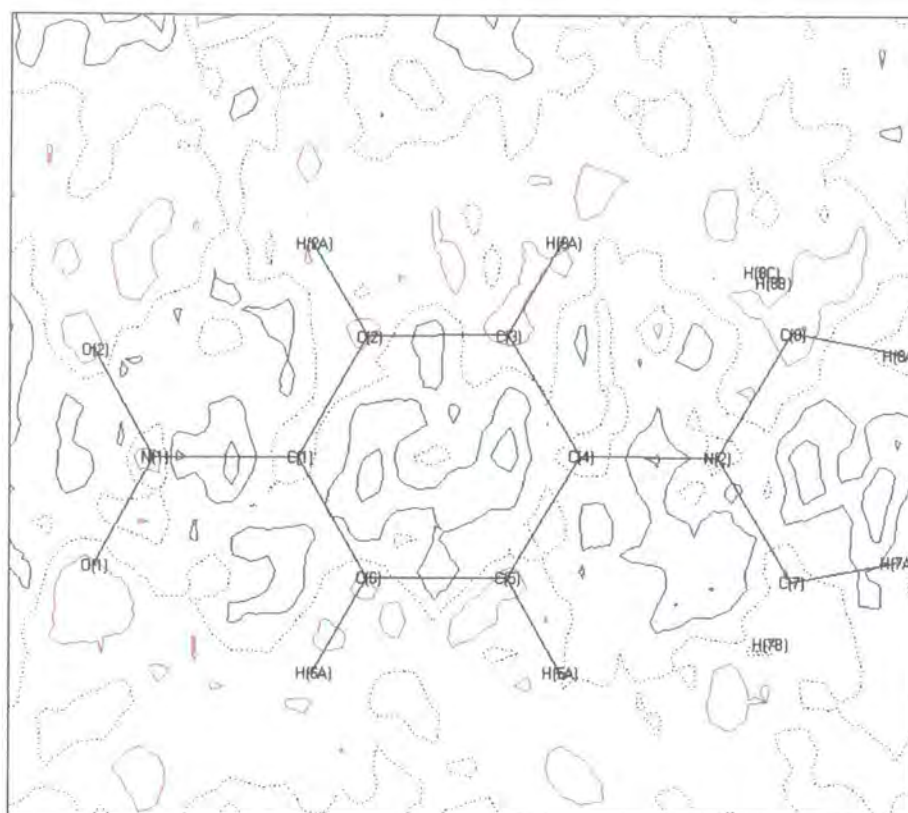


Figure 5.5.2: Residual electron density for NNDPNA, contours at $0.05 eA^3$ positive contours are red, negative blue and black dotted zero.

The map shows no residual features and given the low contour levels shows a very flat surface, adding confidence to the refinement and indicating that the multipole parameters have successfully accounted for the valence/bonding density of the atoms. Further confidence is found when analysing the static deformation density map, shown in Figure 5.5.3 below, in which all the bonding features are apparent and even the oxygen electron lone pairs are clearly seen.

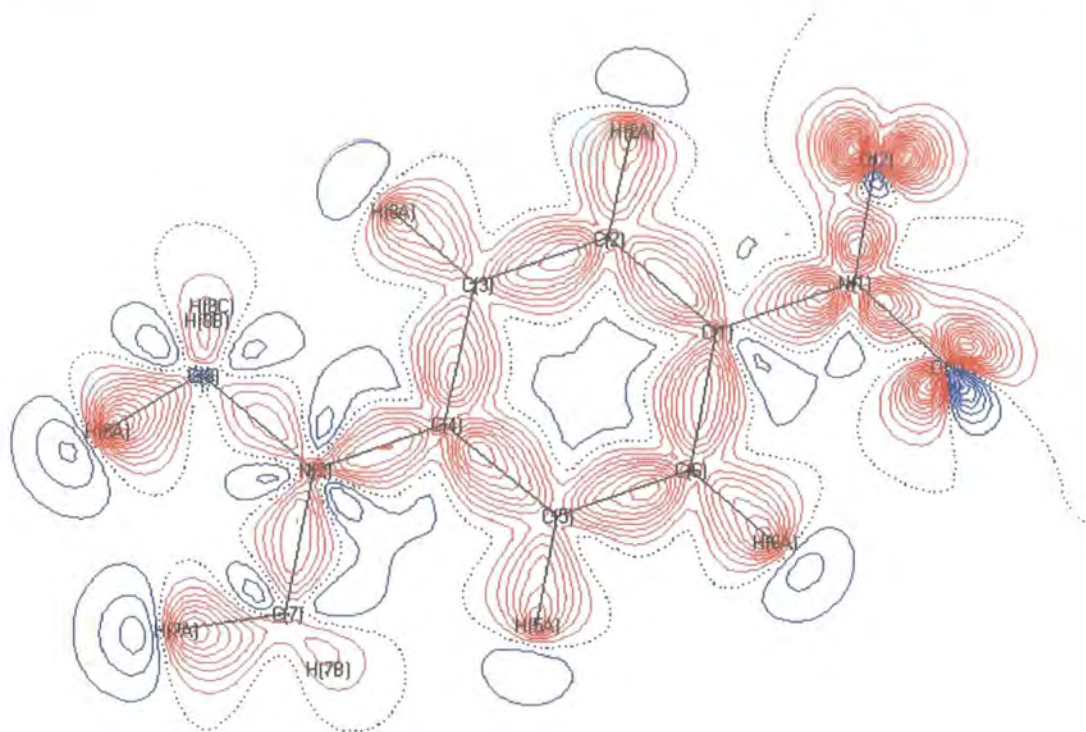


Figure 5.5.3: Deformation density for NNDPNA, contours at 0.1 eA^3 (red positive, blue negative and dotted zero).

The feature seen in the oxygen electron lone pair region is even more clearly seen in the Laplacian of the electron density, shown in Figure 5.5.4, taken through the plane of the nitro group. Features such as lone pairs appear as positive lobes in the Laplacian.

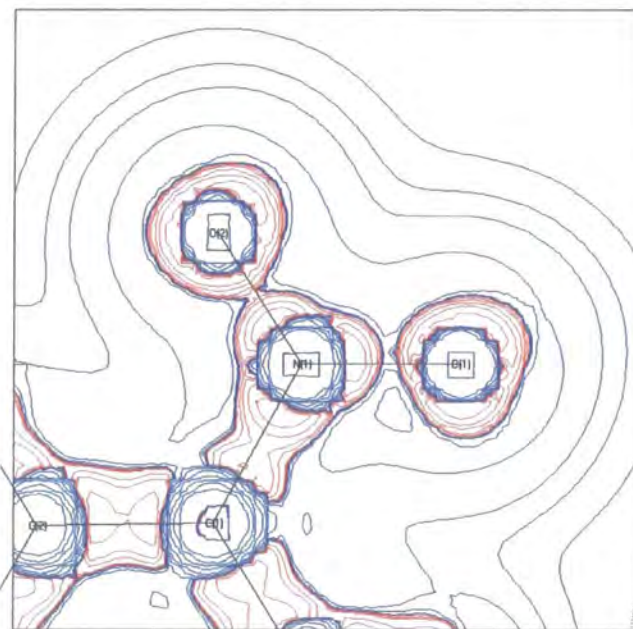


Figure 5.5.4: Negative Laplacian of nitro group, for NNDPNA, showing lone pairs on O atoms.

The calculated dipole of the molecule, from the multipole refinement is 12.3 D compared to the theoretically calculated one in the free molecule of 8.57 D (MJT, private communication 2003). This increase is exactly what this study was hoping to prove. It can be suggested that the lone pairs of the oxygen atoms interact with the H-atoms of the next molecule in the unit cell (translation of $1+x, y, 1+z$) but no bond critical point was found along this path, though this distance is relatively large approximately 2.67 Å. It can therefore be classed as a weak electrostatic (closed shell) interaction. All of the molecular bond critical points and bond paths were found, and are shown in Figure 5.5.5, and the critical values for them are found in Table 5.5.2.

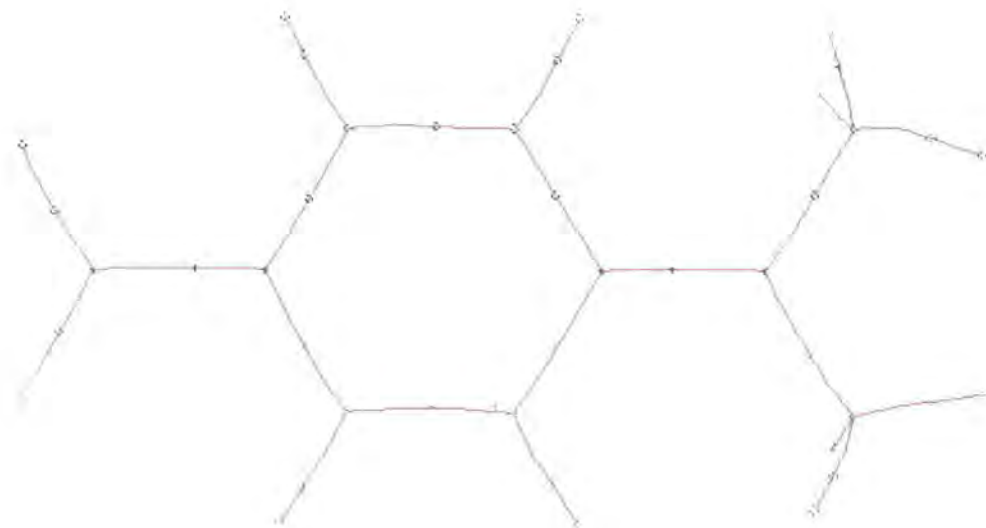


Figure 5.5.5: Bond path diagram for NNDPNA.

Full crystallographic details can be found in Appendix D. The dipole enhancement in the solid state, and the fact that it can be measured from high quality X-ray diffraction data show promising possibilities for the study of non linear optical materials by this method in the future.

Bond	Length (Å)	ρ (Å ⁻³)	$\nabla^2\rho$ (Å ⁻⁵)	ϵ
O(2)-N(1)	1.2354(9)	3.292(39)	-7.126(112)	0.06
O(1)-N(1)	1.2416(9)	3.312(39)	-3.209(115)	0.14
N(2)-C(4)	1.3556(5)	2.338(28)	-21.430(100)	0.24
N(2)-C(8)	1.4541(6)	1.791 (33)	-11.221(82)	0.14
N(2)-C(7)	1.4531(7)	2.007(30)	-12.151(72)	0.18
N(1)-C(1)	1.4343(6)	1.912(26)	-15.602(97)	0.32
C(4)-C(3)	1.4210(5)	2.048(28)	-17.244(63)	0.18
C(4)-C(5)	1.4211(5)	2.169(26)	-18.343(64)	0.19
C(1)-C(2)	1.3950(5)	2.143(28)	-20.308(65)	0.22
C(1)-C(6)	1.3942(5)	2.249(28)	-21.414(63)	0.27
C(2)-C(3)	1.3816(5)	2.238(28)	-20.154(68)	0.20
C(6)-C(5)	1.3807(6)	2.318(27)	-22.618(71)	0.22

Table 5.5.2: Critical values at molecular bond critical points for NNDPNA.

The differences between the theoretical and experimental results extend beyond just the dipole enhancement. The published theoretical results of Borbulevych *et al.* show large differences in the bond ellipticities of the C – N bonds compared to the experimentally obtained values. These are formally double bonds, which is in gross agreement with the experimental values, but is in contradiction to the theoretical results, where the equivalent bond to the C4 – N2 presented here ($\epsilon = 0.24$, Table 5.5.2) has a calculated ellipticity of 0.02 signifying a single σ -bond. The experimental results also show a polarisation across the phenyl ring, with C – C bonds on the nitro end of the molecule possessing a greater ellipticity than at the di-methyl end. This polarisation is likely to represent the movement of the charge in the conjugated system, in line with the enhanced dipole moment. Both experimental and theoretical results lead to the conclusion that the formal, traditional, bonding description is inadequate, and that the real bonding description is far less rigidly defined into double and single bonds.

5.6 References

- 1 Ferraris, J.; Cowan, D.O.; Walatka, V.J.; Perlstein, J.H., *J. Am. Chem. Soc.*, 1973, **95**, 948-949.
- 2 Cole, J.M.; Copley, R.C.B.; McIntyre, G.J.; Howard, J.A.K.; Szablewski, M.; Cross, G.H., *Phys. Rev. B*, **65**, 125107.
- 3 Melby, L.R.; Harder, R.J.; Hertler, W.R.; Mahler, W.; Benson, R.E.; Mochel, W.E., *J. Am. Chem. Soc.*, 1962, **84**, 3374-3387.
- 4 ASTRO 5.007, Bruker Analytical X-ray Instruments Inc.: Madison, Wisconsin, 1997.
- 5 SAINT -NT, Data Reduction Software, version 6.45; Bruker Analytical X-ray Instruments Inc.: Madison, Wisconsin.
- 6 G. M. Sheldrick, SADABS, Empirical Absorption Correction Program. University of Göttingen, Germany, 1998.
- 7 XPREP – Reciprocal space exploration Version 6.12, Bruker Analytical X-ray Instruments Inc.: Madison, Wisconsin.
- 8 SHELXTL, version 5.1; Bruker Analytical X-ray Instruments Inc.: Madison, Wisconsin.
- 9 Blessing, R.H., *Crystallogr. Rev.* **1**, 3-58, 1987.
- 10 Stewart, R.F.; Davidson, E.R.; Simpson, W.T., *J. Chem. Phys.*, 1965, **42**, 3175-3187.
- 11 Koritsanszky, T.; Howard, S.T.; Richter, T.; Macchi, P.; Volkov, A.; Gatti, C.; Mallinson, P.R.; Farrugia, L.; Su, Z.; and Hansen, N.K. (2003). XD - a computer program package for multipole refinement and topological analysis of charge densities from diffraction data. ^bUser manual, Freie Universität Berlin, 1997.
- 12 Hirshfeld, F.L., *Acta Cryst.*, 1976, **A32**, 239-244.
- 13 Bader, R.F.W. (1990). *Atoms in Molecules: a Quantum Theory*. Oxford: Clarendon Press.
- 14 Pillet, S.; Souhassou, M.; Pontillon, Y.; Caneschi, A.; Gatteschi, D.; Lecomte, C., *New J. Chem.*, 2001, **25**, 131-143.
- 15 Calvo, R.; Levstein, P.R.; Castellano, E.E.; Fabiane, S.M., Piro, O.E.; Oseroff, S.B.; *Inorg. Chem.* 1991, **30**, 216-220.

- 16 Facchin, G.; Torre, M.H.; Kremer, E.; Piro, O.E.; Castellano, E.E.; Baran, E.J., *Z. Naturforsch.* 2000, **55b**, 1157-1162.
- 17 Facchin, G.; Torre, M.H.; Kremer, E.; Piro, O.E.; Castellano, E.E.; Baran, E.J., *J. Inorg. Biochem.*, 2002, **89**, 174-180.
- 18 FRaMe to FRaMe image file format conversion utility. Version 1.0.10
Copyright 1997-99 Bruker AXS.
- 19 Borbulevych, O.Y.; Clark, R.D.; Romero, A.; Tan, L.; Antipin, M.Y.; Nesterov, V.N.; Cardelino, B.H.; Moore, C.E.; Sanghadasa, M.; Timofeeva, T.V., *J. Mol. Struct.*, 2004, **604**, 73-86.
- 20 Mak, T.C.W.; Trotter, J., *Acta Cryst.*, 1965, **18**, 68.
- 21 El Haouzi, A.; Hansen, N.K.; Le Hénaff, C.; Protas, J., *Acta Cryst.*, 1996, **A52**, 291-301.
- 22 Spackman, M.A.; Byrom, P.G.; *Acta Cryst.*, 1997, **B53**, 553-564.

Chapter 6: Future research and development

6.1 The necessity for improvement in current X-ray diffraction instrumentation

The results presented herein show structural changes, albeit small, are still occurring in the organic molecular materials studied on cooling to the current laboratory experimental limits. A full structural understanding of molecular superconductors can not be completed until structural data can be retrieved above and below all the transition temperatures of the physical phenomena that these materials possess. The lowest temperature that can be achieved in the Durham laboratory, at the time of writing, is 10 K using the cryo-refrigerator mounted on the Fddd diffractometer. This temperature, although exceptional for most laboratories, is still insufficient to fully explore the structure analyses of the molecular conductors presented in this study, which have known electronic transitions below 8 K. To achieve the desired temperatures further investment in equipment is required. The current limit to commercially available refrigeration units, for use in laboratory X-ray diffraction, is ≈ 6 K, this is achieved through a modification of the displac currently in the Durham laboratory. 6 K is still above the desired base temperature and the only other alternative is to take samples to the large central facilities, where larger specialised equipment allows cooling to the *milli* Kelvin region. This is a costly and time consuming process as experiments have to go through rounds of proposals before any experimentation is completed. Another problem is that the majority of this specialised equipment is only available at neutron diffraction facilities, requiring crystals of sufficient size for neutron experiments which often is an impossible task. Scientists at the *Institute Laue Langevin* have developed a three stage displac incorporating an additional Joule-Thompson cooling stage. The lower limit for this device is 1.8 K. In principle there is no reason why this device could not be used for X-ray diffraction in the home laboratory, albeit with some modifications to current systems. This would allow larger temperature range to be explored without the need to go for the costly experiments at central facilities,

nonetheless this does require funding for the machine that is to be developed and constructed.

6.2 X-ray detection

As was seen in the 12 K determination of $\beta''\text{-(ET)}_4[(\text{H}_3\text{O})\text{Ga}(\text{C}_2\text{O}_4)_3]\text{PhNO}_2$, section 3.1, the data collection ultimately was restricted by the temperature variance of the cryo-cooler. The diffraction experiment was expansive in time since all of the data were collected sequentially using a single point detector. Although this method of X-ray detection has certain advantages, it requires equipment to maintain the same temperature within acceptable errors, for time lengths of up to 30 days. The advent of area detectors, and in particular CCD's, revolutionised laboratory X-ray crystallography, allowing datasets to be achieved in previously unimaginable times; e.g. 30 minute data collections are now possible. Any new machine designed now should take advantage of the CCD detectors, even though they have other drawbacks. The principal problem with area detectors is that by their very nature they 'collect' all of the diffracted intensities from a sample and its environment. With open flow cryo-systems this is of little significance, however when a closed-cycle system is used there is an abundance of X-ray scatter arising from beryllium walls of the sample chamber. An elegant solution to this problem was proposed by Coppens *et al*¹ in which a specialised beamstop is placed inside the sample chamber, and manipulated by an external magnet. This is shown schematically in Figure 6.1 and some test results, collected at University of Durham on a SMART 1K diffractometer, using a mock-up of this design, are shown in Figure 6.2, with no crystal present.

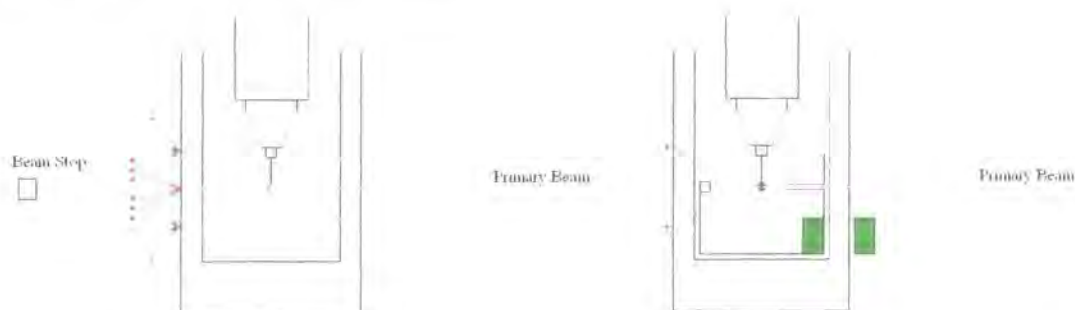


Figure 6.1: Schematic of beamstop placed inside the sample environment.

Conceptually this idea is exceptional, it effectively removes all the scatter from the Be cans that traditionally have comprised the walls of the sample chamber without interfering with the desired crystal diffraction. However the simplicity of the idea does not transfer to operation, with difficulties of alignment of this beamstop throughout an experiment.

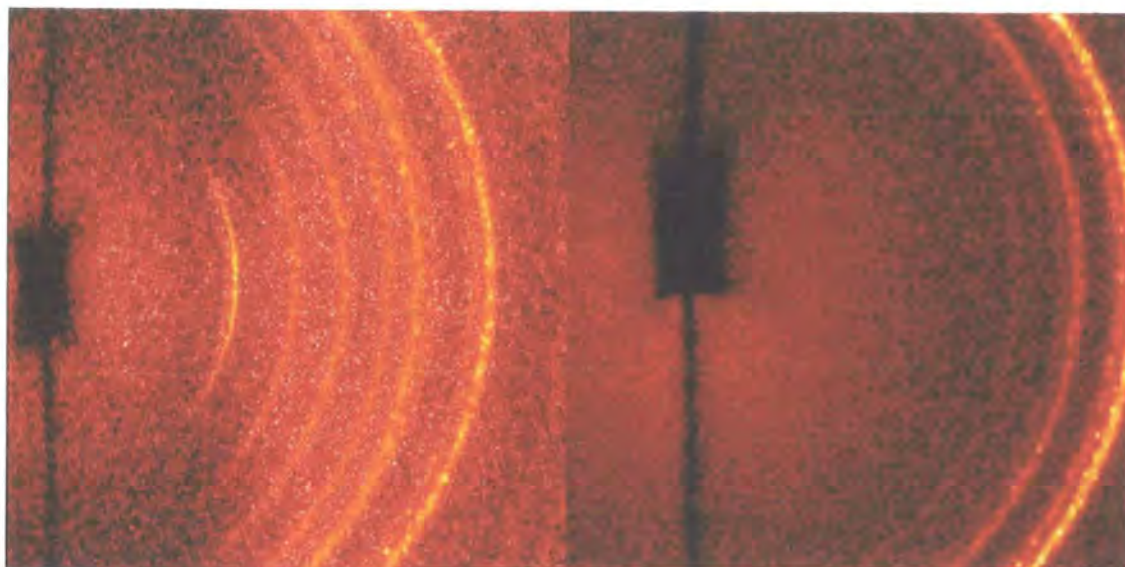


Figure 6.2: Test case of traditional beamstop (left) and beamstop inside Be can (right) collected on a SMART 1K diffractometer.

A different solution has been proposed with the advent of new materials, to construct the sample chamber of a material that is transparent to X-rays and gives only amorphous scatter. The compound of choice is KAPTON®² which provides no coherent scatter resulting in an even background for the detector. KAPTON® also has the advantage that visible light can pass through it so centring the crystal when it is at low temperatures is almost as simple as at room temperature. This transmission of light though could be a concern as incident light on the sample could induce some heating. Moreover the KAPTON® chamber cannot maintain as hard a vacuum as the traditional Be cans which could cause problems from the collection of condensed gasses in the sample chamber if the experiment continued for a long period of time. Kapton is also unproven technology when exposed to repeated heating and cooling situations where the material is placed under vacuum repeatedly.

Another potential solution is a new concept that I have developed, namely that of a 'software collimator', to be used in conjunction with the traditional Be cans. Collimation of the diffracted beam, to a single point detector, has been a traditional method of removing unwanted diffraction from the sample environment. The principle is that only scatter along a vector from the detector to the sample is allowed to be incident on the detector. The same approach could be used with an area detector, using precision engineering to construct a set of solid slits for a particular detector at a particular distance from the sample. This would inhibit the use of the machine quite considerably; it would also be an incredible engineering feat and would limit the active area of the detector. This is therefore not a favoured option.

I believe that this engineering accomplishment could also be achieved using a software approach. If diffraction data were collected at two different detector distances, keeping the same crystal orientation matrix, then the intensity associated with a specific diffraction angle could be calculated. If this was the same at both distances the diffraction is purely from the sample, this method should also allow the extrapolation of data that in one position is 'under' any Be scatter and in the second is not. Be scatter would have a constant calculated diffraction angle at the two different positions of the detector, i.e. the diffraction patterns of the sample and its environment would move across the detector at different rates as the distance from the sample to the detector was varied. Theoretically this should allow the complete deconvolution of data arising from the sample and that from the sample environment. Additionally there are certain 'magic distances' that data collections should be carried out at, to maximise the advantages of two data collections. These distances are the ones in which the largest area of reciprocal space is accessible, without contamination from the diffraction of the sample's environment. These distances for example could be due to the overlap of the primary reflections from the Be of the different walls of the sample chamber. These 'magic distances' can significantly increase the amount of data accessible in any single run. The combination of data deconvolution mixed with 'magic distances' is hoped to form the integral parts of a software collimator, allowing easy access to large complete areas of reciprocal space. This then allows the quality and completeness of data collected to be increased, compared to collecting data when Be scatter obscures large portions of reciprocal space. The aim of combining very low temperature X-ray diffraction data

collection with high redundancy and accuracy is made possible. The ideas of a software collimator and magic distances are summarised in Figure 6.3.

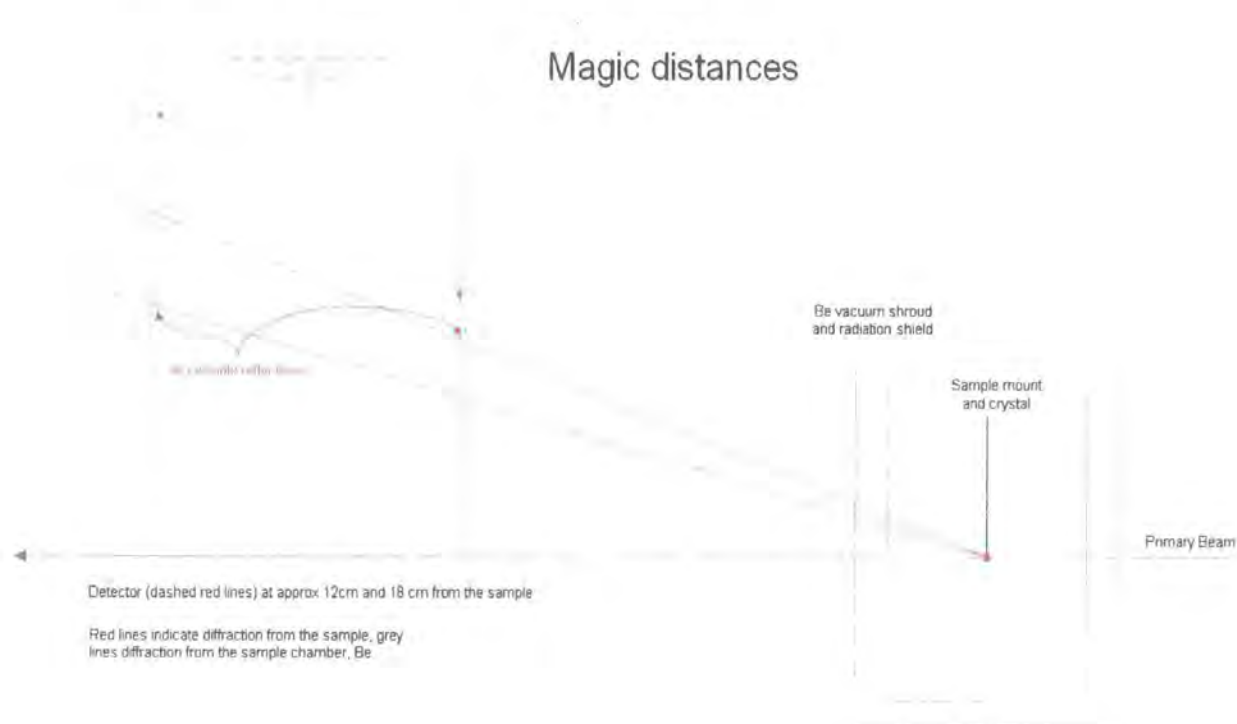


Figure 6.3: The concept of 'Magic Distances'.

6.3 A New diffractometer?

The ideal case would be to develop a completely new diffractometer specialized to perform ultra low, highly accurate diffraction experiments under a range of sample environments. The additional cooling is not only applicable to the field of molecular materials, but it would also assist with charge density data collections to aid the separation of thermal motion from the valence density.

This was seen as a necessary new piece of equipment to further an already very interesting field and as such a grant application was made to EPSRC for machine development. Durham has been awarded a fully funded five year project (2005-2010) to build such a unique, world leading, laboratory X-ray diffraction instrument.

- 1 Darovsky, A.; Bolotovskiy, R.; Coppens, P., *J. Appl. Cryst.*, 1994, **27**, 1039-1040.
- 2 Meserschmidt, M.; Meyer, M.; Luger, P., *J. Appl. Cryst.*, 2003, **36**, 1452-1454.

Appendix A: Seminars and courses attended.

Durham University Seminars

- 04/10/2001 Dr. Sylvia Capelli: Molecular Motion from Multi-Temperature ADPs
- 17/10/2001 Dr Peter Knowles: Gauss-Poisson density representations for large-scale electronic computation
- 24/10/2001 Prof. Bob Denning: Photonic Crystals
- 31/10/2001 Prof. Colin Raston: Towards benign supramolecular chemistry: synthesis - self organisation
- 08/11/2001 Dr. Sergei Kozhuskov: Selected Chapter of Political Organic Chemistry: Fascinating Artificial Cyclopropane Architectures
- 29/11/2001 Prof. Oscar Au-Alvarez: A Crystal's Wonderland - And a Little bit of Cuba!
- 05/12/2001 Prof. Mike Eaton: Drugs of the Future
- 06/12/2001 The Nuts and Bolts of First Principles Simulation – 13/12/2001
- 31/01/2002 Prof. Peter Day: Some Supermolecular Chemistry of Magnets and Superconductors
- 10/01/2002 U.K. Neutron and Muon Users Meeting – 11/01/2002
- 06/06/2002 Dr. Alexander Chernega: Design of New Organic Synthons for Crystal Engineering of functional Materials
- 13/06/2002 Dr. Garry McIntyre: Single Crystal Neutron Diffraction at the ILL: Science and Facilities
- 11/02/2003 Dr John Emsley, University of Cambridge
False Alarms: Chemistry & the Media
- 12/02/2003 Professor Paul Raithby, Department of Chemistry, University of Bath
Adventures in Organometallic Polymer Chemistry
- 22/10/2003 Professor Matthias Beller, Inst. für Organische Katalyseforschung an der Universität Rostock, Germany.
Homogeneous Catalysis a Key Technology for Environmentally Benign Synthesis of Fine Chemicals and Pharmaceuticals (The Degussa Lecture)
- 29/10/2003 Dr Roger Davey, Department of Chemical Engineering, UMIST
Nucleation from solutions - a stereochemical approach
- 05/11/2003 Dr Colin Bain, Physical & Theoretical Chemistry Laboratory, University of Oxford

-
- Pouring oil on troubled waters: wetting and phase transitions in oil drops on surfactant solutions
- 04/02/2004 Professor P O'Brien, Department of Chemistry, University of Manchester
Quantum Dots Realizing the Potential
- 18/02/2004 Professor J Waltho, Molecular Biology and Biotechnology, University of Sheffield
Protein folding and misfolding from an NMR perspective
- 25/02/2004 Professor Robin Clark - RSC Liversidge Lecture
Raman Microscopy: a Powerful Technique in Inorganic Chemistry and for Surface, Nanoparticulate and Pigment Studies
- 02/07/2004 Professor Sir Harry Kroto, Nobel Laureate in Chemistry (1996)
2010: a NanoSpace Odyssey.
- 01/12/2004 Dr Elspeth Garman, Laboratory of Molecular Biophysics, Oxford
Cool crystals: kill or cure?
- 25/01/2005 Professor Sir Harry Kroto, Nobel Laureate in Chemistry (1996)
Want to save the world? Better do chemistry.
- 26/01/2005 Professor Tim P. Softley, Physical and Theoretical Chemistry Laboratory, Oxford
Highly excited molecules in the study of photodissociation, surface scattering and ultracold chemistry
- 01/02/2005 Dr Dylan Jayatilaka, University of Western Australia
Wavefunctions Derived from Experiment
- 02/02/2005 Professor Ulrich Griesser, Department of Pharmaceutical Technology, University of Innsbruck
Crystal Polymorphism of Pharmaceuticals: Relevance and Analytical Aspects

External Meetings:

- 27/08/2001 Oxford School on Neutron Scattering - Mansfield College / Nuclear Physics Department, Oxford University.
- 14/11/2001 BCA, Autumn 2001: Mesomolecular Crystallography (Aston University, Birmingham).
- 25/03/2002 BCA Spring Meeting at The University of Nottingham.

- 06/08/2002 XIX Congress and General Assembly of the International Union of Crystallography. Geneva, Switzerland.
- 13/11/2002 BCA Autumn Meeting 2002 "Dealing with Difficult Data", Kings College, Strand, London.
- 05/01/2003 ISIS Neutron Training Course
- 07/04/2003 BCA/CCG Ninth Intensive Course in X-ray Structure Analysis.
- 15/04/2003 BCA Spring Meeting 2003 at The University of York
- 24/06/2003 The Third European Charge Density Meeting, ECDM-III, and The European Science Foundation Exploratory Workshop. Sandbjerg Estate, Denmark.
- 12/11/2003 BCA Autumn Meeting 2003 Beyond Refinement; What Happens Next?, Accelrys Ltd, 334 Cambridge Science Park, Cambridge.
- 06/04/2004 BCA Spring Meeting 2003 at The University of Manchester.

Appendix B: Publications List

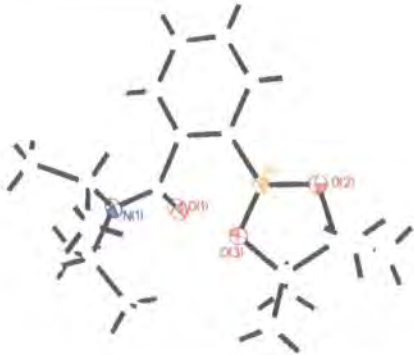
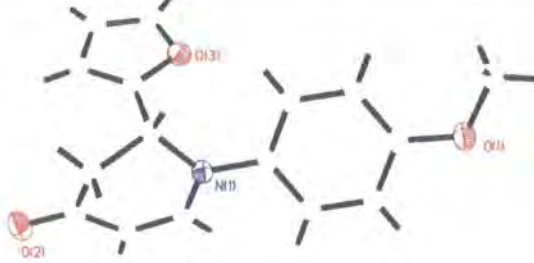

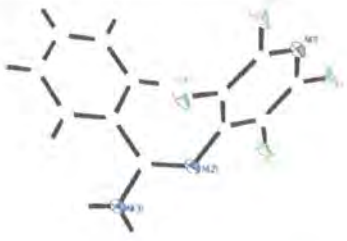
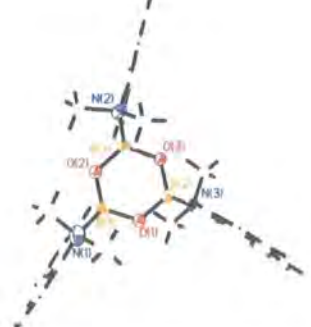
- 1 Akutsu, H.; Akutsu-Sato, A.; Turner, S.S.; Le Pevelen, D.; Day, P.; Laukhin, V.; Klehe, A-K.; Singleton, J.; Tocher, D.A.; Probert, M.R.; Howard, J.A.K., *J. Am. Chem. Soc.*, 2002, **124**, 12430.
- 2 Probert, M.R.; Akutsu, H.; Turner, S.S.; Day, P.; Howard, J.A.K., *Acta Cryst.*, 2002, **A58(supplement)**, C148.
- 3 Akutsu, H.; Akutsu-Sato, A.; Turner, S.S.; Day, P.; Tocher, D.A.; Probert, M.R.; Howard, J.A.K.; Le Pevelen, D.; Klehe, A-K.; Singleton, J.; Laukhin, V.N., *Syn. Metals* **137**, 2003, 1239-1240.
- 4 Giles, R.L.; Howard, J.A.K.; Patrick, L.G.F.; Probert, M.R.; Smith, G.E.; Whiting, A.; *J. Organomet. Chem.*, 2003, **680**, 257-262.
- 5 Hermitage, S.; Howard, J.A.K.; Jay, D.; Pritchard, R.G.; Probert, M.R.; Whiting, A., *Org. Biomol. Chem.*, 2004, **2**, 2451-2460.
- 6 Akutsu-Sato, A.; Akutsu, H.; Turner, S.S.; Day, P.; Probert, M.R.; Howard, J.A.K.; Akutagawa, T.; Takeda, S.; Nakamura, T.; Mori, T., *Angew. Chem. Int. Ed.* 2005, **44**, 292-295.
- 7 Probert, M.R.; Watkin, D.J.; Stewart, A.J.; Storer, R.; Fleet, G.W.J., *Acta Cryst.* 2005, **E61**, 1718-1720*.
- 8 Coghlan, S.W.; Richard, G.L.; Howard, J.A.K.; Patrick, L.G.F.; Probert, M.R.; Smith, G.E.; Whiting, A. *J. Organomet. Chem.*, *In Press*.


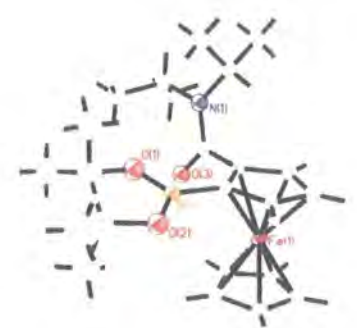
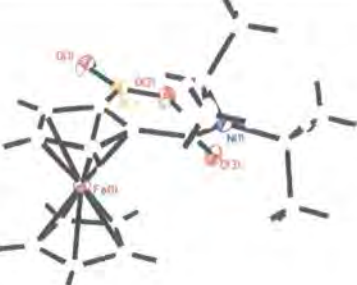
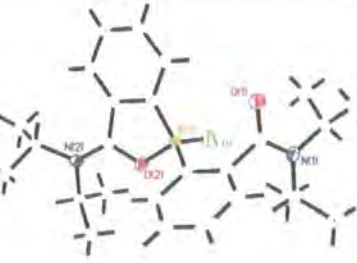
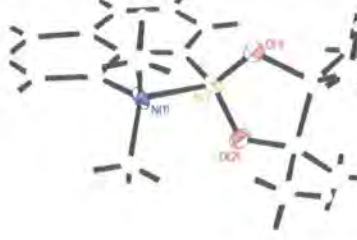
* Work completed in 2001 as part of M. Chem. Chemistry, University of Oxford (1997-2001).

Appendix C: Other Structure Analyses.


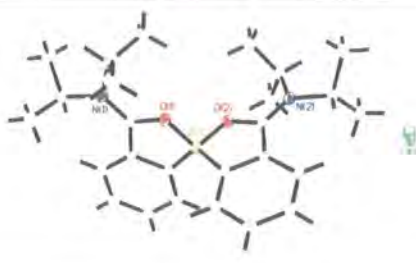
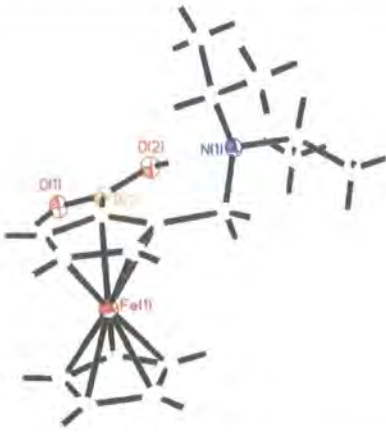

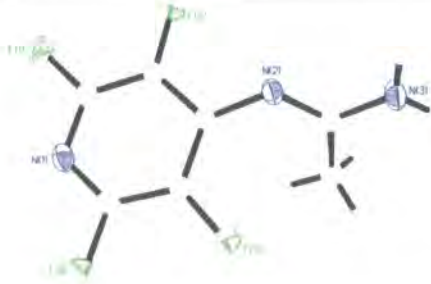
To aid in learning the basic skills for structure refinement a number of ‘service’ crystals were analysed. These are crystals that are synthesised in the University of Durham, Chemistry Department that are submitted for analysis, frequently in order to confirm chemical connectivity. Below is a table of such structures that were solved and refined during the period of this work.

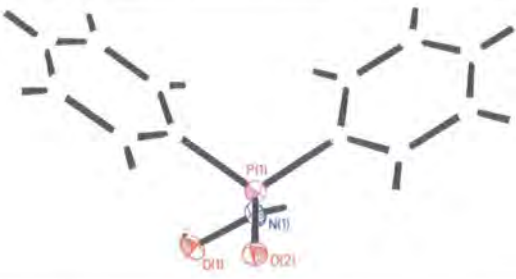
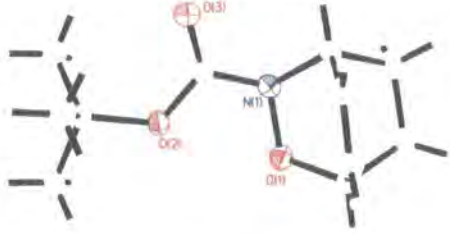
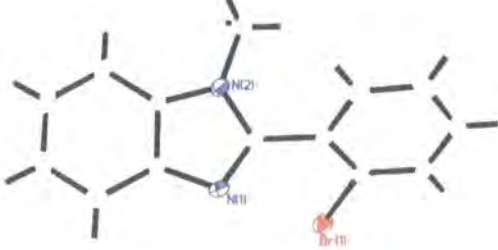
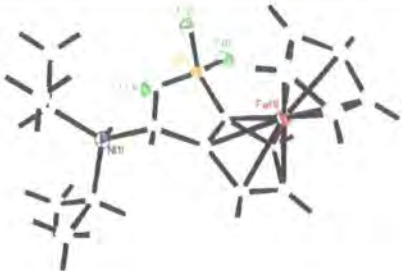
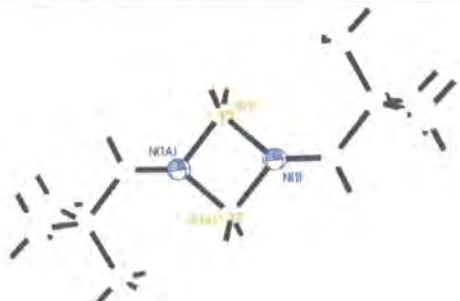
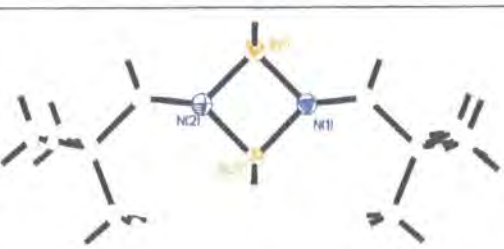
Service #	50% ellipsoid plot of main chemical constituent	Notes
02srv013		$R_1=0.0440$ $wR_2=0.1049$ Max and Min Residual electron densities 0.22 and $-0.19 \text{ e.}\text{\AA}^{-3}$
02srv028		$R_1=0.0435$ $wR_2=0.1173$ Max and Min Residual electron densities 0.32 and $-0.17 \text{ e.}\text{\AA}^{-3}$
02srv032		$R_1=0.0417$ $wR_2=0.0864$ Max and Min Residual electron densities 0.40 and $-0.44 \text{ e.}\text{\AA}^{-3}$
02srv074		$R_1=0.0338$ $wR_2=0.0931$ Max and Min Residual electron densities 0.43 and $-0.24 \text{ e.}\text{\AA}^{-3}$

02srv085		$R_1=0.0744$ $wR_2=0.2014$ Max and Min Residual electron densities 1.21 and $-0.44 \text{ e.}\text{\AA}^{-3}$
02srv104		$R_1=0.0355$ $wR_2=0.0687$ Max and Min Residual electron densities 0.17 and $-0.17 \text{ e.}\text{\AA}^{-3}$
02srv117		$R_1=0.0279$ $wR_2=0.0678$ Max and Min Residual electron densities 0.24 and $-0.15 \text{ e.}\text{\AA}^{-3}$
02srv145		$R_1=0.0611$ $wR_2=0.1124$ Max and Min Residual electron densities 0.31 and $-0.33 \text{ e.}\text{\AA}^{-3}$
02srv148		$R_1=0.0700$ $wR_2=0.1323$ Max and Min Residual electron densities 0.38 and $-0.31 \text{ e.}\text{\AA}^{-3}$

02srv156		$R_1=0.0475$ $wR_2=0.1346$ Max and Min Residual electron densities 0.26 and $-0.20 \text{ e.}\text{\AA}^{-3}$
02srv160		$R_1=0.0995$ $wR_2=0.2492$ Max and Min Residual electron densities 0.69 and $-1.48 \text{ e.}\text{\AA}^{-3}$ Twinned data presented at BCA Autumn meeting
02srv162		$R_1=0.0209$ $wR_2=0.0530$, Max and Min Residual electron densities 0.30 and $-0.19 \text{ e.}\text{\AA}^{-3}$
02srv168		$R_1=0.0689$ $wR_2=0.1345$ Max and Min Residual electron densities 0.21 and $-0.22 \text{ e.}\text{\AA}^{-3}$
02srv181		$R_1=0.0697$ $wR_2=0.1020$ Max and Min Residual electron densities 0.13 and $-0.14 \text{ e.}\text{\AA}^{-3}$

02srv182		$R_1=0.0409$ $wR_2=0.1187$ Max and Min Residual electron densities 0.34 and $-0.17 \text{ e.}\text{\AA}^{-3}$
02srv183		$R_1=0.0402$ $wR_2=0.0915$ Max and Min Residual electron densities 0.38 and $-0.42 \text{ e.}\text{\AA}^{-3}$
02srv184		$R_1=0.0490$ $wR_2=0.1329$ Max and Min Residual electron densities 0.48 and $-0.28 \text{ e.}\text{\AA}^{-3}$
02srv189		$R_1=0.0391$ $wR_2=0.1157$ Max and Min Residual electron densities 0.48 and $-0.20 \text{ e.}\text{\AA}^{-3}$
02srv201		$R_1=0.0353$ $wR_2=0.0636$ Max and Min Residual electron densities 0.31 and $-0.29 \text{ e.}\text{\AA}^{-3}$

02srv236		$R_1=0.0540$ $wR_2=0.1572$ Max and Min Residual electron densities 0.67 and $-0.56 \text{ e.}\text{\AA}^{-3}$
02srv250		$R_1=0.0371$ $wR_2=0.0915$ Max and Min Residual electron densities 0.27 and $-0.21 \text{ e.}\text{\AA}^{-3}$
02srv261		$R_1=0.0384$ $wR_2=0.0776$ Max and Min Residual electron densities 1.02 and $-0.36 \text{ e.}\text{\AA}^{-3}$
02srv262		$R_1=0.0496$ $wR_2=0.1341$ Max and Min Residual electron densities 0.73 and $-0.66 \text{ e.}\text{\AA}^{-3}$
02srv265		$R_1=0.0405$ $wR_2=0.1162$ Max and Min Residual electron densities 0.39 and $-0.24 \text{ e.}\text{\AA}^{-3}$

02srv276		$R_1=0.0445$ $wR_2=0.1123$ Max and Min Residual electron densities 0.40 and $-0.51 \text{ e.}\text{\AA}^{-3}$
03srv015		$R_1=0.0546$ $wR_2=0.1587$ Max and Min Residual electron densities 0.23 and $-0.16 \text{ e.}\text{\AA}^{-3}$
03srv051		$R_1=0.0422$ $wR_2=0.0915$ Max and Min Residual electron densities 1.29 and $-0.84 \text{ e.}\text{\AA}^{-3}$
03srv056		$R_1=0.0314$ $wR_2=0.0768$ Max and Min Residual electron densities 0.83 and $-0.25 \text{ e.}\text{\AA}^{-3}$
03srv057		$R_1=0.0692$ $wR_2=0.1840$ Max and Min Residual electron densities 0.33 and $-0.19 \text{ e.}\text{\AA}^{-3}$
03srv065		$R_1=0.0562$ $wR_2=0.1044$ Max and Min Residual electron densities 0.23 and $-0.19 \text{ e.}\text{\AA}^{-3}$

Appendix D: Research Sample Crystallographic Tables

These are found on the CD on the inside of the back cover of this thesis.